UNIVERSITY OF CALIFORNIA, SAN DIEGO

# Chemical Substitution Effects on Correlated $f$-electron Systems

A dissertation submitted in partial satisfaction of the
requirements for the degree Doctor of Philosophy

in

Materials Science and Engineering

by

Inho Jeon

Committee in charge:

Professor M. Brian Maple, Chair
Professor Richard D. Averitt
Professor Eric E. Fullerton
Professor Y. Shirley Meng
Professor Sunil K. Sinha

2017

The dissertation of Inho Jeon is approved, and it is acceptable in quality and form for publication on microfilm and electronically:

---

---

---

---

---

Chair

University of California, San Diego

2017

# DEDICATION

이 논문을 아버지, 어머니, 그리고 동생에게 바칩니다.

# EPIGRAPH

*The important thing is not to stop questioning. Curiosity has its own reason for existing. One cannot help but be in awe when he contemplates the mysteries of eternity, of life, of the marvelous structure of reality. It is enough if one tries merely to comprehend a little of this mystery every day. Never lose a holy curiosity.*

– Albert Einstein

*I am among those who think that science has great beauty. A scientist in his laboratory is not only a technician: he is also a child placed before natural phenomena which impress him like a fairy tale.*

– Marie Curie

*We have a lot of fish to fry.*

– M. Brian Maple

*지금 자면 꿈을 꿀 수 있지만, 지금 공부하면 꿈을 이룰 수 있다.*

– 장영실

TABLE OF CONTENTS

LIST OF FIGURES

LIST OF TABLES

ACKNOWLEDGEMENTS

This dissertation was completed, thanks to the assistance of many people. First and foremost I would like to thank my advisor, Professor M. Brian Maple for providing me the opportunity to explore the fascinating world of materials science and experimental physics, as well as his support and encouragement throughout the years. None of work in this dissertation would be possible without his clear direction and generous support.

I would like to thank the entire members of Maple group who have been both scientific colleagues and good friends during my time as a Ph.D. student in UCSD. Deep gratitude to Duygu Yazici for introducing me to the various types of synthesis techniques, Ben White for high scientific standards and great writing skills, Sheng Ran for inspiring me by his creative thinking and sharing burdens of the tetra-arc crystal growths, and Noravee Kanchanavatee for introducing me to the XRD analysis. Thanks to Kevin Huang for introducing me to the skutterudite projects, Sooyoung Jang for being a good friend sharing life discussions, Veronica Burnett and Aaron Friedman for showing me to find joy during the Lab life, Naveen Pouse and Alexander Breindel for spending hard times together to deal with various malfunctions in the Lab, Christian Wolowiec and Yuankan Fang for being nice office-mates and having great discussion on $BiS_2$ projects, Colin McElroy and Ivy Lum for their sense of humor, and Christine Coffey (and Camus) for managing various complicated administrative tasks.

Most importantly, this work is dedicated to my family. All I have and will accomplish are only possible due to their love and sacrifices. My father, Jong-Taek, has always been a great supporter of mine. My mother, Yeonmi, has always encouraged me to remind me to do what I love. I thank my brother, Yuho, for being a good friend and for overcoming all the hard times during my absence.

Finally I would like to thank my friends here and in Korea for sharing happiness and sadness together during my Ph.D. life in San Diego. I look forward to having laughs with each of you.

The text and data presented in Chapter III are reprints of material that appears in "Effect of yttrium substitution on the superconducting properties of $La_{1-x}Y_xO_{0.5}F_{0.5}BiS_2$," I. Jeon, D. Yazici, B. D. White, A. J. Friedman, and M. B. Maple, *Phys. Rev. B* **90**, 054510 (2014). The dissertation author is the primary investigator and author of this article.

The text and data presented in Chapter IV are reprints of material that appears in "Investigation of superconducting and normal-state properties of the filled-skutterudite system $PrPt_4Ge_{12-x}Sb_x$," I. Jeon, K. Huang, D. Yazici, N. Kanchanavatee, B. D. White, P.-C. Ho, N. Pouse, and M. B. Maple, *Phys. Rev. B* **93**, 104507 (2016). The dissertation author is the primary investigator and author of this article.

The text and data presented in Chapter V are reprints of material that appears in "Crossover and coexistence of superconductivity and antiferromagnetism in the filled-skutterudite system $Pr_{1-x}Eu_xPt_4Ge_{12}$," I. Jeon, S. Ran, A. J. Breindel, P.-C. Ho, R. B. Adhikari, C. C. Almasan, B. Luong, and M. B. Maple, *Phys. Rev. B* **95**, 134517 (2017). The dissertation author is the primary investigator and author of this article.

## VITA

| | |
|---|---|
| 2010 | Bachelor of Science in Applied Physics<br>Hanyang University, Korea |
| 2012 | Master of Science in Applied Physics<br>Hanyang University, Korea |
| 2013−2017 | Teaching Assistant, Department of Physics<br>University of California, San Diego |
| 2012−2017 | Graduate Research Assistant, University of California, San Diego<br>Advisor: M. Brian Maple |
| 2017 | Doctor of Philosophy in Materials Science and Engineering<br>University of California, San Diego<br>Advisor: M. Brian Maple |

## PUBLICATIONS


B. J. Taylor, T. H. Emery, A. M. Leese de Escobar, I. Jeon, and M. B. Maple, "Examination of the thermal annealing process in producing $YBa_2Cu_3O_{\nabla x}$ films and characterization of pressure stabilized oxygen chain states," *IEEE Trans. Appl. Supercond.* **27**, 4 (2017)

I. Jeon, S. Ran, A. J. Breindel, P.-C. Ho, R. B. Adhikari, C. C. Almasan, B. Luong, and M. B. Maple, "Crossover and coexistence of superconductivity and antiferromagnetism in the filled-skutterudite system $Pr_{1-x}Eu_xPt_4Ge_{12}$," *Phys. Rev. B* **95**, 134517 (2017)

N. P. Butch, S. Ran, I. Jeon, N. Kanchanavatee, K. Huang, A. J. Breindel, M. B. Maple, R. L. Stillwell, Y. Zhao, L. Harriger, and J. W. Lynn, "Distinct magnetic spectra in the hidden order and antiferromagnetic phases in $URu_{2-x}Fe_xSi_2$," *Phys. Rev. B* **94**, 201102(R) (2016)

S. Ran, C. T. Wolowiec, I. Jeon, N. Pouse, N. Kanchanavatee, B. D. White, K. Huang, D. Martien, T. DaPron, D. Snow, M. Williamsen, S. Spagna, P. S. Riseborough, and M. B. Maple, "Phase diagram and thermal expansion measurements on the system $URu_{2-x}Fe_xSi_2$," *PNAS* **113**, 47, 13348-13353 (2016)

Y. P. Singh, R. B. Adhikari, S. Zhang, K. Huang, D. Yazici, I. Jeon, M. B. Maple, M. Dzero, and C. C. Almasan, "Multiband superconductivity in the correlated electron filled skutterudite system $Pr_{1-x}Ce_xPt_4Ge_{12}$," *Phys. Rev. B* **94**, 144502 (2016)

K. Huang, D. Yazici, B. D. White, I. Jeon, A. J. Breindel, N. Pouse, and M. B. Maple, "Superconducting and normal state properties of the systems $La_{1-x}M_xPt_4Ge_{12}$ ($M$ = Ce, Th)," *Phys. Rev. B* **94**, 094501 (2016)

I. Jeon, K. Huang, D. Yazici, N. Kanchanavatee, B. D. White, P.-C. Ho, S. Jang, N. Pouse, and M. B. Maple, "Investigation of superconducting and normal-state properties of the filled-skutterudite system $PrPt_4Ge_{12-x}Sb_x$," *Phys. Rev. B* **93**, 104507 (2016)

D. Yazici, I. Jeon, B. D. White, and M. B. Maple, "Superconductivity in Layered $BiS_2$-based Compounds," *Physica C*, **514**, 218-236 (2015) (Review Article)

B. J. Taylor, T. H. Emery, S. A. E. Berggren, A. M. Leese de Escobar, I. Jeon, and M. B. Maple, "Preparation of novel HTS films and tunnel junctions for advanced C3I sensor applications," *SPIE* **9467**, 946725 (2015)

I. Jeon, D. Yazici, B. D. White, A. J. Friedman, and M. B. Maple, "Effect of yttrium substitution on the superconducting properties of $La_{1-x}Y_xO_{0.5}F_{0.5}BiS_2$," *Phys. Rev. B* **90**, 054510 (2014)

C. T. Wolowiec, B. D. White, I. Jeon, D. Yazici, K. Huang, and M. B. Maple, "Enhancement of superconductivity near the pressure-induced semiconductor-metal transition in the $BiS_2$-based superconductors $LnO_{0.5}F_{0.5}BiS_2$ ($Ln$ = La, Ce, Pr, Nd) compounds," *J. Phys.:Condens. Matter* **25**, 422201 (2013)

D. Yazici, K. Huang, B. D. White, I. Jeon, V. W. Vurnett, A. J. Friedman, I. K. Lum, M. Nallaiyan, S. Spagna, and M. B. Maple, "Superconductivity induced by electron doping in $La_{1-x}M_xOBiS_2$ ($M$ = Ti, Zr, Hf, Th)," *Phys. Rev. B* **87**, 174512 (2013)

## FIELDS OF STUDY

Major Field: Materials Science and Engineering

Exploratory and investigative synthesis of correlated $f$-electron systems
M. Brian Maple, Bernd T. Matthias Professor of Physics,
University of California, San Diego

ABSTRACT OF THE DISSERTATION

Chemical Substitution Effects on Correlated $f$-electron Systems

by

Inho Jeon
Doctor of Philosophy in Materials Science and Engineering
University of California, San Diego, 2017
Professor M. Brian Maple, Chair

Strongly correlated $f$-electron systems are a rich reservoir for exotic and intriguing physical phenomena; their competition and interplay between localized magnetic moments in partially filled $d-$ or $f$-electron shells, and conduction electron states lead to complex magnetism, unconventional superconductivity, and other intricate matter of states. The complex phase diagrams of temperature $T$ versus a control parameter $\delta$, such as chemical composition $x$, applied pressure $P$, and magnetic field $H$, have been observed, where they exhibit new and unexpected physics, including "non-Fermi-liquid" (NFL) behavior, "rattling" motion of atoms in a cage structure, local structure distortion, crossover of superconducting order parameters, and the coexistence of superconductivity and magnetism. In order to explore such new phase diagrams, therefore, the work in this dissertation focuses on several chemical substitution studies on $f$-electron systems: the layered superconductor $La_{1-x}Y_xO_{0.5}F_{0.5}BiS_2$, and the filled-skutterudite $PrPt_4Ge_{12-x}Sb_x$ and $Pr_{1-x}Eu_xPt_4Ge_{12}$ systems, whose parent compound $PrPt_4Ge_{12}$ is an unconventional superconductor. Polycrystalline samples were synthesized during the course

of the studies and were characterized by means of x-ray diffraction, electrical resistivity, magnetic susceptibility, and specific heat measurements.

# Chapter I

# Introduction

Before the development of quantum mechanics in the early 20th century, scientists generally believed that the behavior of objects in the universe could be predicted by understanding the behavior of their constituent parts. As an example, solving the equations of motion for every atom in a system could make accurate predictions of the system's behavior in the future. However, many systems around us defy this concept. A living cell is composed of carbon, hydrogen, and oxygen with other elements. We could study these elements individually, without imagining or predicting such a right way that combines elements into a complex living creature. In 1972, P. W. Anderson mentioned "The behavior of large and complex aggregates of elementary particles, it turns out, is not to be understood in terms of a simple extrapolation of the properties of a few particles." in his article entitled *"More is Different"* [1]. This complex phenomena is called "Emergent behavior."

In the condensed matter physics area, there are various types of emergent phenomena, where the level of understanding is lacking only by the fundamental forces of nature. Especially, $f$-electron systems have shown to be a reservoir of novel electronic states and exotic superconducting and magnetic phenomena, such as the Kondo physics, valence fluctuations, heavy fermion, non-Fermi liquid behavior, magnetism, conventional and unconventional superconductivity, and the coexistence of superconductivity and magnetism. The emergence of a wide variety

of phenomena is believed to arise from an intricate interplay between competing interactions. This dissertation discusses several studies on $f$-electron systems; they exhibit superconductivity, magnetism, and their interplay, that could be tuned via the variation of control parameters, including chemical composition, pressure, and magnetic field. The following sections will introduce key concepts for previously mentioned studies.

## I.A Correlated Electron Phenomena

### I.A.1 Fermi liquid behavior

The classical models for the free electrons by Drude or Sommerfeld were successful in describing behavior of electrons in a solid, such as the temperature dependence of the electronic contribution to specific heat; however, they could not fully explain the behavior of simple metals, including the alkali metals, alkaline earths, and noble metals (Cu, Ag, Au). It is because interactions between electrons or electrons and phonons affect their physical properties. L. D. Landau introduced the phenomenological theory of Fermi liquids to explain the behavior of interacting fermions [2]. Unlike early classical models for free electrons, in which electrons are treated as non-interacting particles, Landau proposed the concept of the quasiparticle by taking electron-electron interactions into account. The quasiparticles could still be treated as non-interacting particles and follow the free electron model, but with an enhanced effective mass $m^*$ (as large as several hundred times the free electron mass). The Fermi liquid model predicted several physical properties at low temperature in the following way:

$$\begin{aligned} \frac{C(T)}{T} &= \frac{m^*}{m_e}\gamma_0, \quad \text{where } \gamma_0 = \left(\frac{\pi^2 k_B^2}{3}\right) N(E_F) \\ \chi(T) &= \frac{m^*}{m_e}\frac{\chi_0}{1+F_0^a}, \quad \text{where } \chi_0 = \mu_B^2 N(E_F) \\ \rho(T) &= \rho_0 + AT^2 \end{aligned} \tag{I.1}$$

where $F_0^a$ is a Landau parameter, $m_e$ is the free electron mass, and $\sqrt{A} \propto m^*$. For regular metlas, $m^*/m_e \sim 1-10$ and $\gamma_0 \sim 1-10$ mJ/mol-K$^2$. Therefore, $\gamma$ ($\equiv C/T$) and $\chi$ are constant and the resistivity saturates as $T^2$ at low temperatures.

### I.A.2 Quantum criticality and Non-Fermi liquid behavior

In the classical phase transitions, there are two main categories. One is the first-order phase transition, which exhibits discontinuity in the first derivative of the free energy with respect to thermodynamic variables. Another is the second order phase transition, showing continuity in the first derivative but discontinuity in the second derivative of the free energy. The second-order phase transitions also show the growth of fluctuations with large length scales, which are called "critical fluctuations". At the critical point, where a second-order transition occurs, the critical fluctuations extend over the entire system.

The critical fluctuations associated with the quantum phase transition are quantum mechanical in nature, exhibiting scale invariance in both space and in time. The quantum critical point (QCP), where the quantum phase transitions occur, is present only at the absolute zero temperature; however, its influence can be observed in over a wide range of temperatures above the quantum critical point. Thus, the effect of "quantum criticality" is felt without reaching the absolute zero temperature (but still low temperature). The QCP can be experimentally accessed through the tuning parameters ($\delta$), such as applied magnetic field ($H$), applied pressure ($P$), or chemical substitution ($x$). It is believed that the high temperature superconductivity in the cuprate superconductors is the consequence of a QCP; the suppression of the antiferromagnetic or pseudogap phase is responsible for dome-shaped superconductivity, in which the complete suppression of the antiferromagnetic or pseudogap phase is located at the center [4].

Near the QCP, the properties of the metal are rapidly changed by the critical fluctuations at low temperatures, resulting in the qualitative deviation from the Fermi liquid behavior. This manifestation is called a "strange metal" or a non-

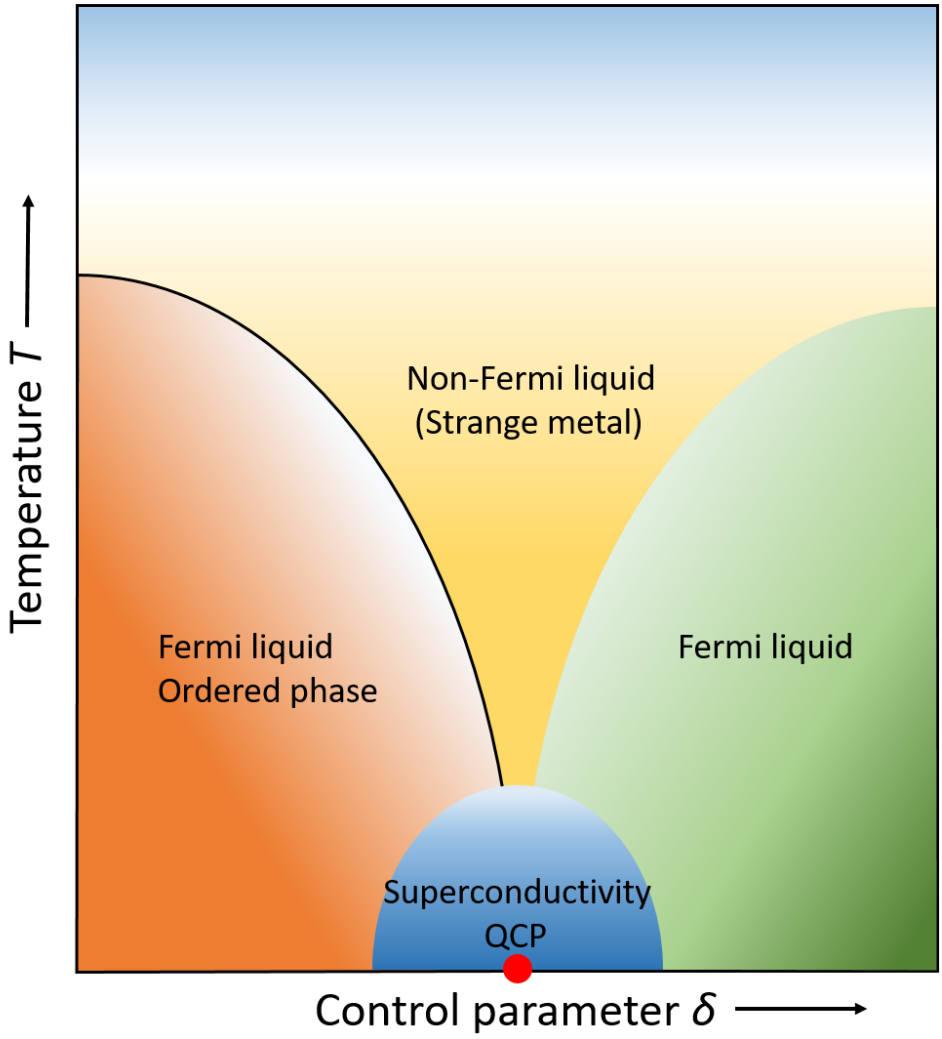


Figure I.1: The NFL behavior occurs in a V-shaped region above the QCP (red dot). The QCP is enveloped by some type of order (usually superconductivity). This scenario can be seen in the $CeIn_3$ system upon applied external pressure [3].

Fermi liquid (NFL) behavior. The physical properties of the NFL behavior are characterized by logarithmic or weak power law divergences at low temperatures $T$, as below:

$$\begin{aligned} &\frac{C(T)}{T} \sim -lnT, \text{ or} \sim T^{-1+\lambda}, \\ &\chi(T) \sim 1 - cT^{1/2}, \sim -lnT, \text{ or} \sim T^{-1+\lambda}, \\ &\rho(T) \sim \rho_0 + A'T^n \end{aligned} \tag{I.2}$$

where usually $\gamma \sim 0.7 - 0.8$ and $1 \leq n < 2$ ($n \sim 0.5$ has also been observed). In general, the NFL behavior is associated with quantum mechanical fluctuations of the order parameter near the QCP, as illustrated in Fig. I.1. However, the NFL behavior is also observed in the absence of the QCP; it may be associated with unconventional Kondo phenomena [5, 6] or other possible physical mechanisms [7].

### I.A.3 Magnetism

Magnetism was first discovered in the ancient Greeks, when people found that naturally magnetized pieces of the mineral "magnetite" attract iron. The word "magnet" comes after the Greek term for lodestone, "magnítis líthos", meaning a stone from the region of Magnesia. The nature of magnetism was not truly understood until the developments of quantum mechanics.

#### Magnetic moments in $f$-electron ions

Besides the itinerant electron magnetism in metals, magnetism could also arise from localized unpaired electron spins in various systems including transition metal, rare earth, and actinide elements. The magnetic moment of a free atom has three fundamentals: the electron spin, its orbital angular momentum, and the change in the orbital moment induced by an applied magnetic field. The first two are associated with *"paramagnetic"* contributions to the magnetization, while the third one gives a *"diamagnetic"* contribution. Atoms with fully filled electron

shells have zero unpaired electron spins and zero orbital moment, indicating the finite moment values are associated with partially filled shells.

The magnetic susceptibility, $\chi$, is the change in the magnetization, $M$, upon applied magnetic field $H$.

$$\chi = \frac{M}{H} \tag{I.3}$$

A material with a negative magnetic susceptibility value is called diamagnetic, while one with a positive susceptibility is paramagnetic.

**Atomic susceptibility** If the interactions between localized electron spins are not considered (i.e., the isolated magnetic moments), the interaction energy of the magnetic field with each electron spin along the $z$-axis is given by

$$\Delta\mathcal{H} = g_0\mu_B H \cdot S_z \tag{I.4}$$

where the sum of each electron spin is $S_z = \sum_i s_z^i$, $\mu_B$ is the Bohr magneton ($\mu_B = (e\hbar)(2mc)$), and $g_0$ is the electronic $g-$factor ($g_0 \sim 2$). The total Hamiltonian with the momentum of each electron is

$$\mathcal{H} = \frac{1}{2m}\sum_i \left[p_i + \frac{e}{c}\mathbf{A}(r_i)\right]^2 = \frac{1}{2m}\sum_i \left(p_i - \frac{e}{2c} r_i \times \mathbf{H}\right)^2 \tag{I.5}$$

where $\mathbf{A}$ is the uniform vector potential. This could be expanded below

$$\mathcal{H} = \mathcal{H}_0 + \mu_B \mathbf{L}\cdot\mathbf{H} + \frac{e^2}{8mc^2}H^2\sum_i (x_i^2 + y_i^2) \tag{I.6}$$

where $\mathbf{L}$ is the total electronic orbital angular momentum

$$\hbar\mathbf{L} = \sum_i r_i \times p_i \tag{I.7}$$

Combining Eqs. I.4 and I.5, the field-dependent Hamiltonian upon the magnetic field $\mathbf{H} = \nabla \times \mathbf{A}$ is:

$$\mathcal{H} = \mathcal{H}_0 + \mu_B(\mathbf{L} + g_0\mathbf{S}) \cdot \mathbf{H} + \frac{e^2}{8mc^2} H^2 \sum_i (x_i^2 + y_i^2) \tag{I.8}$$

The second term $\mu_B(\mathbf{L} + g_0\mathbf{S}) \cdot \mathbf{H}$ is the *paramagnetic* part and the following part $\frac{e^2}{8mc^2} H^2 \sum_i (x_i^2 + y_i^2)$ is the *diamagnetic* term. Using second-order perturbation theory, an estimate of the paramagnetic term reveals that it is almost always dominant, even in a strong magnetic field ($\sim 1$ tesla).

**Larmor diamagnetism** In terms of quantum mechanics, all materials should have some diamagnetic contributions to the magnetic suscpetibility due to the second term in Eq. I.8. Consider a material with fully occupied electronic shells, where $\mathbf{J}|0\rangle = \mathbf{L}|0\rangle = \mathbf{S}|0\rangle = 0$. In order to have zero spin and zero orbital angular momentum, the first-order shift in the ground state is given by

$$\Delta E_0 = \frac{e^2}{8mc^2} H^2 \langle 0| \sum_i (x_i^2 + y_i^2)|0\rangle = \frac{e^2}{12mc^2} H^2 \langle 0| \sum_i (r^2)|0\rangle \tag{I.9}$$

where $\langle x_i^2 \rangle = \langle y_i^2 \rangle = \frac{1}{3}\langle r_i^2 \rangle$. The susceptibility of a material with $N$ ions is

$$\chi = -\frac{N}{V} \frac{\partial^2 \Delta E_0}{\partial H^2} = -\frac{e^2}{6mc^2} \frac{N}{V} \langle 0| \sum_i (r^2)|0\rangle \tag{I.10}$$

This is known as the *Larmor diamagnetic susceptibility*. The diamagnetism simply means a negative susceptibility (i.e., cases in which the direction of induced moment is opposite to that of applied field, such as a superconductor below its superconducting critical temperature $T_c$). Magnetic properties of noble gases and simple ionic crystals such as alkali halides can be explained by Eq. I.10; their molar susceptibility values are typically of order $\sim 10^{-5}$ cm$^3$/mole, indicating their magnetization, $M$, is small compared with the applied magnetic field $H$.

**Hund's rules** When a solid contains ions with partially filled electronic shells, the total angular momentum of an electron can have a lot of possible configurations. Instead of calculating all possible states, in 1927, F. Hund formulated a series of rules, called Hund's rules, which are used to determine the ground state for given orbital angular momentum $l$. There are three rules:

1. The first rule states the lowest energy atomic state maximizes the total spin angular momentum $S$. If a solid contains $n \leq 2l+1$ electrons, the largest total spin value, $S = l + \frac{1}{2}$, minimizes the Coulomb energy, due to the Pauli exclusion principle. Since the exclusion principle requires opposite spins to fill electron shells after the $(2l+1)$th electron, the $S$ value is reduced from its maximum value by half a unit for each electron after $(2l+1)$.

2. The second rule maximizes the total orbital angular momentum $L$ of the electrons, which is consistent with the first rule and with the exclusion principle. To determine the value, electrons will go into a level with highest value of $|l_z|$. The rest of the electrons with the same spins will have different $l_z$ values due to the exclusion principle, following the manner $L = l + (l-1) + \cdots + [l-(n-1)]$. This minimizes the overlap of the wavefunctions, and again lowers the effective energy. When the shell is precisely half filled, the value of total orbital momentum $L$ is zero. The second half of the shell will be filled with electrons with opposite spins, resulting in the same series of values for $L$.

3. The above two rules still leave $(2L+1)(2S+1)$ possible states. These can be further classified, attempting to minimize spit-orbit coupling energy. The value of $J$ can be determined as,

$$\begin{aligned} J &= |L-S|, \qquad && n \leq (2l+1), \\ J &= L+S, && n \geq (2l+1) \end{aligned} \tag{I.11}$$

For transition metal ions, this procedure is not applicable, since the $3d$ outermost shell is responsible for paramagnetism in transition metal ions, resulting in crystal field effect, which is an intense inhomogeneous electric field produced by

neighboring ions. However, for rare earth $f$-electron ions, this term is applicable, since their $4f$ shells are responsible for paramagnetism and lie inside the ions within the $5s$ and $5p$ electron shells.

Consider two examples of Hund's rules. For the case of the $Pr^{3+}$ ion, there are two electrons in the $4f$ electron shell. Thus, this results in $S = \frac{1}{2} + \frac{1}{2} = 1$, $L = 3 + 2 = 5$. Since the shell is less than half filled, $J = |5 - 1| = 4$. The $Gd^{3+}$ ion has 7 electrons in the $4f$ electron shell and the shell is more than half filled, resulting in $S = \frac{7}{2}$, $L = 0$, and $J = L + S = \frac{7}{2}$.

**Paramagnetism** The ions with partially filled electron shells, the dominant contribution to the susceptibility is from the paramagnetic term, $\mu_B(\mathbf{L} + g_0\mathbf{S}) \cdot \mathbf{H}$, in Eq. I.8. If the $4f$ shell is one electron short of being half filled ($J = 0$), it seems that the paramagnetic term has zero contribution to the susceptibility. However, the paramagnetic term does not vanish, according to second-order perturbation theory. It predicts a change in the ground state energy $E_0$ since the excited state is mixed ($J \neq 0$) as follows,

$$\Delta E_0 = -\sum_n \frac{|\langle 0|\mu_B \mathbf{H} \cdot (\mathbf{L} + g_0\mathbf{S})|n\rangle|^2}{E_n - E_0} + \frac{e^2}{8mc^2} H^2 \langle 0| \sum_i (x_i^2 + y_i^2)|0\rangle \qquad \text{(I.12)}$$

If a solid contains some ions per unit volume $N/V$, the susceptibility, $\chi = -\frac{N}{V}\frac{\partial^2 E_0}{\partial H^2}$, is given below

$$\chi = \frac{N}{V}\left[2\mu_B^2 \sum_n \frac{|\langle 0|\mathbf{L}_z + g_0\mathbf{S}_z|n\rangle|^2}{E_n - E_0} - \frac{e^2}{4mc^2}\langle 0| \sum_i (x_i^2 + y_i^2)|0\rangle\right] \qquad \text{(I.13)}$$

The second term is the Larmor diamagnetic susceptibility as discussed previously. The first term has a sign opposite to that of the second term. Therefore, it favors alignment of the moment parallel to the applied magnetic field, which is known as paramagnetism. However, the paramagnetic contribution to the susceptibility is small and temperature independent. This paramagnetic correction to the Larmor diamagnetic susceptibility is known as *Van Vleck paramagnetism*.

If the shell is partially filled and does not have $J = 0$, the diamagnetic term can safely be ignored, as discussed earlier. If the ground state is $(2J + 1)$-fold degenerate in zero magnetic field, the following relation without the surrounding state vectors can be obtained [8, 9],

$$\mathbf{L} + g_0\mathbf{S} = g_J\mathbf{J} \tag{I.14}$$

where $g_0$ is the electron $g$-factor ($\sim 2$) and $g_J$ is the Landé $g$-factor,

$$\begin{aligned} g_J &= \frac{1}{2}(g_0 + 1) - \frac{1}{2}(g_0 - 1)\frac{L(L+1) - S(S+1)}{J(J+1)} \\ &= \frac{3}{2} + \frac{1}{2}\left[\frac{S(S+1) - L(L+1)}{J(J+1)}\right] \end{aligned} \tag{I.15}$$

According to the Eq. I.14, the interaction between the magnetic moment and the field is proportional to the total angular momentum of the ion $\mathbf{J} = \mathbf{S} + \mathbf{L}$,

$$\boldsymbol{\mu} = -g_J\mu_B\mathbf{J} \tag{I.16}$$

Since the zero-field ground state is degenerate, it is not possible to calculate the susceptibility by equating the free energy to the ground-state energy as for the non-degenerate shells with $J = 0$. In order to obtain the susceptibility, a statistical mechanical method is the best way to calculate the paramagnetic term. The partition function is,

$$Z = e^{-\beta F} = \sum_{J_z=-J}^{J} exp(-\beta\gamma H J_z), \quad \text{where } \gamma \equiv g_J\mu_B, \quad \beta \equiv \frac{1}{k_B T} \tag{I.17}$$

where the sum is over the $2J + 1$ states, $F$ is the magnetic Helmholtz free energy, and $k_B$ is the Bolztmann constant. The sum of geometric series can be obtained as:

$$Z = \frac{\sinh(\beta\gamma H(J + 1/2))}{\sinh(\beta\gamma H/2)} \tag{I.18}$$

The magnetization, $M$, of $N$ ions in a volume $V$ can be written in the thermodynamic form,

$$M = -\frac{N}{V}\frac{\partial F}{\partial H} = \frac{N}{V}\gamma J B_J(\beta\gamma JH), \tag{I.19}$$

where $B_J(x)$ is the *Brillouin function* defined by

$$B_J(x) = \frac{2J+1}{2J}\coth\frac{2J+1}{2J}x - \frac{1}{2J}\coth\frac{1}{2J}x \tag{I.20}$$

If the field $H$ is fixed and $T \to 0$, the magnetization $M \to (N/V)\gamma J$, indicating that all ions are completely aligned by the field and $|J_z|$ reaches its maximum or saturation value $J$. However, it is unlikely since this case only happens when $k_BT \ll \gamma H$. When $\gamma H \ll k_BT$, using the small-$x$ expansion gives the Brillouin function as

$$B_J(x) = \frac{J+1}{3J}x + O(x^3) \tag{I.21}$$

Therefore, the susceptibility is

$$\chi = \frac{M}{H} = \frac{N}{V}\frac{(g_J\mu_B)^2}{3}\frac{J(J+1)}{k_BT}, \qquad (k_BT \gg g_J\mu_B H) \tag{I.22}$$

**The Curie law and rare earth ions** The variation of the susceptibility is inversely temperature-dependent, known as the *Curie law*. This law characterizes paramagnetic systems with "permanent moments," which favor parallel alignment to the applied field. Even though the Curie law is strictly valid for ($k_BT \gg g_J\mu_B H$), it described the magnetic susceptibility for various systems within large ranges of field and temperature. The paramagnetic contribution to the susceptibility in Eq. I.22 is much larger than the temperature-independent Larmor diamagnetic contribution, when an ion has a partially filled $4f$ electron shell with nonzero $J$. From a rough estimate, the diamagnetic susceptibility is of the order $10^{-5}$, while room temperature paramagnetic susceptibilities are of the order $10^{-2}$ to $10^{-3}$.

Table I.1: Calculated by Eq. I.24 and measured by Eq. I.23 effective magnetic moment (magneton number) values, $\mu_{eff}$, for rare earth ions.

| Element | Electron configuration | Basic level | Calc. $\mu_{eff}$ | Exp. $\mu_{eff}$ |
|---|---|---|---|---|
| $La^{3+}$ | $4f^0$ | $^1S$ | 0.00 | diamagnetic |
| $Ce^{3+}$ | $4f^1$ | $^2F_{5/2}$ | 2.54 | 2.4 |
| $Pr^{3+}$ | $4f^2$ | $^3H_4$ | 3.58 | 3.5 |
| $Nd^{3+}$ | $4f^3$ | $^4I_{9/2}$ | 3.62 | 3.5 |
| $Pm^{3+}$ | $4f^4$ | $^5I_4$ | 2.68 | – |
| $Sm^{3+}$ | $4f^5$ | $^6H_{5/2}$ | 0.84 | 1.5 |
| $Eu^{3+}$ | $4f^6$ | $^7F_0$ | 0.00 | 3.4 |
| $Gd^{3+}$ | $4f^7$ | $^8S_{7/2}$ | 7.94 | 8.0 |
| $Tb^{3+}$ | $4f^8$ | $^7F_6$ | 9.72 | 9.5 |
| $Dy^{3+}$ | $4f^9$ | $^6H_{15/2}$ | 10.63 | 10.6 |
| $Ho^{3+}$ | $4f^{10}$ | $^5I_8$ | 10.60 | 10.4 |
| $Er^{3+}$ | $4f^{11}$ | $^4I_{15/2}$ | 9.59 | 9.5 |
| $Tm^{3+}$ | $4f^{12}$ | $^3H_6$ | 7.57 | 7.3 |
| $Yb^{3+}$ | $4f^{13}$ | $^2F_{7/2}$ | 4.54 | 4.5 |
| $Lu^{3+}$ | $4f^{14}$ | $^1S$ | 0.00 | diamagnetic |

The Curie law is frequently written as:

$$\chi = \frac{1}{3}\frac{N}{V}\frac{\mu_B^2 \mu_{eff}^2}{k_B T} = \frac{C}{T} \tag{I.23}$$

where $C$ is known as the Curie constant and $\mu_{eff}$ is the "effective Bohr magneton number", define as

$$\mu_{eff} \equiv g_J \sqrt{J(J+1)} \tag{I.24}$$

Crystals containing rare earth ions with partially filled $4f$ electron shells have magnetic susceptibilities that are described by a Curie law quite well. The chemical properties of the trivalent rare earth ions are similar since the outermost electron shells have an identical $5s^2 5p^6$ configuration. In lanthanum, at the beginning of rare earth series, the $4f$ shell is empty. The number of $4f$ electrons increases gradually through the rare earth series until the filled shell $4f^{14}$ at lutetium. The radii of the trivalent rare earth ions contract monotonically with increasing number of

electrons in the series, which called the "lanthanide contraction." The $4f$ electrons are confined in the inner shell with a radius of about 0.3 Å, making the magnetic behavior of the rare earth series very interesting; no other group of elements in the periodic table is as intriguing. The calculated and measured magneton numbers are in a good agreement, as shown in Table. I.1. The only exceptions are the case for samarium and europium. In both cases, the ground and excited states of the $L - S$ multiplet are very close in energy, compared to $k_B T$ at room temperature.

For the transition metal ions, $L$ is zero and thus $J = S$, although the Curie law is still obeyed. This is due to the quenching of the orbital angular momentum, by the crystal field.

**Magnetic ordering**

If there were no magnetic interactions, individual magnetic moments would be thermally disordered at any temperature in the absence of a field, and the the sum of moments would be zero. However, in some solid systems, magnetic ions have non-vanishing average vector moments below a critical temperature, $T_c$. Such behavior is called magnetic ordering. For example, some solids show "spontaneous magnetization," even without the applied magnetic field. This is known as *ferromagnetism*. Other systems favor antiparallel orientations of neighboring moments, even though there is no net total moment in the absence of a field, known as *antiferromagnetism*. If a solid favors antiparallel alignment, but its neighboring magnetic ions have magnetic moments of a different magnitude, their moments would not cancel, resulting a net moment; solids that exhibit this behavior are called *ferrimagnets*. Schematics of some types of magnetic ordering are illustrated in Fig. I.2. These examples and other more exotic types of magnetic behavior cannot be explained by the isolated magnetic moments, in which they do not interact with one another; magnetic interactions need to be taken into account in order to understand the striking and complex types of magnetic behavior.

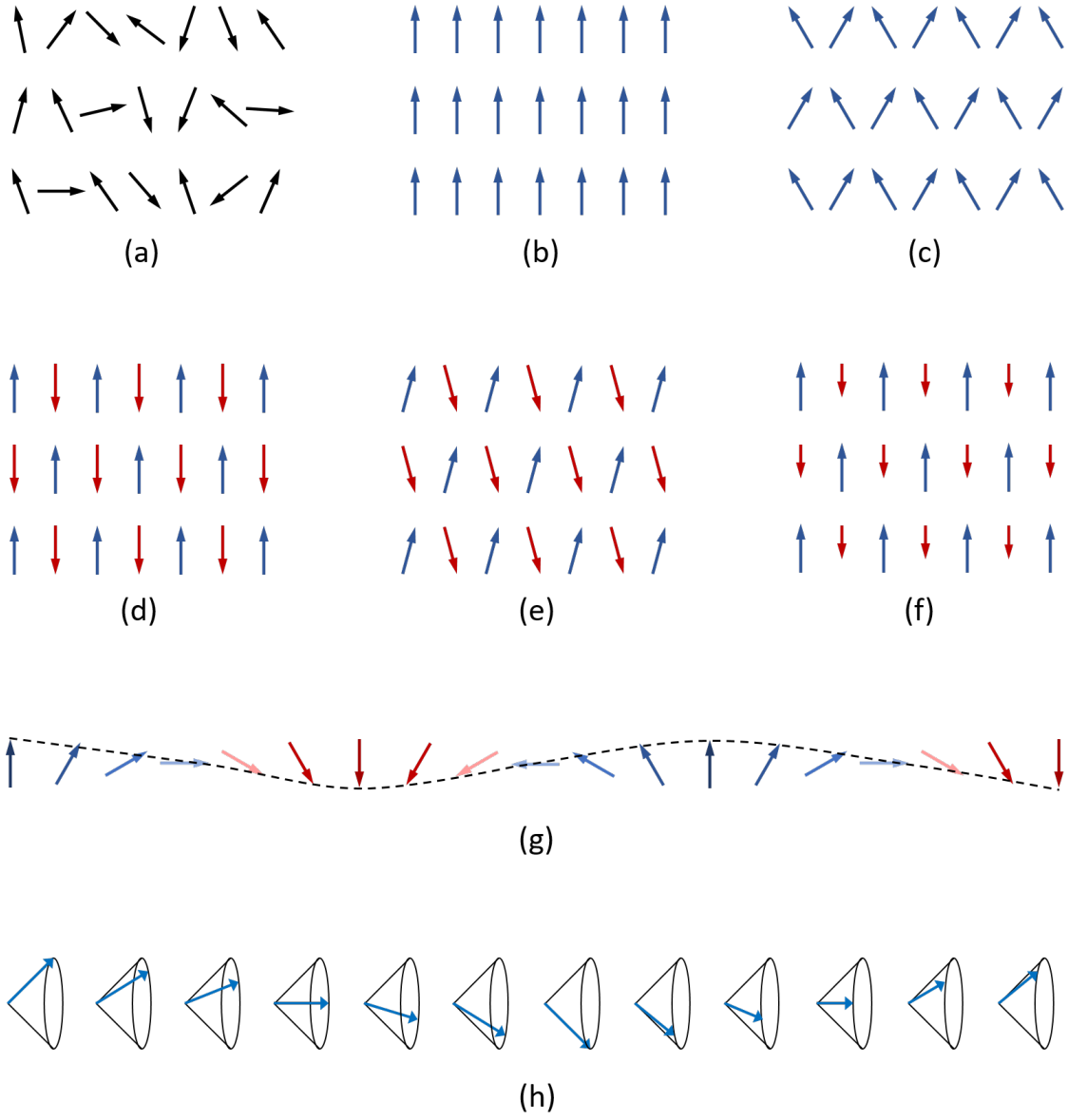


Figure I.2: Schematics for linear arrays of spins are illustrated: (a) Paramagnetic state in the absence of a field. (b, c) Ferromagnetic orderings. (d) Simple antiferromagnetic ordering. (e) Canted antiferromagnet. (f) Ferrimagnetic ordering. (g) A spin wave on a line of spins. (h) Helical spin array.

**Spin Hamiltonian** When many ions of spin $S$ are widely separated in a solid, it is convenient to have an operator, known as the spin Hamiltonian, whose eigenfunctions give the spin of the corresponding states [8].

$$\mathcal{H}^{spin} = -\sum_{i,j} J_{ij}\mathbf{S}_i \cdot \mathbf{S}_j, \tag{I.25}$$

The above Eq. I.25 is known as the *Heisenberg model* for interacting spins, and the $J_{ij}$ is the exchange coupling constant. In general, it is very difficult to extract much information from the Heisenberg model; it introduces the starting point for many profound investigations of magnetism in solids. Therefore, before considering this model, the following criteria must apply: 1) all magnetic ions should be sufficiently far enough apart, so that the electronic wave function overlap is negligible. 2) the coupling of the spin Hamiltonian should strongly depend on spin orientations and not the orbital component of the angular momentum.

The low-lying excitations of magnetic ions at Bravais lattice sites $\mathbf{R}$ can be described by a Heisenberg Hamiltonian from Eq. I.25,

$$\begin{gathered}\mathcal{H} = -\frac{1}{2}\sum_{\mathbf{R}\mathbf{R}'} \mathbf{S}(\mathbf{R}) \cdot \mathbf{S}(\mathbf{R}')J(\mathbf{R}-\mathbf{R}') - g_J\mu_B H \sum_{\mathbf{R}} \mathbf{S}_z(\mathbf{R}), \\ J(\mathbf{R}-\mathbf{R}') = J(\mathbf{R}'-\mathbf{R}) \geq 0\end{gathered} \tag{I.26}$$

This is a ferromagnetic Hamiltonian since a positive exchange interaction $J$ favors parallel spin alignment. If spins in the Hamiltonian are regarded as classical vectors, the ground state will be the one with all spins aligned along the $z$-axis, parallel to the magnetic field. This suggests the quantum-mechanical ground state $|0\rangle$ and its eigenstate by $\mathcal{H}|0\rangle = E_0|0\rangle$, resulting in

$$E_0 = -\frac{1}{2}S^2 \sum_{\mathbf{R},\mathbf{R}'} J(\mathbf{R}-\mathbf{R}') - Ng_J\mu_B HS \tag{I.27}$$

where $E_0$ is the ground state energy for ferromagnetic systems.

Unlike the case of ferromagnet, the Heisenberg antiferromagnet is a difficult and unsolved problem. One special case of a Heisenberg Hamiltonian, which a one-dimensional array of spin 1/2 ions has coupling only between nearest neighbors in the absence of an applied magnetic field,

$$\mathcal{H} = \frac{1}{2} \sum_{\mathbf{R},\mathbf{R}'} |J(\mathbf{R} - \mathbf{R}')\mathbf{S}(\mathbf{R}) \cdot \mathbf{S}(\mathbf{R}') \tag{I.28}$$

assuming the ground state $|0\rangle$ is to put each antiferromagnetic sublattice into a ferromagnetic ground state with oppositely directed sublattice magnetization. This results in a ground-state energy,

$$E_0 = -\frac{1}{2} \sum_{\mathbf{R},\mathbf{R}'} |J(\mathbf{R} - \mathbf{R}')|S^2 \tag{I.29}$$

In contrast to the ferromagnetic case, this is not an eigenstate, since a spin in the "up" sublattice has its $z$-component reduced and a spin in the "down" sublattice is correspondingly raised. The actual ground-state energy has upper and lower bounds, leading to the inequality,

$$-\frac{1}{2}S(S+1) \sum_{\mathbf{R},\mathbf{R}'} |J(\mathbf{R} - \mathbf{R}')| \leq E_0 \leq -\frac{1}{2}S^2 \sum_{\mathbf{R},\mathbf{R}'} |J(\mathbf{R} - \mathbf{R}')| \tag{I.30}$$

In the one-dimensional nearest-neighbor spin 1/2 chain [10], for example, the resultant bound is estimated to be $-0.75NJ \leq E_0 \leq -0.25NJ$; this indicates the exchange coupling is negative for the antiferromanetic case.

**Mean field theory** A quantitative analysis of the ferromagnetic transition was derived by P. Weiss; this is a mean field theory, one simplest rough way of characterizing the type of magnetic orderings. Assuming that each magnetic ion experiences

a field proportional to the magnetization as follow,

$$H_{eff} = H + \lambda M \tag{I.31}$$

where $\lambda = \frac{V}{N}\frac{J_0}{(g_J \mu_B)}$ and $J_0 = \sum_{\mathbf{R}} J(\mathbf{R})$. This mean field theory for ferromagnet suggests that each spin feels the average magnetization of all the other spins by $H_{eff}$. By the mean field approximation, the magnetization density is given as

$$M = M_0\left(\frac{H_{eff}}{T}\right) \tag{I.32}$$

where $M_0$ is the magnetization density in the field $H$ at temperature $T$, extracted in the absence of interactions between magnetic ions (paramagnetic case). The zero-field susceptibility is:

$$\chi_0 = \left(\frac{\partial M_0}{\partial H}\right)_{H=0} = \frac{C}{T} \tag{I.33}$$

where $C$ is the Curie constant by Eq. I.23. Therefore, the susceptibility in the mean field approximation is given as:

$$\chi = \frac{\partial M}{\partial H} = \frac{\partial M_0}{\partial H_{eff}}\frac{\partial H_{eff}}{\partial H} = \chi_0(1 + \lambda\chi) \tag{I.34}$$

Thus,

$$\chi = \frac{C}{T - C\lambda} \tag{I.35}$$

This susceptibility has a singularity at $T = C\lambda$. Since the finite $\chi$ should be extracted from a finite $M$ in a zero field, temperatures at the singularity and below exhibit a spontaneous magnetization (or magnetic ordering). This is the *Curie-Weiss law*, which is more frequently written as:

$$\chi = \frac{C}{T - T_c}, \qquad \text{where } \; T_c = C\lambda \tag{I.36}$$

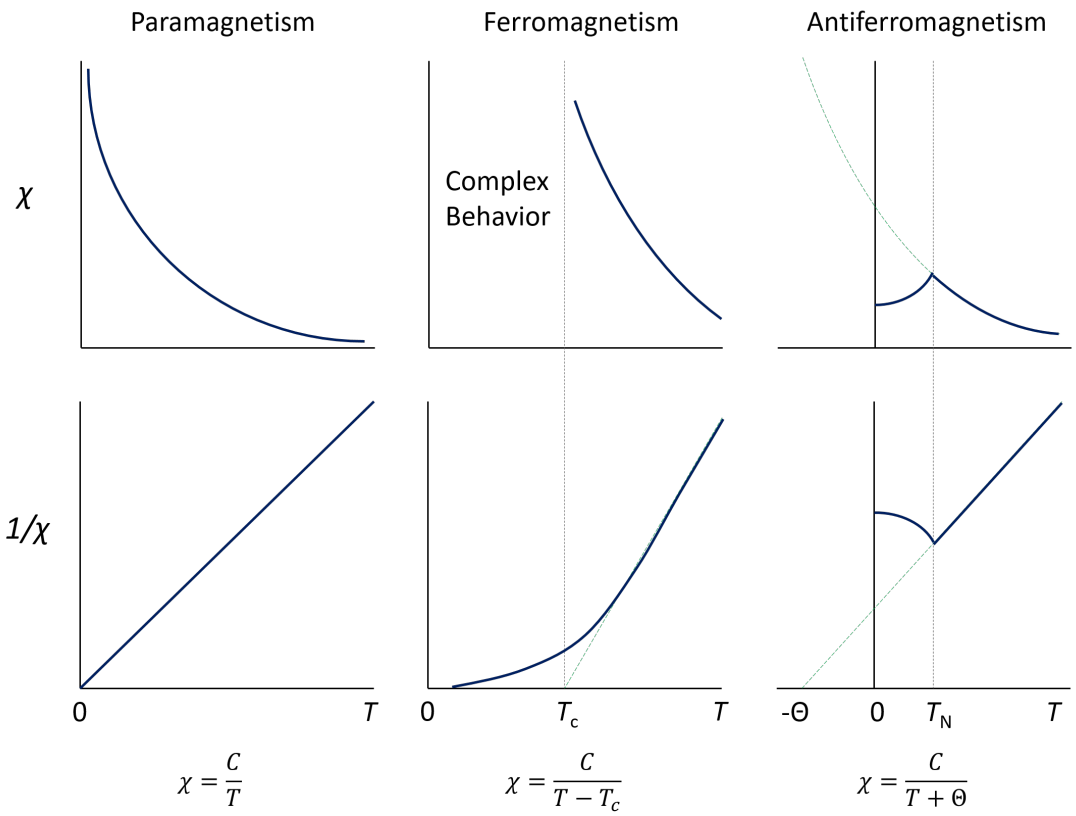


Figure I.3: Temperature dependence of the magnetic susceptibility and its reciprocal function in paramagnets, ferromagnets, and antiferromagnets.

This result shows an identical form as Curie's law for a paramagnet, with a modification. Although the measure and calculated susceptibilities of a ferromagnet near $T_c$ exhibit an inverse power divergence, this expression describes quite well the measured susceptibility variation in the paramagnetic region above the ordering temperatures. The ordering temperature, where the spontaneous magnetization occurs and/or vanishes, is called the Curie temperature, $T_c$, and the Néel temperature, $T_N$, for ferromagnetic and antiferromanetic systems, respectively. The susceptibility of an antiferromagnet is not infinite at $T_N$, but shows a weak peak or apex. Schematics of temperature-dependent susceptibilities for different systems are shown in Fig. I.3.

**Ruderman-Kittel-Kasuya-Yosida Interaction**

The Ruderman-Kittel-Kasuya-Yosida interaction, known as *RKKY interaction*, was originally proposed by M. A. Ruderman and Charles Kittel to explain unusual broad nuclear spin resonance lines observed in metallic silver. Before the introduction of the RKKY interaction, localized magnetic moments in metals were known to have ferromagnetic or antiferromagneti alignments, and not to be expected to participate in long range orders. The RKKY interaction suggested a coupling mechanism between localized magnetic moments and the conduction electrons [11–13]. The conduction electrons are polarized due to the presence of magnetic moments in a metal. The magnetic moments of the conduction electrons align parallel or anti-parallel, depending on the distance from the magnetic impurity. The Hamiltonian of the RKKY interaction is given as

$$\mathcal{H}_{RKKY} = -\frac{J^2}{g_J^2\mu_B^2}\chi(r)\mathbf{S}_i \cdot \mathbf{S}_j \tag{I.37}$$

where $\mathbf{S}_i$ and $\mathbf{S}_j$ are localized moments with the distance $r$. The magnetic susceptibility is obtained by the inverse Fourier transform,

$$\begin{aligned}\chi(r) &= \frac{1}{V}\sum_q \chi(q)e^{iq\cdot r}, \\ &= \frac{3(g_J\mu_B)^2(N/V)}{8\epsilon_F}\frac{k_F^3}{\pi}\left[\frac{\sin(2k_Fr) - 2k_Fr\cos(2k_Fr)}{(2k_Fr)^4}\right]\end{aligned} \tag{I.38}$$

Thus the exchange interaction is,

$$\mathcal{J}_{RKKY} \propto -J^2\frac{\sin(2k_Fr) - 2k_Fr\cos(2k_Fr)}{(2k_Fr)^4} \tag{I.39}$$

For small $r$, the exchange interaction is proportional to $\sim -J^2/3k_Fr$, indicating ferromagnetic; howver at larger distances $r$, its sign alternates, resulting in the change of magnetic alignments (ferromagnetic or antiferromagnetic). For very large $r$, $\mathcal{J}_{RKKY} \propto r^{-3}$ and it decreases rapidly as $r$ increases.

One significant application of the RKKY is to understand the theory of giant magneto-resistance (GMR) effect. The coupling between thin layers of magnetic materials separated by a non-magnetic spacer layer, exhibits oscillation between ferromagnetic and antiferromagnetic orderings, as a function of the distance between two magnetic layers. The GMR effect is widely used as magnetic field sensors, which are used to read data in hard disk drives, biosensors, and other devices.

### I.A.4 Superconductivity

#### Zero resistivity

Superconductivity was first discovered by H. Kamerlingh Onnes in 1911 [14]. He found that the electrical resistivity of mercury unexpectedly dropped to zero at 4.2 K, directly above liquid $^4$He boiling point. The zero-resistance at the critical temperature, $T_c$ was subsequently also observed in more than 20 other elements, indicating that superconductivity is intrinsic property of the material. This *"perfect conductivity"* was defined as the first characteristic of a superconductor.

#### Meissner effect

The second characteristic of a superconductor is *"perfect diamagnetism."* It was discovered by Meissner and Ochsenfeld in 1933 [15] by measuring the magnetic field distribution outside superconducting tin and lead samples. The samples in the applied magnetic field suddenly cancel all interior magnetic field, when the sample is cooled below its critical temperature, $T_c$. This behavior is illustrated in Fig. I.4 (a) and (b). This property is probably more important than resistance measurements since it cannot be implied by perfect conductivity alone. The perfect conductivity implies a time-independent magnetic field in the interior, where Eddy currents would be induced to maintain the field if the magnetic field is turned off; however in a superconductor, the interior field is not only independent of time, but also zero.

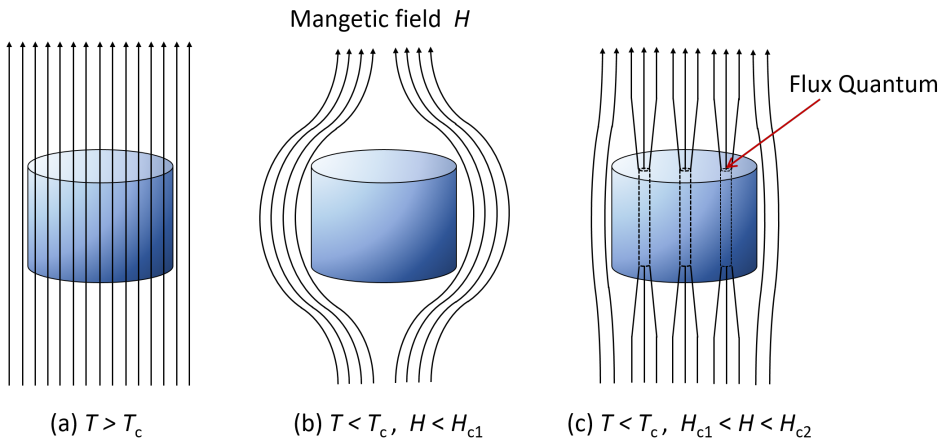


Figure I.4: Meissner effect in a superconducting sample. (a) Above $T_c$ in a constant applied magnetic field. The magnetic flux penetrates the sample. (b) Below $T_c$ the magnetic flux are ejected from the sample. (c) The type-II superconductor below $T_c$ shows mixed state. Some lines of magnetic field penetrates the sample, resulting in flux quantum.

### Critical magnetic field

A superconductor at a temperature $T$ below its $T_c$ in an applied magnetic field (not too strong) cancels the field in the interior due to the Meissner effect. If the applied field is large enough, it will eventually revert the superconductor to the normal state and penetrate the sample. The penetration occurs with increasing magnetic field and its manner depends on two distinguishable kinds of behavior, as seen in Fig. I.5. In case of the *type I superconductor*, usually observed in pure specimens of many elements, there is no penetration of magnetic flux below a critical field, $H_c$. When the applied magnetic field exceeds $H_c$, it penetrate the specimen completely, reverting the sample to the normal state. The *Type II superconductor*, mostly alloy systems, behaves in a same manner as type I superconductor in the regions below a lower critical field $H_{c1}$ and above an upper critical field $H_{c2}$. However, there is partial penetration of flux, called vortex/mixed state, when the applied magnetic field is between $H_{c1}$ and $H_{c2}$, as seen in Fig. I.4 (c).

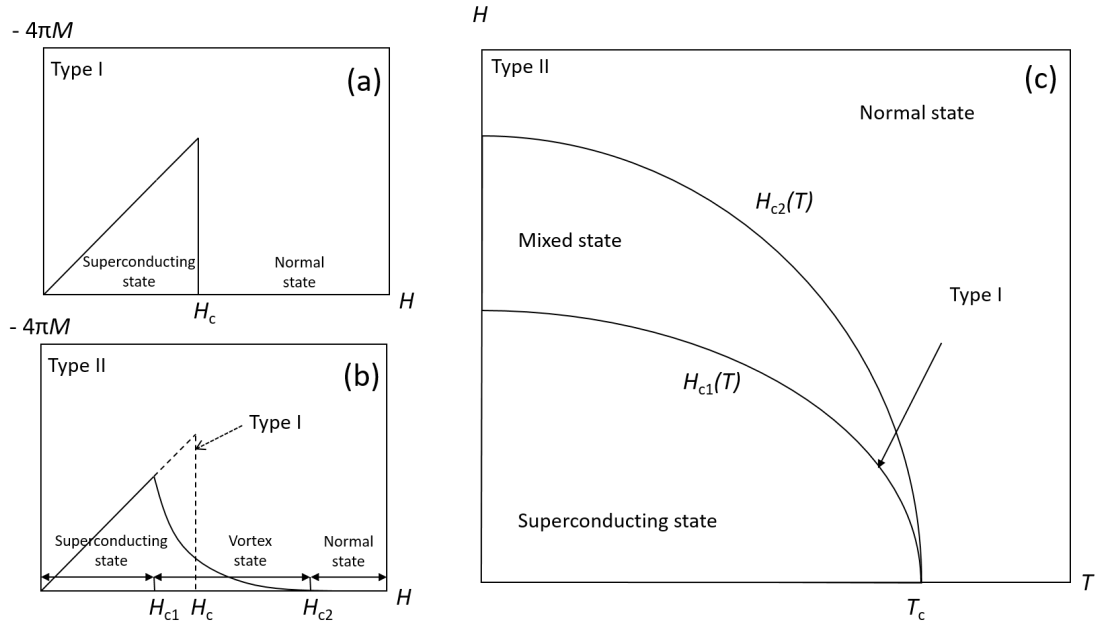


Figure I.5: (a) Magnetization curve of a type I superconductor. Below $H_c$ no magnetic field penetrates the sample. (b) Magnetization curve of a type II superconductor. Below $H_{c1}$, the behavior is similar to the type I superconductor. Between $H_{c1}$ and $H_{c2}$, it undergoes the vortex state, in which the magnetization decreases smoothly to zero as $H$ increases. (c) The phase boundary between the superconducting (and vortex) and normal states of type I and II superconductor in the $H - T$ phase diagram.

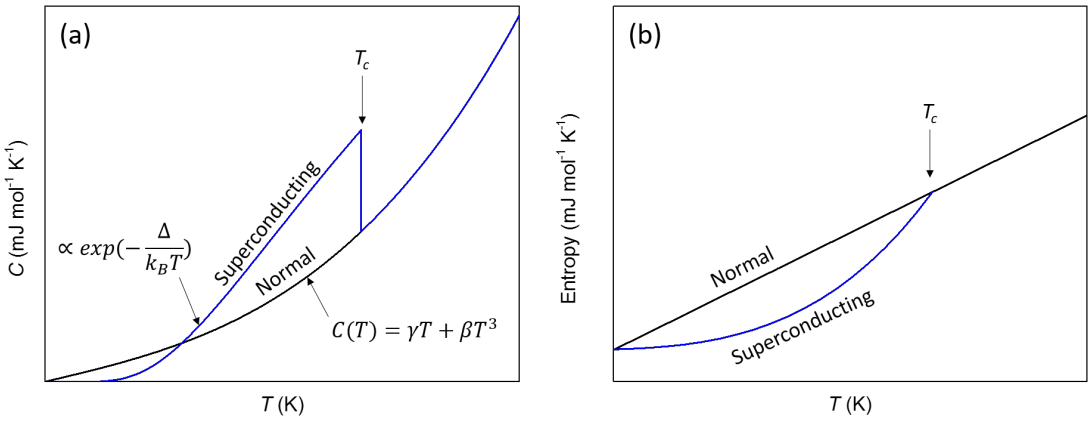


Figure I.6: (a) A schematic of the specific heat for a superconducting specimen, as a function of temperature. The normal state has electronic and lattice contributions, while superconducting system below $T_c$ follows the exponential temperature-dependence. (b) Entropy of a superconducting specimen in the normal and superconducting states as a function of temperature. Since electrons are more ordered in the superconducting state, the entropy is lower than in the normal state.

### Specific heat

The low temperature specific heat of a normal metal has the form $C(T) = \gamma T + \beta T^3$, where the first term is the electronic contribution and the second term is due to lattice vibrations. If a superconductor cools down below $T_c$, the specific heat jumps to a higher value and then decreases, eventually dropping below the value expected for a normal metal I.6. In the superconducting state, the linear term $(\gamma T)$ to the specific heat deviates from the behavior of a normal metal. It decreases much more rapidly at low temperature, having an exponential type temperature-dependence of the form $exp(-\Delta/k_B T)$. This is the characteristic temperature dependence of a system below $T_c$, in which the excited levels are separated from the ground state by an energy $2\Delta$. The superconducting energy gap will be discussed more in the following sections.

### London equations

F. London and H. London were the first to examine superconductivity in a quantitative way that a superconductor permits no magnetic field in its inte-

rior [16]. Their analysis is similar to the two-fluid description of superfluid $^4$He; a superconductor at temperature $T < T_c$ has a fraction of the total number of conduction electron, $n_s$, contributing to a supercurrent, and the remaining fraction of electrons, $n - n_s$, is in a normal state. The value of $n_s$ increases from 0 at $T_c$ to $n$ as $T \to 0$. The two relations of the microscopic electirc and magnetic fields:

$$\frac{\partial}{\partial t}\mathrm{j} = \frac{n_s e^2}{m}\mathrm{E} \tag{I.40}$$

$$\nabla \times \mathrm{j} = -\frac{n_s e^2}{mc}\mathrm{B} \tag{I.41}$$

where j is the superconducting current density, and E and B are the electric and magnetic fields within the superconductor, respectively. The Eq. I.40 describes a material conducting electricity without dissipation (i.e., a *perfect conductor*). The Eq. I.41 with Maxwell's equation

$$\nabla \times \mathrm{B} = \frac{4\pi}{c}\mathrm{j} \tag{I.42}$$

leads to

$$\nabla^2\mathrm{B} = \frac{4\pi n_s e^2}{mc^2}\mathrm{B} \tag{I.43}$$

$$\nabla^2\mathrm{j} = \frac{4\pi n_s e^2}{mc^2}\mathrm{j} \tag{I.44}$$

where

$$\lambda = \left(\frac{mc^2}{4\pi n_s e^2}\right)^{1/2} \tag{I.45}$$

These equations, in turn, describe that currents and magnetic fields could only exist within a layer of thickness, $\lambda$, from the surface of a superconductor. The $\lambda$ is defined as the London penetration depth.

**Ginzburg-Landau theory**

V. L. Ginzburg and L. D. Landau developed a macroscopic theory that describes superconductivity without examining their microscopic properties [17]. They assumed that a macroscopic quantum wave function, $\Psi(r) \equiv |\Psi(r)|e^{i\phi}$, is equivalent to an order parameter.

$$\begin{aligned} \Psi = &\quad 0 && T > T_c \\ = &|\Psi(T)| && T < T_c \end{aligned} \tag{I.46}$$

The order parameter is a complex number, similar to that in theories of superfluid $^4$He. To solve $\Psi$, the free energy is assumed to be depend on $|\Psi|$.

$$f_s = f_n + \alpha|\Psi|^2 + \frac{1}{2}\beta|\Psi|^4 + \frac{1}{2m^*}|(-i\hbar\Delta - 2e^*\mathrm{A})\Psi|^2 + \frac{|\mathrm{B}|}{2\mu_0} \tag{I.47}$$

where $f_s$ and $f_n$ are normal and superconducting states, respectively, A is the magnetic vector potential, and $\mathrm{B} = \Delta \times \mathrm{A}$ is the magnetic field, $\alpha$ and $\beta$ are treated as phenomenological parameters, and $m^*$ is an effective mass. $|\Psi|$ is found to be

$$\begin{aligned} |\Psi| = &\quad 0 && T > T_c \\ = &\left(\frac{\alpha(T_c - T)}{\beta}\right)^{1/2} && T < T_c \end{aligned} \tag{I.48}$$

The Ginzburg-Landau equations also predicted two characteristic lenghts in a superconductor, coherence length, $\xi$, and penetration depth, $\lambda$. The coherence length is the characteristic exponent of the variations of the density of superconducting component. In case of weak-coupling BCS theory, it is related to characteristic Cooper pair size.

$$\xi = \sqrt{\frac{\hbar^2}{4m|\alpha|}} \tag{I.49}$$

The penetration depth was previously introduced by the London theory. In the Ginzburg-Landau theory

$$\lambda = \sqrt{\frac{m}{4\mu_0 e^2 \Psi_0^2}} \tag{I.50}$$

The ratio of Eq. I.50 and I.49, $\kappa = \lambda/\xi$, is known as the Ginzburg-Landau parameter. It has been proposed that type I superconductors are in the range $0 < \kappa < 1/\sqrt{2}$, and type II superconductors are within $\kappa > 1/\sqrt{2}$.

**BCS theory**

J. Bardeen, L. Cooper, and J. R. Schrieffer successfully described the microscopic behavior of superconductivity in 1957. [18] In BCS theory, when electrons move through the lattice, the negative charge of the electron attracts the positive lattice atoms, resulting in a small local distortion. This local distortion has a slightly positive charge which attracts another electron, allowing electrons to use the lattices to couple to one another. The pair of two electrons with opposite momentum states (k $\uparrow$, k $\downarrow$) is known as the *"Cooper pair"*, as illustrated in Fig. I.7. This bound state with two fermions has a net integer spin, which is treated as a boson and forms a condensate at sufficiently low temperatures, leading to the superconducting state. The attraction between the electron in Cooper pairs require a temperature dependent energy gap $2\Delta$ at the Fermi level. This gap stabilizes the superconducting condensate by prohibiting other scatterings.

The complexities of BCS theory will not be discussed in full here. Rather, some important predictions by the BCS theory will be introduced below:

**Critical temperature** In zero magnetic field, the superconducting critical temperature is given by

$$k_B T_c = 1.13\hbar\omega e^{-1/N(0)V(0)} \tag{I.51}$$

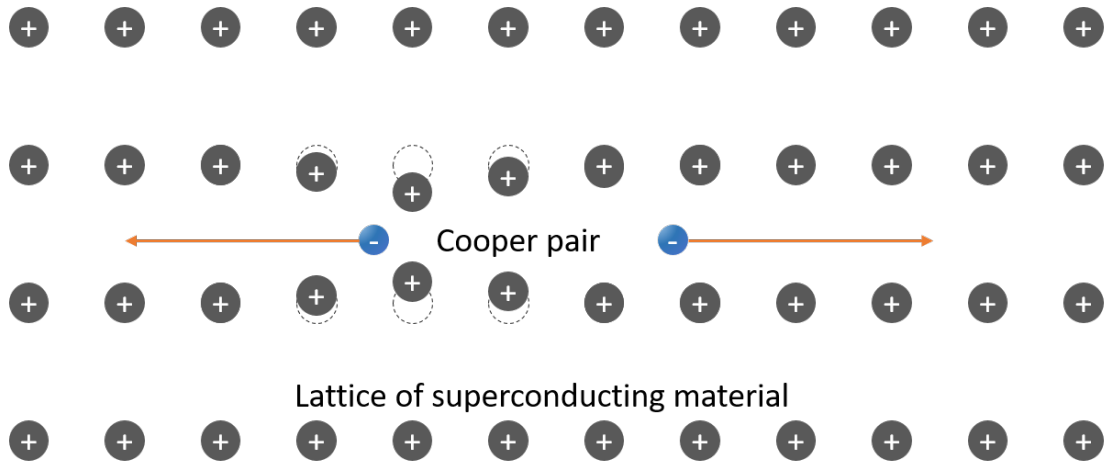


Figure I.7: The two electrons form a weak bond due to the local lattice distortion, called the Cooper pair.

where $N(0)$ is the density of states at the Fermi level, and $\hbar\omega$ and $V(0)$ are the Debye cutoff energy and the electron-phonon coupling potential, respectively.

**Energy Gap** At 0 K, the energy gap is centered on the Fermi energy and is related to the transition temperature $T_c$

$$\frac{\Delta(0)}{k_B T_c} = 1.76 \tag{I.52}$$

**Specific heat** At $T_c$, a jump in the specific heat indicates the strength of the phonon coupling

$$\frac{\Delta C(T_c)}{\gamma T_c} = 1.43 \tag{I.53}$$

BCS theory also predicts that the specific heat at low temperature has an exponential dependence given by

$$\frac{C_e}{\gamma T_c} = 1.34\left(\frac{\Delta(0)}{T}\right)^{3/2} e^{-\Delta(0)/T} \tag{I.54}$$

where $\gamma$ is the Sommerfeld coefficient in the specific heat of the metal in the normal state.

**Critical field** The BCS prediction for $H_c(T)$ is

$$\frac{H_c(T)}{H_c(0)} \approx 1 - \left(\frac{T}{T_c}\right)^2 \tag{I.55}$$

**Unconventional Superconductivity**

Thereafter the discovery of superconductivity in 1911, which is a quantum condensate of phonon-mediated Cooper pairs, a growing number of materials exhibits superconductivity and other types of correlated phenomena together, such as heavy-fermion and high $T_c$ (above the boiling temperature of liquid nitrogen) superconductivity. This reopened intense and exciting discussions of new phenomenon in condensed-matter physics community because the mechanism of these materials cannot be solely explained by the BCS theory.

The beginning of unconventional superconductivity was the discovery of heavy-fermion superconductors, where heavy electrons are usually thought to be prohibitive to pairing of electrons. However, heavy-fermion materials such as $CeCu_2Si_2$ [19], $UBe_{13}$ [20], and $UPt_3$ [21] surprisingly exhibit superconductivity with large effective masses, $m^*$, of the electrons (i.e., heavy-fermion). In the heavy-fermion systems, the competition between the Kondo effect and the RKKY interaction causes various types of ground states [22].

About the same time, the $(La,Sr)_2CuO_4$ systems [23] opened a new era of Cuprate superconductors (i.e., CuO-based superconductors). An intense and vigorous investigation of the copper-oxide materials leads to discoveries of high-$T_c$ superconducting systems, whose superconducting critical temperatures $T_c$ exceed the boiling temperature of liquid nitrogen $\sim$ 77 K: the Y-Ba-Cu-O [24], Bi-Sr-Ca-Cu-O [25], and Tl-Ca-Ba-Cu-O [26] systems. The parent compounds, with no chemical doping, are traditionally thought to be poor candidates for superconductivity; because they are Mott insulators [27], in which the electron-electron Coulomb repulsion prohibits electronic conductivity. They also have magnetic ordering (usually antiferromagnetic order) at low temperature. Upon chemical

substitutions, magnetic order can be suppressed and a superconducting "dome" is established.

Recently, superconductivity was discovered in iron-based materials (Fe-pnictide), for example, $LaO_{1-x}F_xFeAs$ in 2008 [28]. One of the most interesting properties is a complex interplay between magnetism and superconductivity, which is similar to those found in heavy-fermion superconductors and cuprates. The generic phase diagram of Fe-pnictide superconductors resembles to that of cuprates; the parent compound has magnetic ordering, which can be suppressed with increasing chemical substitution or applied pressure. On the other hand, the antiferromagnetism in Fe-pnictide parent compounds is associated with a spin-density wave (SDW) with small and variable values of ordered moment, arising from itinerant electrons. With increasing chemical substitution, the SDW is suppressed and superconductivity emerges or coexists with antiferromagnetism.

For more than the past century, many superconducting materials have been discovered, and their class of materials extended to elements, intermetallic compounds, complex oxides, and organic compounds, that have raised the $T_c$ values over the half of the room temperature at ambient pressure. A brief summary of the development of the $T_c$ values over years is shown in Fig. I.8.

**Power-law behaviors** In a conventional $s$-wave superconductor, the order parameter is isotropic and rotationally symmetric. For the $s$-wave state there is no low-lying collective mode. As we discussed in the BCS theory section, the existence of the gap in the excitation spectrum usually leads to the exponential temperature dependence of various physical quantities, including the specific heat, relaxation rate of nuclear magnetic resonance (NMR), and Knight shift. However, the order parameters for unconventional superconductors may have multiband structures or point/line nodes (zeros) in the energy gap. Due to the excitations across these points or lines, the excitation spectrum starts from zero energy. Schematics for

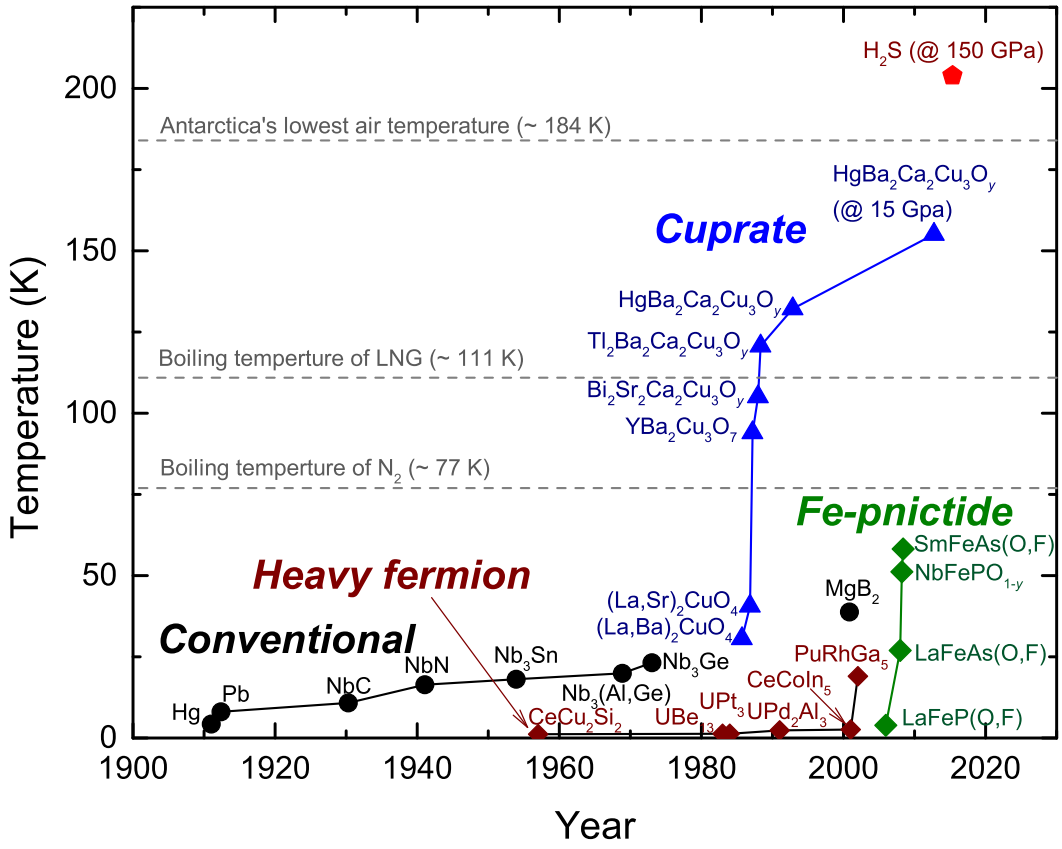


Figure I.8: The chronicle of superconductivity in a plot of critical temperature $T_c$ versus years. The $HgBa_2Ca_2Cu_3O_y$ compound holds the highest $T_c$ value around 133 K at ambient pressure.

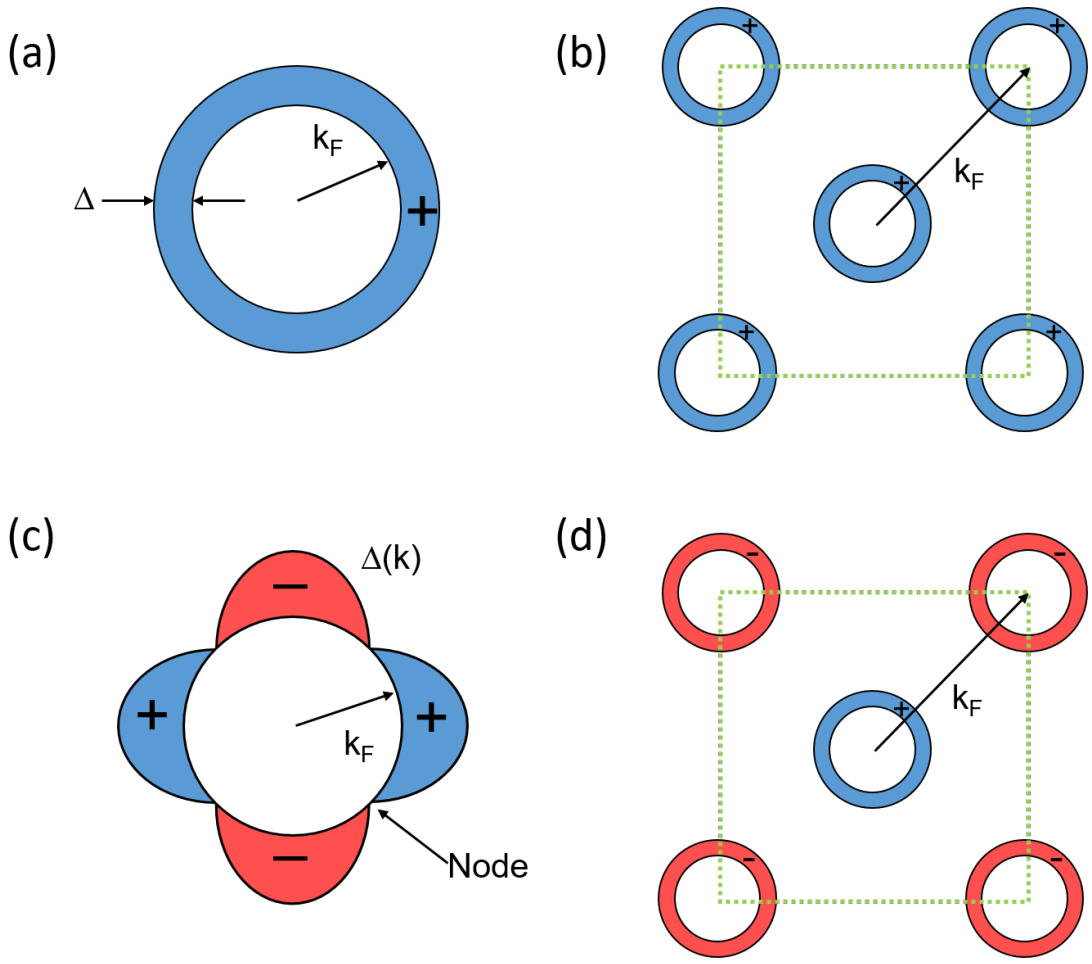


Figure I.9: A schematic of various superconducting order parameters. (a) A conventional, $s$-wave, isotropic energy gap. (b) A two-band $s$-band with the same sign, as in $MgB_2$ (c) A $d$-wave with point nodes as in the case of cuprate superconductors. (d) A $s_{\pm}$ wave with the sign change, as is believed to be the case in Fe-pnictide superconductors.

several gap structures are shown in Fig. I.9.

The case of temperature-dependent specific heat is considered as a representative example, since the specific heat data are mainly used to analyze the superconducting gap structures in this dissertation.

$$C(T) = \frac{2}{T}\int_0^\infty dE\rho(E)E^2\left(-\frac{df}{dE}\right) \qquad (T < T_c) \tag{I.56}$$

where $f(E)$ is the Fermi distribution function. Thus, the temperature dependence of the specific heat below $T_c$ depends on the topology of the gap structure as below [29].

$$C(T) \propto \begin{cases} exp(\Delta/T) & \text{Isotropic,} \\ T & \text{gapless,} \\ T^2 & \text{line nodes,} \\ T^3 & \text{point nodes.} \end{cases} \tag{I.57}$$

## I.B $BiS_2$-based superconductor

In 2012, superconductivity was discovered in $Bi_4O_4S_3$ with a transition temperature $T_c = 8.6$ K [30]. This new compound brought a lot of interests from physicists and chemists worldwide, since it has a layered crystal structure composed of superconducting $BiS_2$ layers and blocking layers of $Bi_4O_4(SO_4)_{1-x}$, where $x$ is the inclusion of $SO^{2-}$ at the interlayer sites. This layered structure is very similar to those found in high-$T_c$ cuprate and Fe-pnictide superconductors, where $T_c$ can be tuned by chemical substitutions in the blocking layers [31–34]. Soon afterwards, superconductivity was discovered in the $LaO_{0.5}F_{0.5}BiS_2$ compound by replacing the blocking layer $Bi_3O_4S$ with $La_2O_2$ [35]. These two crystal structures are compared in Fig. I.10. Both structures have an alternate stacking of the two $BiS_2$ double layers and the blocking layer.

Similarly to the case in cuprate and Fe-pnictide superconductors [33, 34, 36],

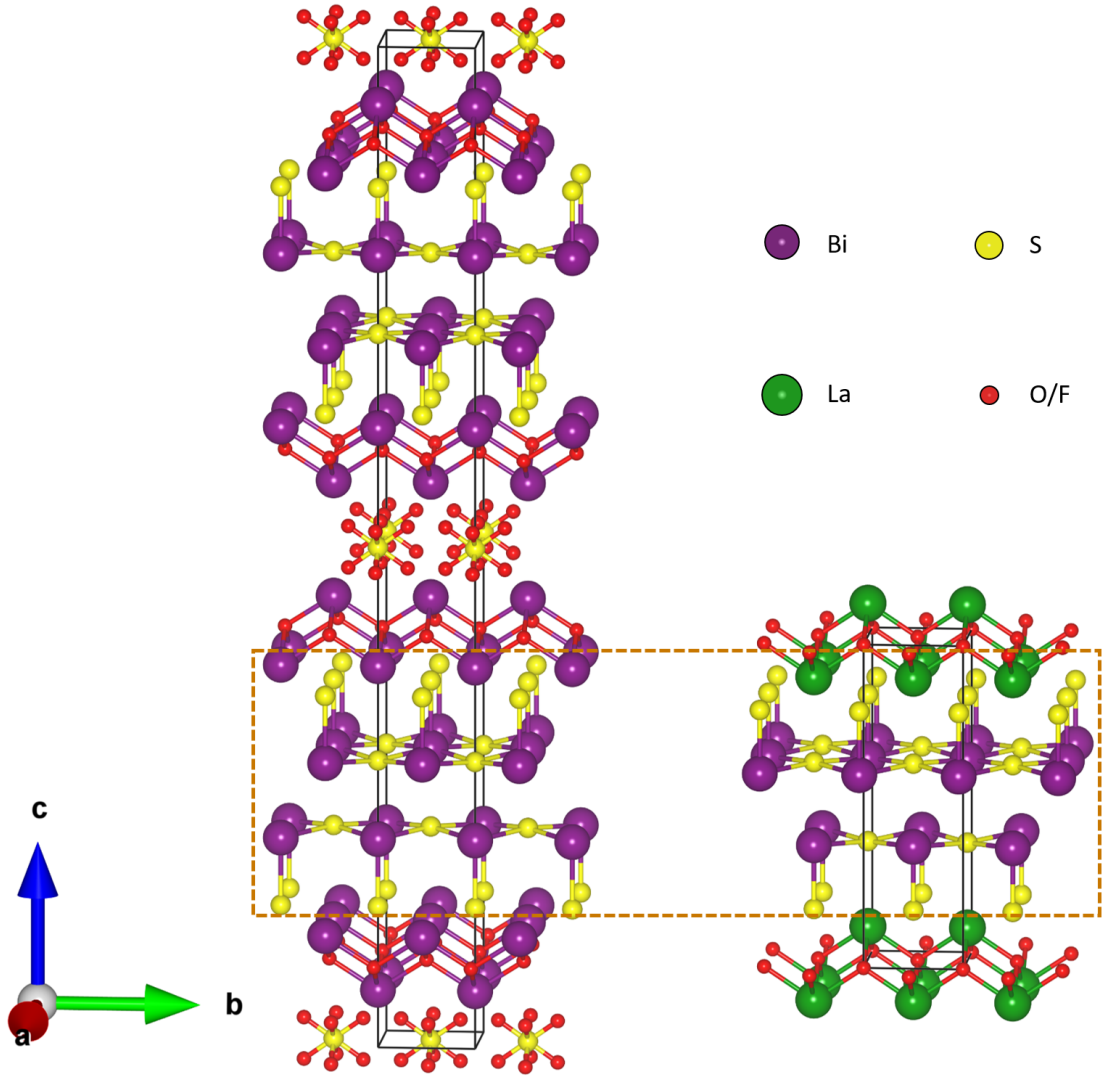


Figure I.10: Comparison of the crystal structures. *Left*: $Bi_4O_4S_3$ *Right*: $LaO_{1-x}F_xBiS_2$. A box with dashed boundaries indicates the superconducting $BiS_2$ layers, which are common to both crystal structures.

electron substitutions in the blocking layer are essential for the emergence of superconductivity in the $BiS_2$-based compounds. The parent compounds of $LaOBiS_2$ is a bad metal; in the $LnOBiS_2$ ($Ln$ = lanthanide or actinide ions) compounds, however, a partial substitution of $O^{2-}$ by $F^-$ or substitution of tetravalent elements (Ti, Zr, Hf, Th) for trivalent La induces superconductivity [30, 35, 37–39]. It was also reported that replacing non-magnetic La with magnetic rare-earth ions (Ce, Pr, Nd, Yb) increased $T_c$ up to $\sim 5.4$ K [38, 40]. Most recently, superconductivity at $T_c = 2.6$ K was reported in the $LaO_{0.5}F_{0.5}BiSe_2$ compound, whose the crystal structure with an alternative layer of $BiSe_2$ is similar to that of $LaOBiS_2$ [41–43].

Surprisingly, applying external pressure induces a structural phase transition from tetragonal to monoclinic phases, resulting in the enhancement of $T_c$ for $LnO_{1-x}F_xBiS_2$ ($Ln$ = La, Ce, Pr, Nd) [44–47]; $T_c$ is sensitive to applied pressure, similar to the case in Fe-pnictide superconductors [33, 34, 36]. The $BiS_2$ systems have some similarities to Fe-pnictide superconductors, for example, theoretical considerations of the density of states, band structure, and Fermi surface nesting [48–50].

The details concerning the nature of superconductivity in the $BiS_2$-based materials are still under debate. Several previous studies suggest that superconductivity in $Bi_4O_4S_3$ is not a bulk phenomenon and might be associated with impurity phases [51, 52]; however, recent studies on single crystals of $LnO_{1-x}F_xBiS_2$ ($Ln$ = La, Ce, Nd), grown by a flux method [43, 53–55], confirm the bulk nature of superconductivity in these class of materials. In order to have a better understanding of the intrinsic properties of $BiS_2$ superconductors, such as physical parameters determining $T_c$, the upper limit of $T_c$ for this class of materials, or the pairing mechanism, further investigations would be necessary.

## I.C Filled-Skutterudites

The skutterudites are named after the city of Skotterud, Norway. Skutterudite is a cobalt arsenide mineral that has variable amounts of nickel and iron substituting for cobalt with a general formula of $CoAs_3$. Associated minerals are arsenopyrite, native silver, erythrite, annabergite, nickeline, cobaltite, silver sulfosalts, native bismuth, calcite, siderite, barite and quartz. The filled skutterudites have the chemical formula $MT_4X_{12}$, where $M$ is an alkali metal, alkaline erath, lanthanide or actinide, $T$ is a transition metal from the Fe or Co column, and $X$ is a pnictogen. By filling the voids formed by the pnictogen ion with an alkali metal, alkaline-earth, lanthanide, or actinide ion, the filled skutterudites are formed, as shown in Fig. I.11. The unit cell of the filled skutterudite compounds contains two formula units (i.e., 34 atoms per unit cells).

The skutterudite structure consists of 8 canted octahedra, formed by $TX_6$ cages, where the $T$ ions reside in the center of each octahedron arranged in a simple cubic structure. Due to this arrangement of 8 octahedra, the 12 $X$ pnictogen ions form a distorted icosahedral cage structure, in which the $M$ ions are located in the center of the cage (see Fig. I.12). It is also found that the size of icosahderal cage increases with increasing the lattice constant of filled skutterudite systems [56]. This large size of the icosahedral cage results in the large thermal displacement parameter of the $M$ ions, preventing strong bonding with the $X$ ions. The combination of the large cage structure and weak bonding, in turn, induces so-called "rattling" modes of the $M$ "filler" ions within the rigid icosahedral cage structure. These "rattling" modes are believed to strongly scatter phonons and thus decrease the thermal conductivity, $\kappa$ [57–59]. In addition, many of these compounds have large features in the electronic density of states near the Fermi level, leading to enhanced thermoelectric power $S$ at low temperature. These two aspects give rise to interest in thermoelectric applications since the thermoelectric efficiency depends on the dimensionless figure of merit, $ZT = \sigma S^2/\kappa$.

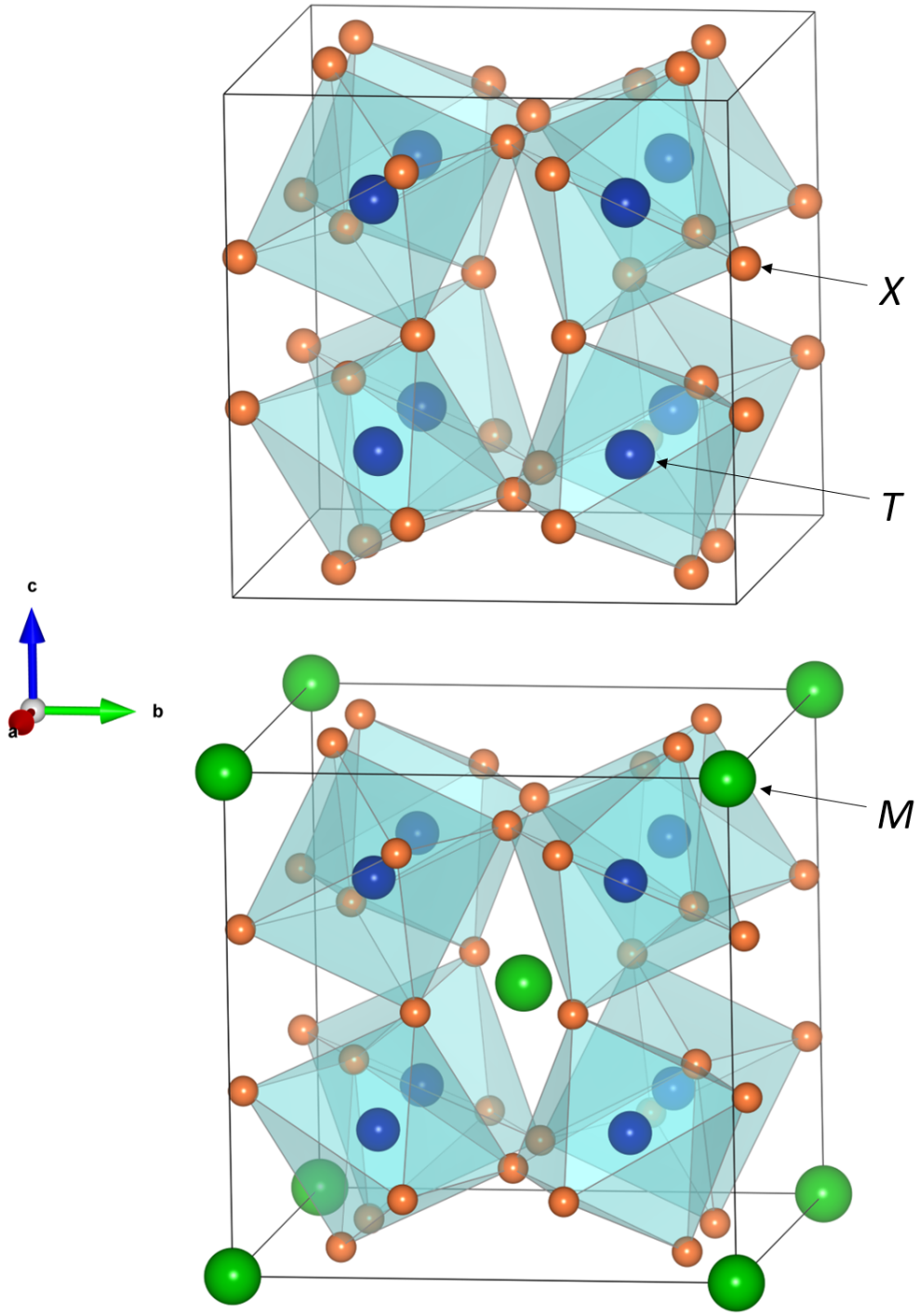


Figure I.11: *Top*: The (unfilled) Skutterudite structure with the chemical formula $TX_3$. *Bottom*: The filled Skutterudite structure with the chemical formula $MT_4X_{12}$. The voids of the pnictogen ions (the $X$ ions) are filled with an alkali metal, alkaline erath, lanthanide or actinide (the $M$ "filler" ions).

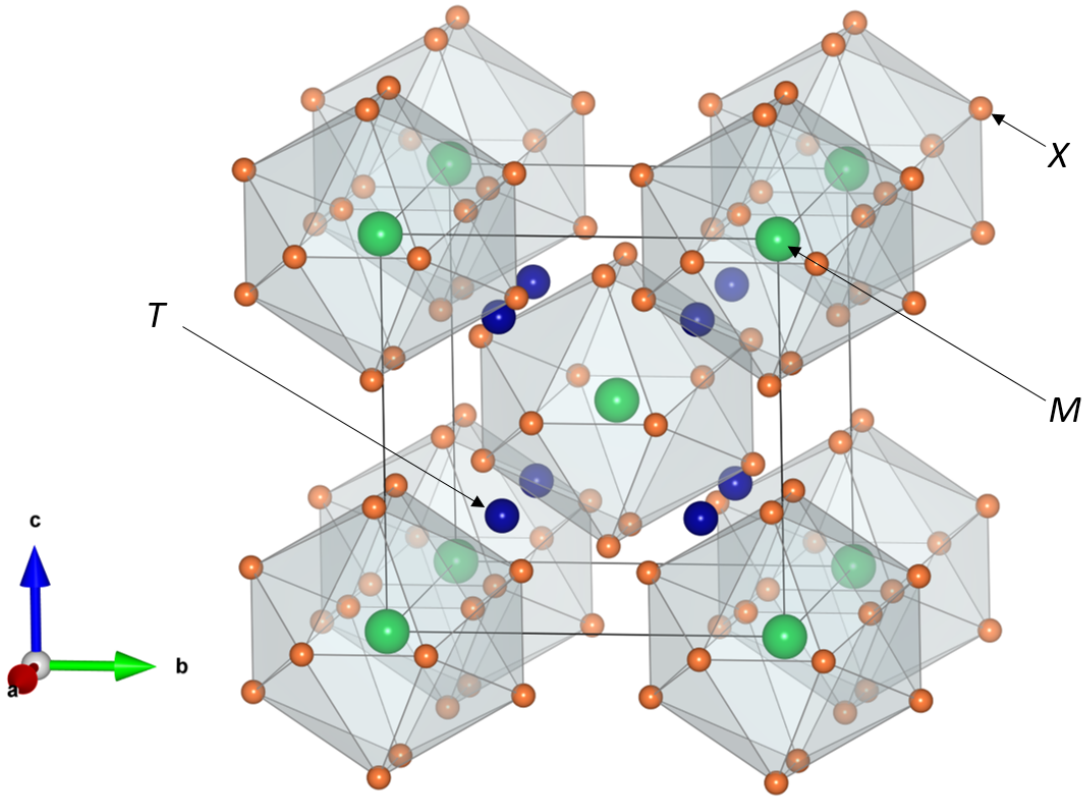


Figure I.12: The $X$ pnictogen ions form distorted icosahedral cages, in which the "filler" $M$ ions reside in the cages.

Besides the thermoelectric properties of the filled skutterudite compounds, they exhibit various types of correlated electron phenomena: conventional BCS-type superconductivity, unconventional superconductivity, Kondo lattice behavior, valence fluctuations, non-Fermi liquid behavior, heavy fermion behavior, Kondo insulator behavior, metal-insulator transitions, magnetic orderings, spin fluctuations, quadrupolar order, and etc [60–66].

Among the filled skutterudite compounds, the $PrOs_4Sb_{12}$ system is particularly interesting, since it is the first discovered Pr-based heavy fermion superconductor ($T_c = 1.85$ K and $H_{c2}(0) = 2.5$ T [67, 68]). Several peculiar correlated electron phenomena have been reported in its superconducting state: time reversal symmetry breaking [69], different superconducting phases with point nodes in the energy gap [70, 71], potential spin triplet pairing of electrons [72], and multiple superconducting bands [71, 73, 74]. Moreover, superconductivity emerges from a heavy Fermi liquid ground state where $m^* \sim 50m_e$ [67, 68]. It is seen that the specific heat jump $\Delta \sim \gamma T_c$ is large [68], indicating that the heavy quasiparticles are involved in its superconducting properties.

Recently, it has been reported that a new member of filled-skutterudite compounds with chemical formula $M Pt_4Ge_{12}$ ($M$ = alkali metal, alkaline erath, lanthanide or actinide) can be formed by standard synthesis techniques [60–66]. Superconductivity is observed in the compounds with $M$ = Sr, Ba, La, Pr, and Th. For (Sr, Ba)$Pt_4Ge_{12}$, with $T_c = 5.35$ and 5.10 K, respectively, BCS-like superconductivity is observed and emerged from electron-phonon interactions originating from the Pt-Ge cage structure. For (La, Pr)$Pt_4Ge_{12}$, superconductivity occurs at interestingly high temperatures, $T_c \sim 8$ K, and $ThPt_4Ge_{12}$ was found to be a clean-limit strong-coupling superconductor with $T_c = 4.62$ K.

$PrPt_4Ge_{12}$ is an unconventional superconductor with $T_c \sim 7.8$ K and exhibit several similar behaviors to those observed in $PrOs_4Sb_{12}$. Transverse Muon Spin Relaxation ($\mu$SR) and specific heat ($C$) measurements reveal that point nodes in its superconducting energy gap and other zero-field $\mu$SR measurements have pro-

vided evidence for time reversal symmetry breaking (TRSB) in its superconducting state [66]. Upon Ce substitution in the Pr site, the suppression of superconductivity was observed with increasing Ce concentration with positive curvature up to $x = 0.5$. Comparisons of the $C/T$ profile in the superconducting state shows that the $C(T)/T$ data are best described by a $T^3$ dependence for $x = 0$ and an $e^{-\Delta/T}$ dependence for $x \geq 0.05$, indicating a crossover from a nodal to nodeless superconducting energy gap or the suppression from multiple to single BCS type superconducting energy bands with increasing Ce concentration [75].

## Bibliography


[1] P. W. Anderson, Science **177**, 393 (1972).

[2] L. D. Landau, J. Exp. Theor. Phys. **30**, 1058 (1956).

[3] I. Walker, F. Grosche, D. Freye, and G. Lonzarich, Physica C: Superconductivity **282**, 303 (1997).

[4] P. A. Lee, N. Nagaosa, and X.-G. Wen, Rev. Mod. Phys. **78**, 17 (2006).

[5] D. L. Cox, Phys. Rev. Lett. **59**, 1240 (1987).

[6] O. O. Bernal, D. E. MacLaughlin, A. Amato, R. Feyerherm, F. N. Gygax, A. Schenck, R. H. Heffner, L. P. Le, G. J. Nieuwenhuys, B. Andraka, H. v. Löhneysen, O. Stockert, and H. R. Ott, Phys. Rev. B **54**, 13000 (1996).

[7] A. H. Castro Neto, G. Castilla, and B. A. Jones, Phys. Rev. Lett. **81**, 3531 (1998).

[8] N. Ashcroft and N. Mermin, *Solid State Physics* (Saunders College, Philadelphia, 1976).

[9] C. Kittel, *Introduction to Solid State Physics* (John Wiley & Sons, Inc., New York, 1986), 6th ed.

[10] H. A. Bethe, Z. Physik **71**, 205 (1931).

[11] M. A. Ruderman and C. Kittel, Phys. Rev. **96**, 99 (1954).

[12] T. Kasuya, Progress of Theoretical Physics **16**, 45 (1956).

[13] K. Yosida, Phys. Rev. **106**, 893 (1957).

[14] H. K. Onnes, Commun. Phys. Lab. Univ. Leiden pp. 120b,122b,124c (1911).

[15] W. Meissner and R. Ochsenfeld, Naturwissenschaften **21**, 787 (1933).

[16] F. London and H. London, Pro. Roy. Soc. **149**, 71 (1935).

[17] L. D. Landau and V. L. Ginzburg, Eksp. Teor. Fiz. **20** (1950).

[18] J. Bardeen, L. N. Cooper, and J. R. Schrieffer, Phys. Rev. **108**, 1175 (1957).

[19] F. Steglich, J. Aarts, C. D. Bredl, W. Lieke, D. Meschede, W. Franz, and H. Schäfer, Phys. Rev. Lett. **43**, 1892 (1979).

[20] H. R. Ott, H. Rudigier, Z. Fisk, and J. L. Smith, Phys. Rev. Lett. **50**, 1595 (1983).

[21] G. R. Stewart, Z. Fisk, J. O. Willis, and J. L. Smith, Phys. Rev. Lett. **52**, 679 (1984).

[22] S. Doniach, Physica B+C **91**, 231 (1977).

[23] J. G. Bednorz and K. A. Müller, Zeitschrift für Physik B Condensed Matter **64**, 189 (1986).

[24] M. K. Wu, J. R. Ashburn, C. J. Torng, P. H. Hor, R. L. Meng, L. Gao, Z. J. Huang, Y. Q. Wang, and C. W. Chu, Phys. Rev. Lett. **58**, 908 (1987).

[25] H. Maeda, Y. Tanaka, M. Fukutomi, and T. Asano, Jpn. J. Appl. Phys. **27**, L209 (1988).

[26] Z. Z. Sheng and A. M. Hermann, Nature **332**, 138 (1988).

[27] P. W. ANDERSON, Science **235**, 1196 (1987).

[28] Y. Kamihara, T. Watanabe, M. Hirano, and H. Hosono, J. Am. Chem. Soc. **130**, 3296 (2008).

[29] M. Sigrist and K. Ueda, Rev. Mod. Phys. **63**, 239 (1991).

[30] Y. Mizuguchi, H. Fujihisa, Y. Gotoh, K. Suzuki, H. Usui, K. Kuroki, S. Demura, Y. Takano, H. Izawa, and O. Miura, Phys. Rev. B **86**, 220510(R) (2012).

[31] E. Dagotto, Rev. Mod. Phys. **66**, 763 (1994).

[32] P. A. Lee, N. Nagaosa, and X.-G. Wen, Rev. Mod. Phys. **78**, 17 (2006).

[33] J. Paglione and R. L. Greene, Nat. Phys. **6**, 645 (2010).

[34] D. C. Johnston, Adv. Phys. **59**, 803 (2010).

[35] Y. Mizuguchi, S. Demura, K. Deguchi, Y. Takano, H. Fujihisa, Y. Gotoh, H. Izawa, and O. Miura, J. Phys. Soc. Jpn. **81**, 114725 (2012).

[36] G. R. Stewart, Rev. Mod. Phys. **83**, 1589 (2011).

[37] Y. Mizuguchi, T. Hiroi, J. Kajitani, H. Takatsu, H. Kadowaki, and O. Miura, J. Phys. Soc. Jpn. **83**, 053704 (2014).

[38] D. Yazici, K. Huang, B. D. White, A. H. Chang, A. J. Friedman, and M. B. Maple, Phil. Mag. **93**, 673 (2013).

[39] D. Yazici, K. Huang, B. D. White, I. Jeon, V. W. Burnett, A. J. Friedman, I. K. Lum, M. Nallaiyan, S. Spagna, and M. B. Maple, Phys. Rev. B **87**, 174512 (2013).

[40] S. Demura, Y. Mizuguchi, K. Deguchi, H. Okazaki, H. Hara, T. Watanabe, S. James Denholme, M. Fujioka, T. Ozaki, H. Fujihisa, Y. Gotoh, O. Miura, T. Yamaguchi, H. Takeya, and Y. Takano, J. Phys. Soc. Jpn. **82**, 033708 (2013).

[41] A. Krzton-Maziopa, Z. Guguchia, E. Pomjakushina, V. Pomjakushin, R. Khasanov, H. Luetkens, P. K. Biswas, A. Amato, H. Keller, and K. Conder, J. Phys.: Condens. Matter **26**, 215702 (2014).

[42] M. Tanaka, M. Nagao, Y. Matsushita, M. Fujioka, S. J. Denholme, T. Yamaguchi, H. Takeya, and Y. Takano, J. Solid State Chem. **219**, 168 (2014).

[43] M. Nagao, M. Tanaka, S. Watauchi, I. Tanaka, and Y. Takano, J. Phys. Soc. Jpn. **83**, 114709 (2014).

[44] H. Kotegawa, Y. Tomita, H. Tou, H. Izawa, Y. Mizuguchi, O. Miura, S. Demura, K. Deguchi, and Y. Takano, J. Phys. Soc. Jpn. **81**, 103702 (2012).

[45] C. T. Wolowiec, D. Yazici, B. D. White, K. Huang, and M. B. Maple, Phys. Rev. B **88**, 064503 (2013).

[46] C. T. Wolowiec, B. D. White, I. Jeon, D. Yazici, K. Huang, and M. B. Maple, J. Phys.: Condens. Matter **25**, 422201 (2013).

[47] T. Tomita, M. Ebata, H. Soeda, H. Takahashi, H. Fujihisa, Y. Gotoh, Y. Mizuguchi, H. Izawa, O. Miura, S. Demura, K. Deguchi, and Y. Takano, J. Phys. Soc. Jpn. **83**, 063704 (2014).

[48] T. Yildirim, Phys. Rev. B **87**, 020506 (2013).

[49] H. Usui, K. Suzuki, and K. Kuroki, Phys. Rev. B **86**, 220501 (2012).

[50] X. B. Wang, S. M. Nie, H. P. Wang, P. Zheng, P. Wang, T. Dong, H. M. Weng, and N. L. Wang, Phys. Rev. B **90**, 054507 (2014).

[51] I. C. Sathish, H. L. Feng, Y. Shi, and K. Yamaura, J. Phys. Soc. Jpn. **82**, 074703 (2013).

[52] S. L. Liu, J. Superconductivity Novel Mag. **26**, 3411 (2013).

[53] J. Liu, D. Fang, Z. Wang, J. Xing, Z. Du, S. Li, X. Zhu, H. Yang, and H.-H. Wen, Europhys. Lett. **106**, 67002 (2014).

[54] M. Nagao, S. Demura, K. Deguchi, A. Miura, S. Watauchi, T. Takei, Y. Takano, N. Kumada, and I. Tanaka, J. Phys. Soc. Jpn. **82**, 113701 (2013).

[55] M. Nagao, A. Miura, S. Demura, K. Deguchi, S. Watauchi, T. Takei, Y. Takano, N. Kumada, and I. Tanaka, Solid State Comm. **178**, 33 (2014).

[56] B. J. Braun and W. Jeitschko, J. Solid State Chem. **32** (1980).

[57] B. C. Sales, *Filled skutterudites in Handbook on the Physics and Chemistry of the Rare Earths*, vol. 33 (Elsevier Science, Amsterdam, 2002).

[58] M. B. Maple, Z. Henkie, R. E. Baumbach, T. A. Sayles, N. P. Butch, P.-C. Ho, T. Yanagisawa, W. M. Yuhasz, R. Wawryk, T. Cichorek, and A. Pietraszko, Journal of the Physical Society of Japan **77**, 7 (2008).

[59] H. Sato, D. Kikuchi, K. Tanaka, M. Ueda, H. Aoki, T. Ikeno, S. Tatsuoka, K. Kuwahara, Y. Aoki, M. Kohgi, H. Sugawara, K. Iwasa, and H. Harima, J. Phys. Soc. Jpn. **77SA**, 1 (2008).

[60] E. Bauer, A. Grytsiv, X.-Q. Chen, N. Melnychenko-Koblyuk, G. Hilscher, H. Kaldarar, H. Michor, E. Royanian, G. Giester, M. Rotter, R. Podloucky, and P. Rogl, Phys. Rev. Lett. **99**, 217001 (2007).

[61] E. Bauer, X.-Q. Chen, P. Rogl, G. Hilscher, H. Michor, E. Royanian, R. Podloucky, G. Giester, O. Sologub, and A. P. Gonçalves, Phys. Rev. B **78**, 064516 (2008).

[62] R. Gumeniuk, W. Schnelle, H. Rosner, M. Nicklas, A. Leithe-Jasper, and Y. Grin, Phys. Rev. Lett. **100**, 017002 (2008).

[63] M. Toda, H. Sugawara, K. ichi Magishi, T. Saito, K. Koyama, Y. Aoki, and H. Sato, Journal of the Physical Society of Japan **77**, 124702 (2008).

[64] F. Kanetake, H. Mukuda, Y. Kitaoka, H. Sugawara, K. Magishi, K. Itoh, and E. Haller, Physica C: Superconductivity **470, Supplement 1**, S703 (2010).

[65] R. Gumeniuk, M. Schöneich, A. Leithe-Jasper, W. Schnelle, M. Nicklas, H. Rosner, A. Ormeci, U. Burkhardt, M. Schmidt, U. Schwarz, M. Ruck, and Y. Grin, New Journal of Physics **12**, 103035 (2010).

[66] A. Maisuradze, W. Schnelle, R. Khasanov, R. Gumeniuk, M. Nicklas, H. Rosner, A. Leithe-Jasper, Y. Grin, A. Amato, and P. Thalmeier, Phys. Rev. B **82**, 024524 (2010).

[67] E. Bauer, A. Slebarski, E. Freeman, N. Frederick, B. Taylor, C. Sirvent, and M. Maple, Physica B: Condensed Matter **312-313**, 230 (2002).

[68] M. Maple, N. Frederick, P.-C. Ho, W. Yuhasz, and T. Yanagisawa, Journal of Superconductivity and Novel Magnetism **19**, 299 (2006).

[69] Y. Aoki, A. Tsuchiya, T. Kanayama, S. R. Saha, H. Sugawara, H. Sato, W. Higemoto, A. Koda, K. Ohishi, K. Nishiyama, and R. Kadono, Phys. Rev. Lett. **91**, 067003 (2003).

[70] K. Izawa, Y. Nakajima, J. Goryo, Y. Matsuda, S. Osaki, H. Sugawara, H. Sato, P. Thalmeier, and K. Maki, Phys. Rev. Lett. **90**, 117001 (2003).

[71] R. W. Hill, S. Li, M. B. Maple, and L. Taillefer, Phys. Rev. Lett. **101**, 237005 (2008).

[72] E. E. M. Chia, M. B. Salamon, H. Sugawara, and H. Sato, Phys. Rev. Lett. **91**, 247003 (2003).

[73] G. Seyfarth, J. P. Brison, M.-A. Méasson, D. Braithwaite, G. Lapertot, and J. Flouquet, Phys. Rev. Lett. **97**, 236403 (2006).

[74] L. Shu, D. E. MacLaughlin, W. P. Beyermann, R. H. Heffner, G. D. Morris, O. O. Bernal, F. D. Callaghan, J. E. Sonier, W. M. Yuhasz, N. A. Frederick, and M. B. Maple, Phys. Rev. B **79**, 174511 (2009).

[75] K. Huang, L. Shu, I. K. Lum, B. D. White, M. Janoschek, D. Yazici, J. J. Hamlin, D. A. Zocco, P.-C. Ho, R. E. Baumbach, and M. B. Maple, Phys. Rev. B **89**, 035145 (2014).

# Chapter II

# Experimental Details

## II.A Sample Synthesis

Skillful sample synthesis is a key step to study correlated $f-$electron systems. Various types of synthesis techniques can be used to produce samples for characterization. The appropriate technique has to be chosen depending on crystal structures as well as the type of characterizations (or measurements) to be performed. Single crystals have single grain orientation, and low impurity concentrations, resulting in higher sample quality; however it is usually more difficult to synthesize, especially in large quantities. Since chemical substitution studies are exploratory to new type of physics and bulk types of measurements are mainly performed, techniques for polycrystalline growth are mainly used in the work of this dissertation.

### II.A.1 Solid-state reaction

A solid-state reaction is very straight-forward and accessible method to synthesis crystals. The starting materials (chunks, powders) are mixed in the correct stoichiometric ratios, ground to find powders, and placed in an appropriate container, which does not react with any of starting materials. The mixture is heated

to high enough temperatures below the melting points of the starting materials. To control atmospheric conditions, quartz ampoules (Fig. II.1 (b)) are used to evacuate or to introduce inert gases during heating processes. With appropriate conditions, thermal energy overcomes the free energy constraints and materials or mixtures change into other configurations. Since the reaction usually happens at the interface of the starting materials, it is important to promote homogeneity of the samples; the sample is ground to powdered and reheated. The process is repeated several times until chemical homogeneity is achieved. To further promote chemical reactions between individual grains, the mixture is compressed into a dense pellet, as shown in Fig. II.1 (c), by using various die-kits and a cold isostatic press.

### II.A.2 Arc-melting method

Another common technique for synthesizing polycrystalline samples or metallic alloys is an arc-melting method; this method works on conducting or semiconducting materials. The arc furnace has a 2% lanthanated tungsten electrode to produce an arc over a water cooled copper hearth. The furnace is evacuated with a vacuum and filled with a high purity argon atmosphere and to capture additional oxygen, a zirconium getter is employed. The starting materials, usually raw elements, are weighed and mixed in the correct stoichiometric ratio. Upon application of high voltage, an electric arc flows from tungsten electrode to the copper hearth. When the arc is close enough to the starting materials, it will move to the lower resistance material and starts to melt materials by Joule heating. The components are melted then transforming to a homogeneous liquid mixture. The final sample will be boule- or ball-like shape, as shown in Fig. II.2 (c). Since arc melting is a violent and rapid process, samples likely have point, line, planar defects or dislocations. To promote crystalline homogeneity, usually an additional annealing process

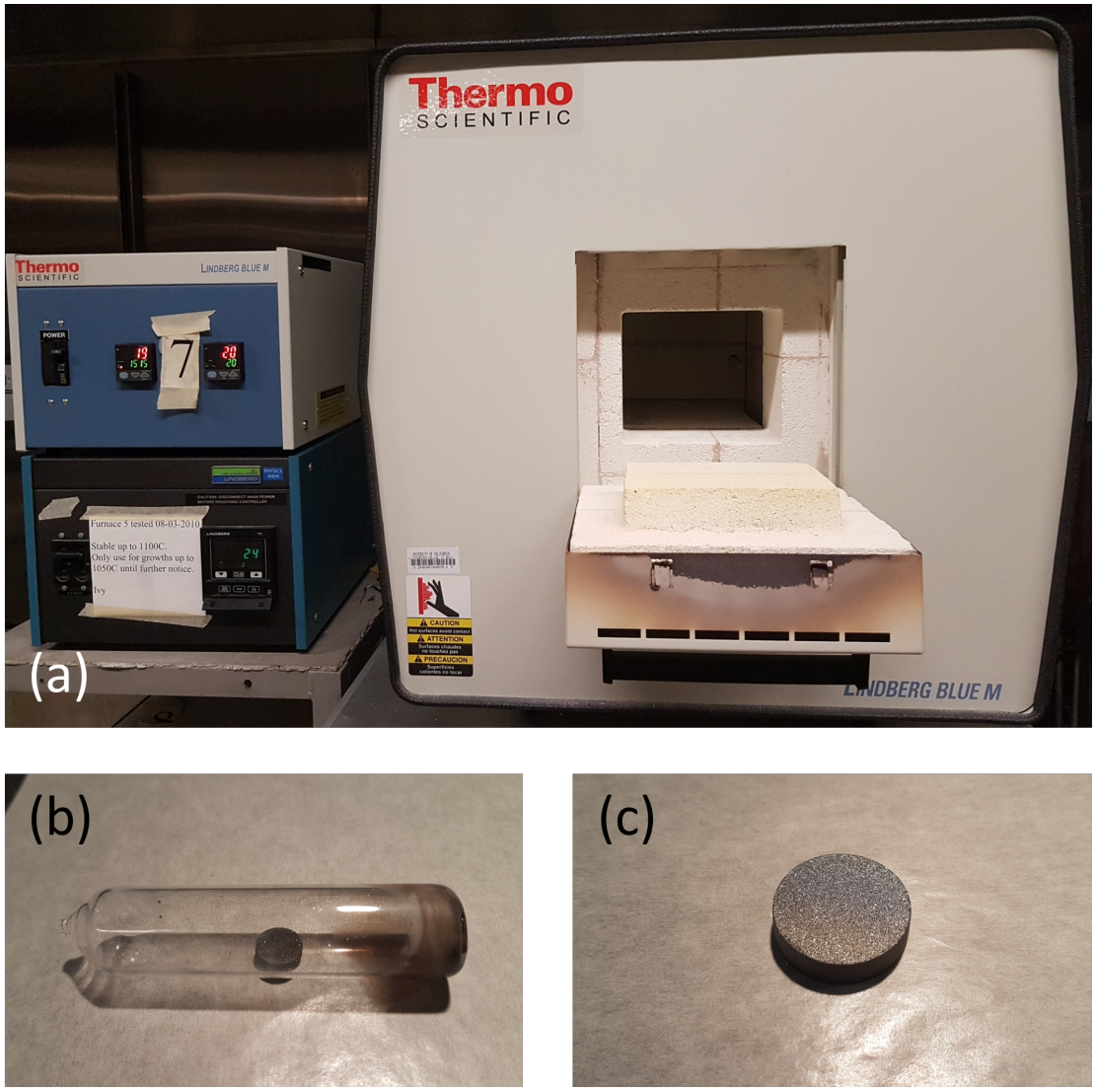


Figure II.1: (a) A box furnace with its control console. (b) A quartz ampoule containing a sample under Argon atmosphere, after heating process. (c) A representative sample for $La_{1-x}Y_xO_{0.5}F_{0.5}BiS_2$ in a dense pellet form.

is employed after arc melting, with the same technique as discussed in Fig. II.1.

## II.B Characterization

Various measurement techniques are used to characterize samples. These techniques allow us to determine crystal structures, ordering temperatures, and transport, thermal, and magnetic properties of samples. A few of bulk type measurements will be introduced here; powder X-ray diffraction, electrical resistivity, magnetic susceptibility, and specific heat measurements.

### II.B.1 Powder X-ray Diffraction

A sample is ground into a fine powder, using mortar and pestle until the grain sizes are minimized. The powder is mixed with petrolatum and then the mixture is affixed to a glass slide as a thin film-like form with homogeneous thickness, as shown in Fig. II.3 (b). The room temperature structure of the specimens was determined by powder x-ray diffractometry, using a Bruker D8 Discover diffractometer with 40 kV and 200 mA settings. The machine shines monochromatic x-ray ($\lambda =$ 1.540562 Å), generated by a filtered and rotating copper anode producing Cu-$K_\alpha$ x-ray radiation, on the glass slides. The beam passes through all possible orientations of the powdered single/poly crystals while the coordinated detector span a portion of the surrounding Ewald sphere, as shown in Fig. II.3 (a). A powder x-ray diffraction pattern consists of a set of Bragg reflection peaks, which occur when Bragg's law, $n\lambda = 2d\sin\theta$, is satisfied for given reflection planes. The obtained intensity($I$)-position($2\theta$) data is quantitatively analyzed by the GSAS+EXPGUI program [1, 2], using a non-linear and least-squares regression algorithm, called Rivetveld refinement [3]. From the Rietveld refinement technique, the crystal structure of a sample including space group, lattice constants, atomic position, occupancy of atomic sites, bond angles, and other parameters, was obtained. The

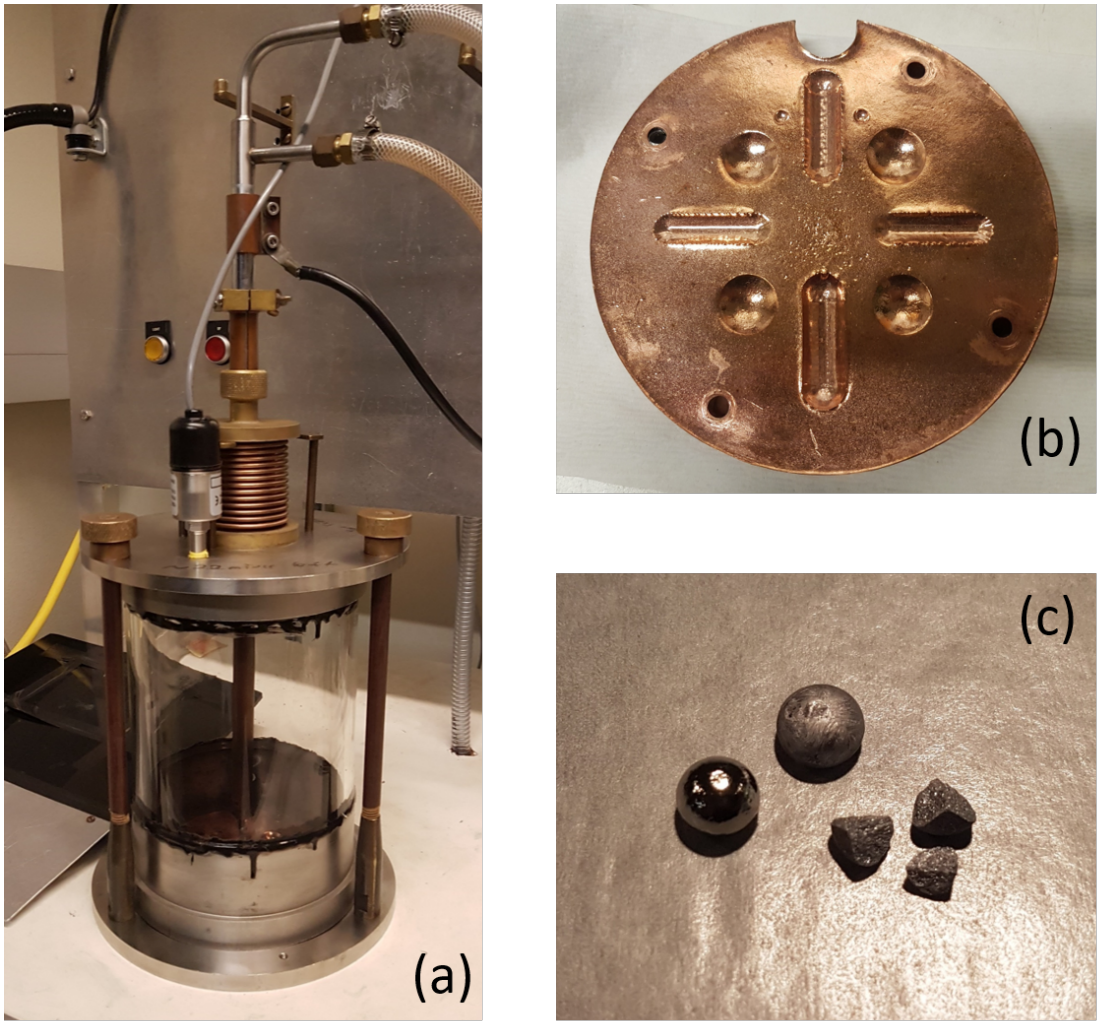


Figure II.2: (a) The arc furnace system. (b) Copper hearth, with several dent spaces for samples and zirconium getter. (c) Various shapes of $Pr_{1-x}Eu_xPt_4Ge_{12}$ samples, prepared by the arc-melting method.

observation of additional Bragg reflection peaks beside the parent phase also provides a rough estimate for the quantities of parent and impurity phases in the sample.

### II.B.2 Electrical Resistivity

The measurements of electrical resistivity were conducted using the standard four-wire configuration. First, each sample is shaped to a long rectangular bar by carefully cutting and sanding the sample. In order to facilitate low contact resistances, gold-contact pads were sputtered on the polished surface of samples by a Hummer 6.2 sputterer, then four independent leads were attached using gold wires by a two-part silver epoxy. The four leads are separated into two pairs: the two outside leads carry the excitation current throughout the sample and the other two inside leads measure the voltage drop across them. Finally, the electrical resistivity of samples is estimated, using a relation $\rho = \alpha \cdot R$, where $\alpha = (w \cdot t)/l$ and $R$ is resistance of samples in units of cm·Ω. An example is shown in Fig. II.4. A Linear Research LR-700 AC resistance bridge was employed in a home-built $He^4$ dewar to measure the temperature-dependent resistance values in the temperature ranges from 300 K to 1.1 K.

### II.B.3 Magnetic Susceptibility

The magnetic susceptibility of samples was performed by using a Quantum Design Magnetic Properties Measurement System (MPMS), equipped with a 7 tesla magnet in the temperature ranges between 2 and 400 K. The sample travels vertically through two sets of detection coils; each set is comprised of two single coils wound oppositely to measure periodic signal of the magnitude of the moment. The Superconducting Quantum Interference Device (SQUID), comprised of two superconductors separated by a thin insulating layer, i.e., a Josephson Junction,

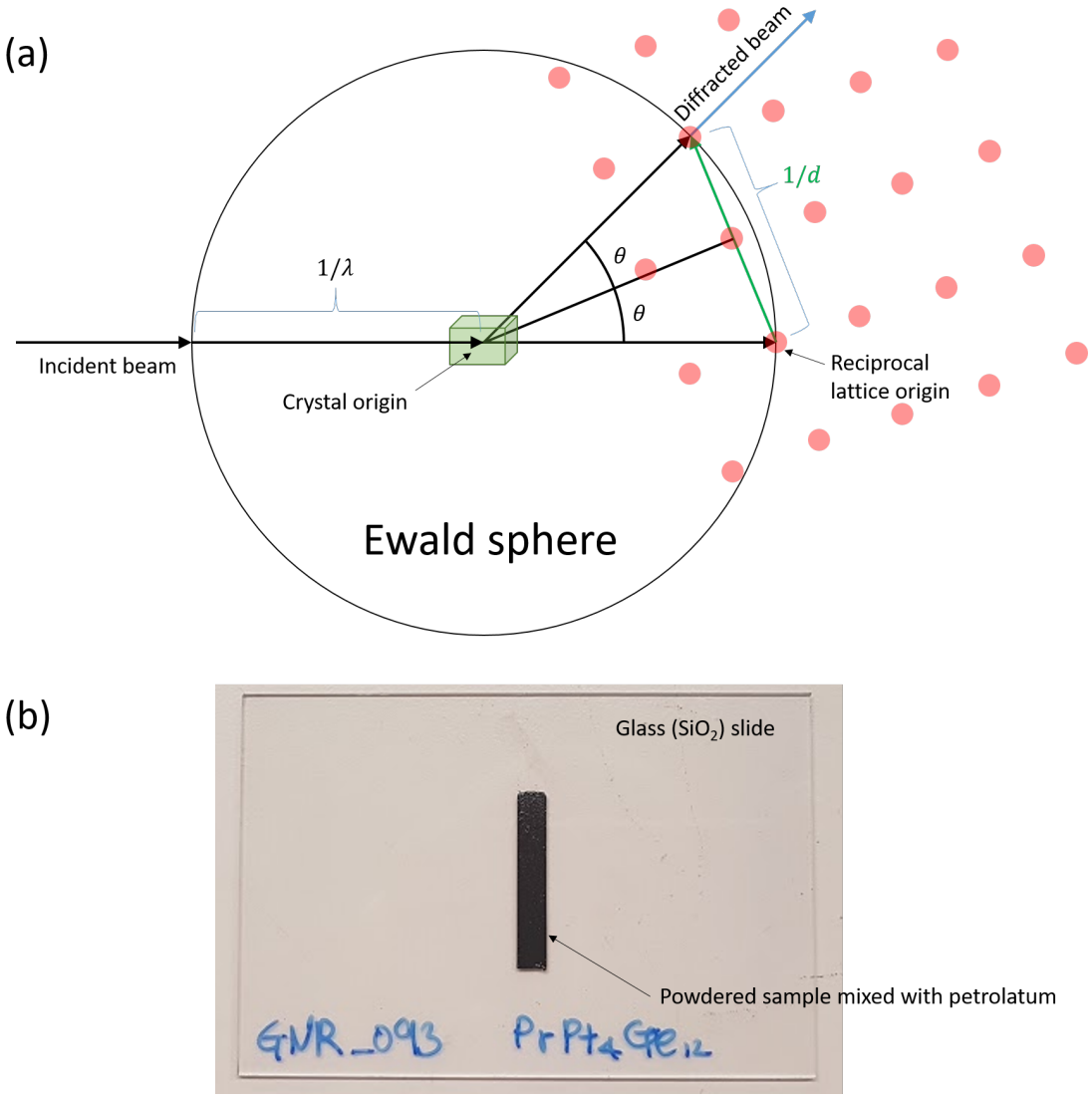


Figure II.3: (a) In the Ewald construction, a sphere with diameter $1/\lambda$ is drawn centered at the crystal. The reciprocal lattice is then drawn on the same scale as the sphere with its origin located $1/\lambda$ from the center of the circle on the opposite side of the incident beam. (b) An example of a skutterudite XRD sample. The mixture of powdered sample and petrolatum is affixed to the glass slide.

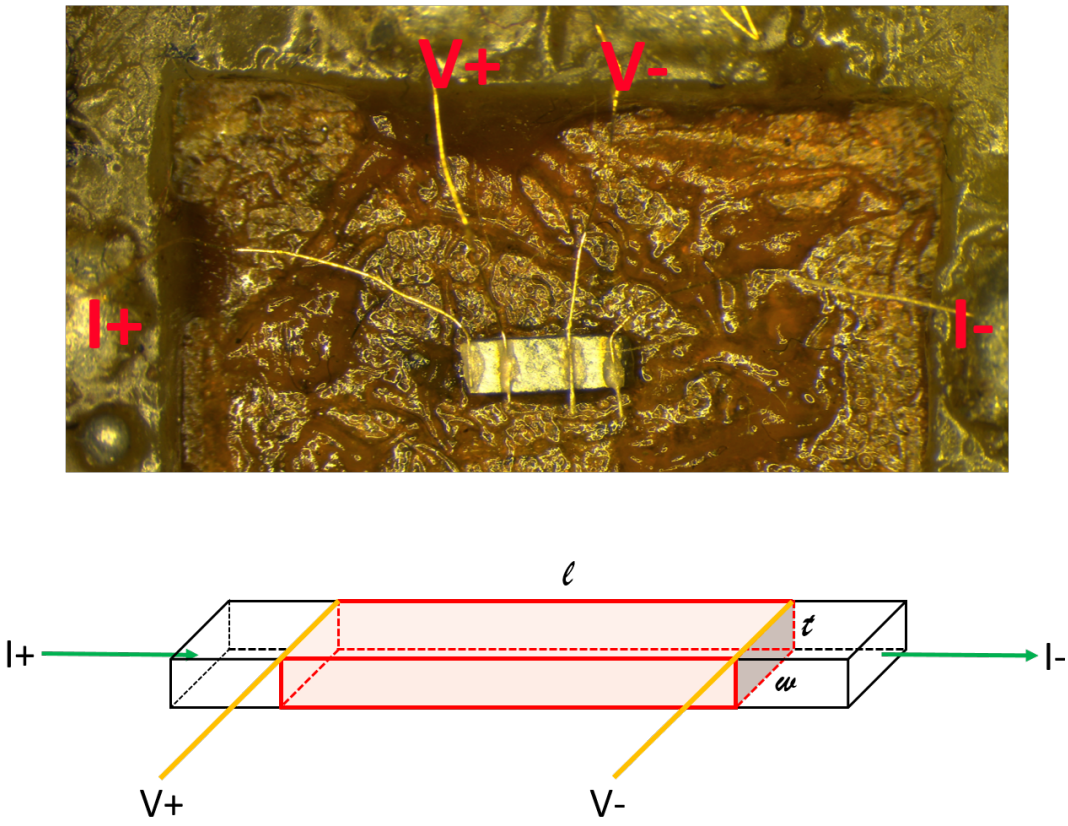


Figure II.4: *Top* : A photo of a resistivity sample with a four-wire configuration in a LR-700 home-built resistivity puck. *Botom* : A schematic of a resistivity bar with relevant dimensions. The geometric factor $\alpha$ is determined by the relation $\alpha = w \cdot t/l$.

is connected to the detection coils to filter out noise and measure temperature-dependent magnetization of samples in very high precision. A schematic of MPMS apparatus is shown in Fig. II.5. The samples were shaped to a rectangular prism, in order to estimate demagnetization factors upon applied magnetic field, especially for superconducting samples. A magnetization sample of $BiS_2$-superconductor is shown in Fig. II.5.

### II.B.4 Specific Heat

The measurements of specific heat were made by using a Quantum Design Physical Properties Measurements System (PPMS) DynaCool, equipped with a 9 Tesla magnet in the temperature range between 1.8 K and 300 K. The sample is shaped to a thin slab within $3 \times 3$ mm$^2$ in size and 1 to 10 mg in mass, due to the design of the sample holder (PPMS Heat Capacity puck), which has the sample platform suspended by eight platinum wires to thermally isolate the sample from the puck. The surface of the sample, which contacts to the sample platform, is well polished and also Apiezon N-grease is applied to the sample-platform interface, in order to promote good thermal contact. A schematic and an actual image of the PPMS heat capacity option are shown in Fig. II.6 (a) and (c), respectively. A standard thermal relaxation technique was employed to fit relaxation curve to an exponential decay after applying a short heat pulse to the sample. The time-dependent heat pulse and temperature change in the sample are illustrated in Fig. II.6 (b). Each measurement, the specific heat of the N-grease, called the Addenda, is measured separately and subtracted from the total specific heat data to obtain the specific heat of the sample only.

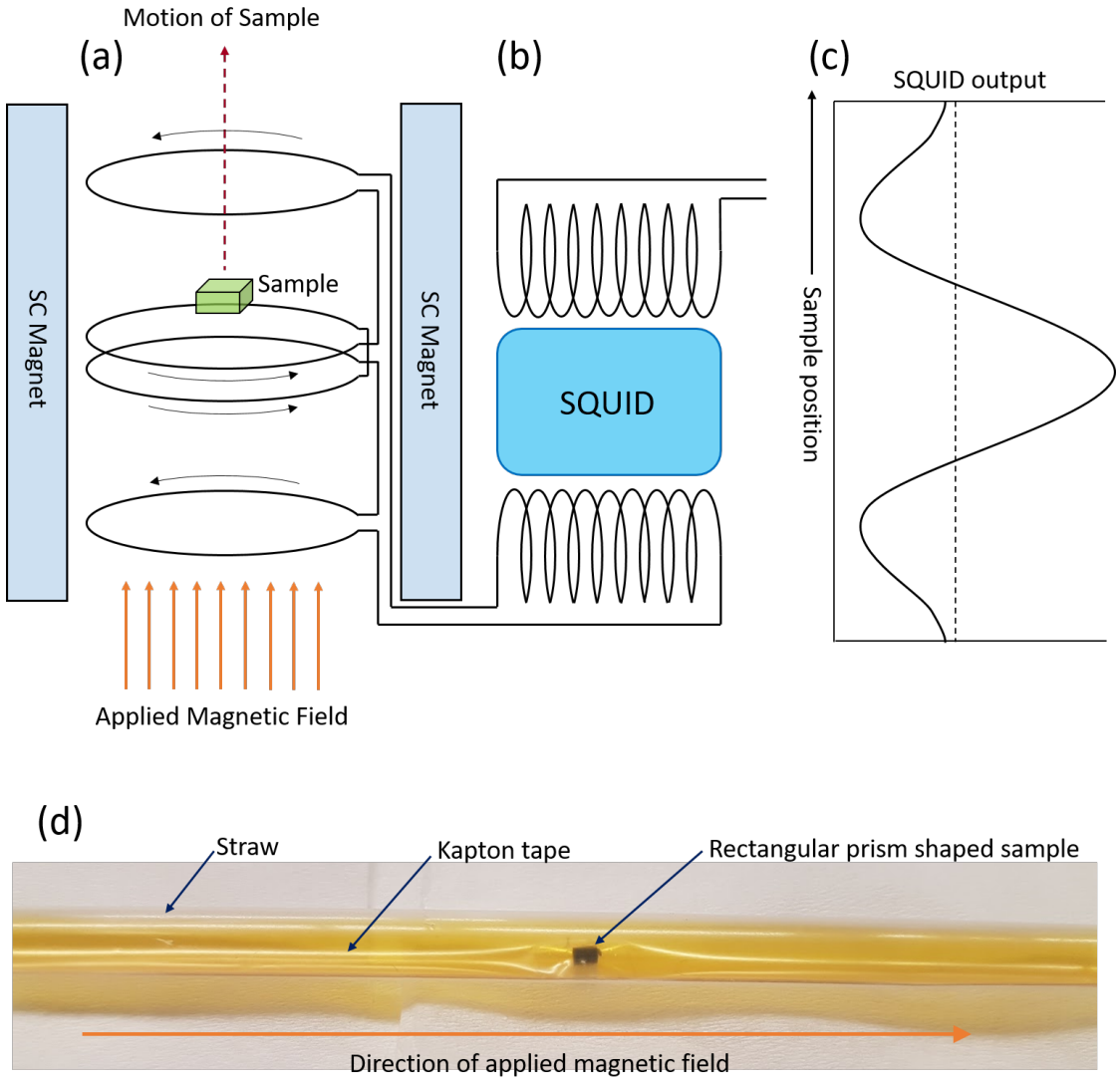


Figure II.5: A schematic of a MPMS apparatus. (a) A sample travels vertically through the detection coils in an applied magnetic field. (b) A SQUID transforms periodic signals of voltage variations of the sample to magnetic moments of the sample in a high precision. (c) Calibrated output from SQUID, as a function of sample position. (d) An example of $BiS_2$ magnetization sample. The rectangular prism shaped sample is fixed by kapton tape in a straw.

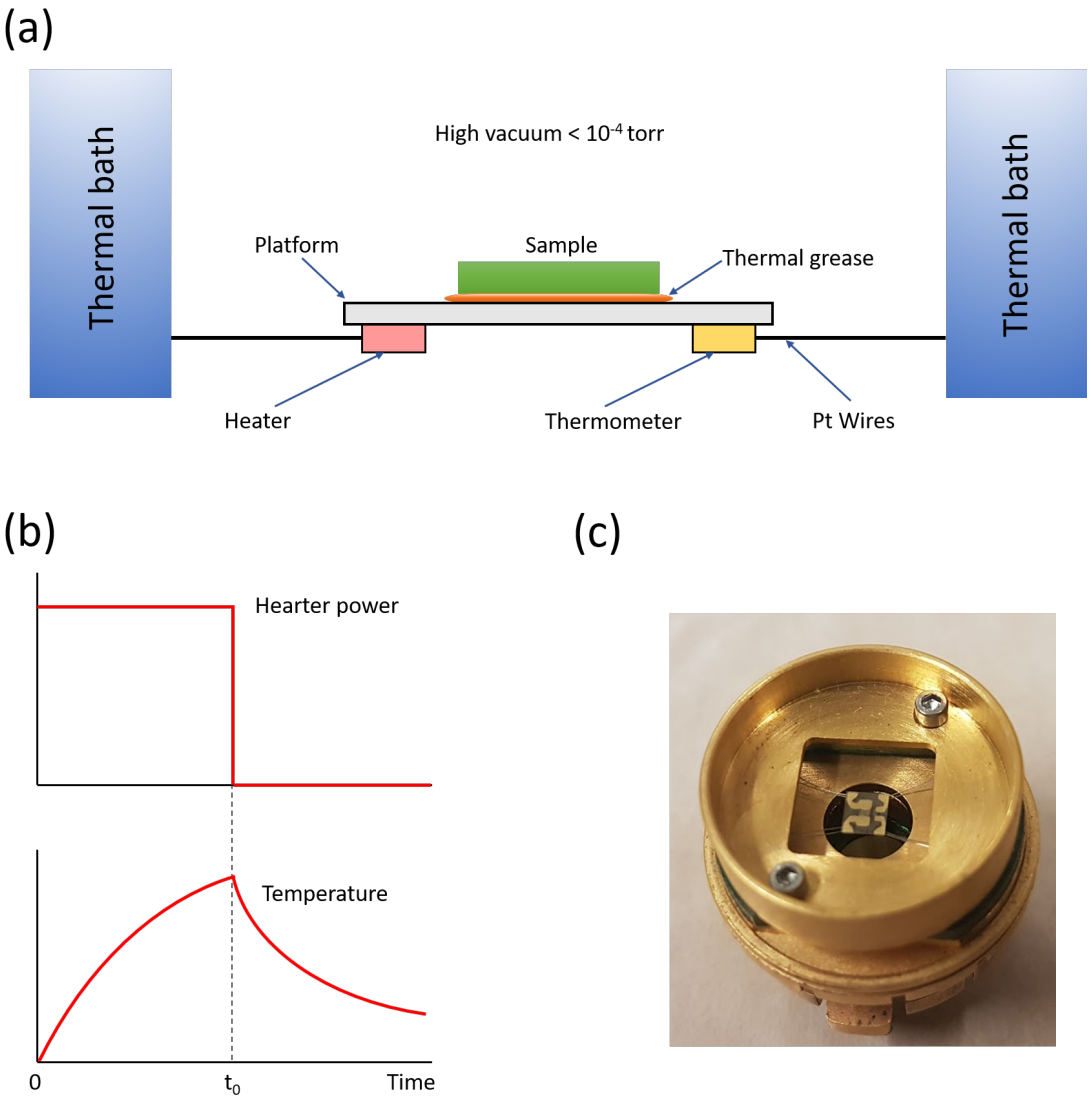


Figure II.6: (a) A schematic of a PPMS heat capacity option. (b) An illustration of heat capacity measurement approach. (c) The PPMS heat capacity puck.

## Bibliography

[1] A. C. Larson and R. B. V. Dreele, Los Alamos National Laboratory Report, 1994 (unpublished).

[2] B. Toby, J. Appl. Crystallogr. **34**, 210 (2001).

[3] H. M. Rietveld, J. Appl. Crystallogr. **2**, 65 (1969).

# Chapter III

# Effect of yttrium substitution on the superconducting properties of the system $La_{1-x}Y_xO_{0.5}F_{0.5}BiS_2$

## III.A Introduction

Superconductivity was discovered in the layered compound $Bi_4O_4S_3$ with critical temperature $T_c = 8.6$ K [1, 2]. Shortly thereafter, superconductivity was reported in fluorine-doped $LnO_{1-x}F_xBiS_2$ ($Ln$ = La, Ce, Pr, Nd, Yb) compounds, with a maximum $T_c = 10.6$ K [3–12]. A layered structure is also observed for these materials, composed of superconducting $BiS_2$ and blocking oxide layers. Subsequent studies demonstrated that superconductivity is induced in general by electron doping in the blocking layers, as with the systems $LnO_{1-x}F_xBiS_2$ ($Ln$ = La, Ce, Pr, Nd, Yb) and $La_{1-x}M_xOBiS_2$ ($M$ = Ti, Zr, Hf, Th) [13], or doping in the isocharge block $[Ln_2O_2]^{2-}$ with a $[Sr_2F_2]^{2-}$ layer [14, 15]. The parent compounds, $AOBiS_2$ ($A$ = La, Ce, Th) [6, 13] and $SrFBiS_2$ [14–16], are bad metals and show semiconducting-like behavior; however, theoretical studies employing the tight-binding model and density functional calculations predicted that electron doping

in the $BiS_2$ system increases the density of states at the Fermi level [17, 18], making electron doping a crucial tuning parameter for superconductivity. The pairing mechanism in both $Bi_4O_4S_3$ and $LaO_{0.5}F_{0.5}BiS_2$ has also been investigated; recent studies of the temperature dependence of the penetration depth by the tunnel diode oscillator technique revealed evidence for fully gapped, strongly-coupled s-wave superconductivity in the $Bi_4O_4S_3$ compound [19], and an s-wave character for $LaO_{0.5}F_{0.5}BiS_2$ was indicated in muon-spin spectroscopy measurements [20]. It has been suggested that superconductivity emerges in the vicinity of a charge-density wave (CDW) and semiconducting-like behavior [6, 21]. Moreover, neutron scattering measurements on the $LaO_{1-x}F_xBiS_2$ system show intrinsic structural instabilities in the superconducting phases [22]. As a consequence, studies focused on applied pressure as a tuning parameter in $BiS_2$ compounds have been conducted recently. It has been reported that the $LnO_{0.5}F_{0.5}BiS_2$ ($Ln$ = La, Ce, Pr, Nd) compounds show marked $T_c$ enhancements [23–27] when subjected to applied pressure. A study of $LaO_{0.5}F_{0.5}BiS_2$ with various lattice parameters has shown that reducing the lattice parameters should have an effect on $T_c$ [28]. To further investigate the relationships between pressure, lattice parameters, and superconductivity, chemical substitution of Y for La is a logical way to tune the properties of $LaO_{0.5}F_{0.5}BiS_2$. Like La, Y has no magnetic moment and a trivalent electronic configuration, and chemical pressure can be introduced by partial substitution of La by smaller Y ions. The effect of Y substitution has been studied for a number of superconducting systems, with suppression of superconductivity observed in the systems $(La_{1-x}Y_x)_{1.85}Sr_{0.15}CuO_4$ and $(La_{1-x}Y_x)NiC_2$ [29, 30], and enhancement of superconductivity observed in $(La_{1-x}Y_x)Co_2B_2$, $La_{1-x}Y_xFeAsO_{1-\delta}$, and F-doped $La_{1-y}Y_yFeAsO$ [31–33]. The latter system shows a remarkable enhancement of $T_c$ from 24 K to 40 K. The effect of Y substitution on the $BiS_2$ systems has not been explored yet. In this work, we present a systematic study in which we have

substituted Y ions into the La-site in $LaO_{0.5}F_{0.5}BiS_2$. We observe that the critical temperature $T_c$ appears to be correlated with the lattice parameter $c$ and the La-O-La bond angle. The chemical pressure resulting from Y substitution is insufficient to induce the structural phase transition from tetragonal ($P4/nmm$) to monoclinic ($P2_1/m$) crystal structures seen under an applied pressure of 1 GPa in $LaO_{0.5}F_{0.5}BiS_2$ [34].

## III.B Experimental Details

Polycrystalline samples of $La_{1-x}Y_xO_{0.5}F_{0.5}BiS_2$ ($0 \leq x \leq 0.40$) were prepared by a conventional solid state reaction method. High-purity starting materials (purity $\geq 99.9\%$) of La, Y, and S, as well as $LaF_3$, $Bi_2O_3$, and $Bi_2S_3$ were weighed stoichiometrically. They were well-mixed, pressed into pellets, encapsulated in evacuated quartz tubes, and annealed at 800 °C for two days. This process was repeated two additional times to promote homogeneity of the samples. The crystal structure was determined by x-ray powder diffraction (XRD) using a Bruker D8 Discover x-ray diffractometer with Cu-$K_\alpha$ radiation and XRD patterns were analyzed via Rietveld refinement using the GSAS+EXPGUI software package [35, 36]. The temperature dependence of electrical resistivity was measured from 1.1 K to 300 K using a standard four-wire method with a Linear Research LR700 ac resistance bridge and a home-built probe in a liquid $^4$He Dewar. Magnetic susceptibility measurements were performed between 2 K and 10 K with applied magnetic field $H = 5$ Oe using a Quantum Design Magnetic Properties Measurement System (MPMS). Alternating current magnetic susceptibility was measured down to $\sim$ 1.1 K in a liquid $^4$He Dewar using home-built magnetic susceptibility coils. Specific heat measurements were made for 1.8 K $\leq T \leq$ 30 K with a Quantum Design Physical Properties Measurement System (PPMS) DynaCool.

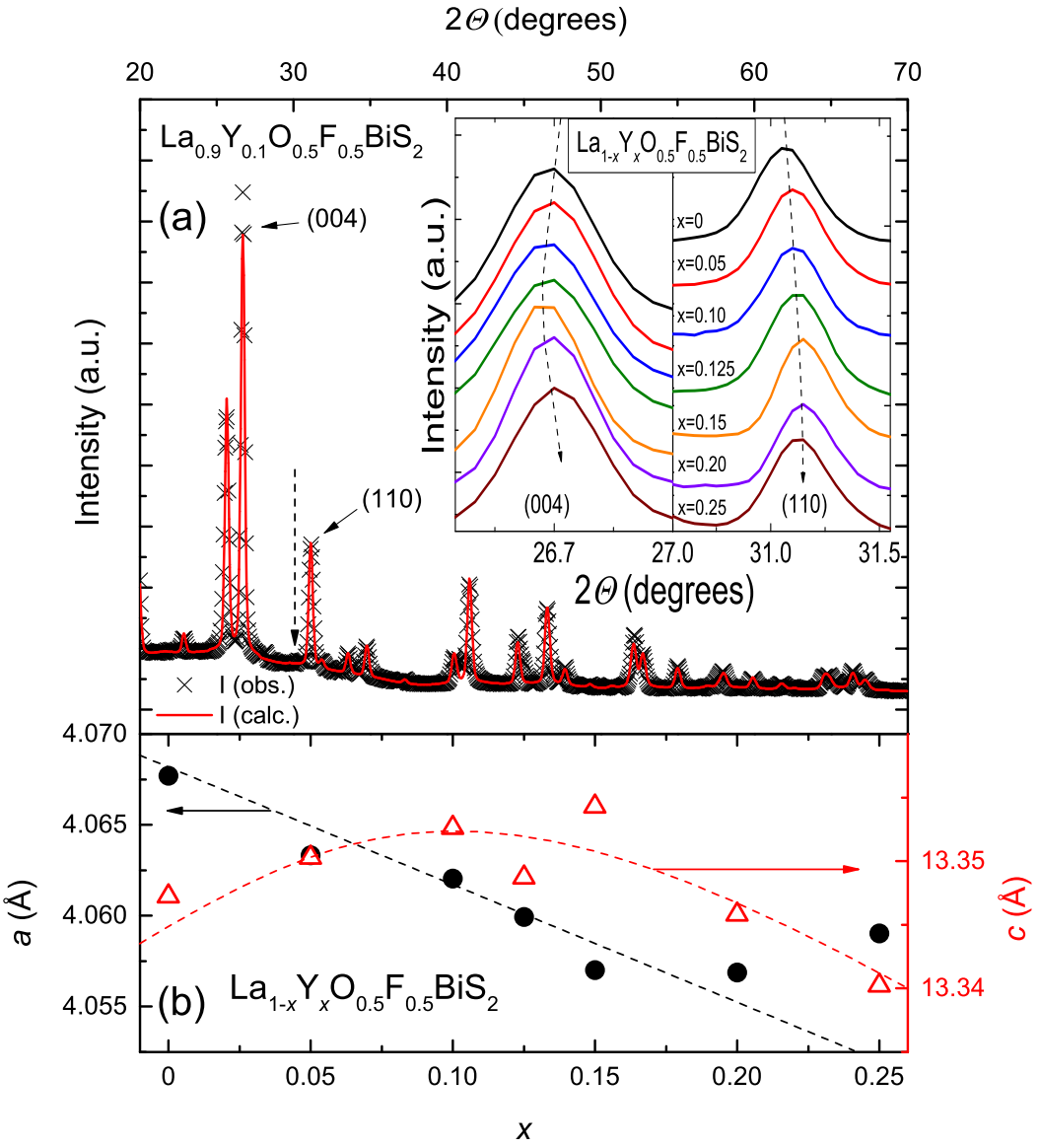


Figure III.1: (a) X-ray diffraction pattern for $La_{0.9}Y_{0.1}O_{0.5}F_{0.5}BiS_2$. The black crosses are data and the red line represents the fit results from Rietveld refinement of the data. The dashed arrow indicates a $La_2O_2S$ and/or $Y_2O_2S$ impurity. The systematic behavior of the (004) and (110) diffraction peaks is shown in the inset of the graph. (b) Lattice parameters $a$ and $c$ versus nominal yttrium concentration $x$.

## III.C Results

### III.C.1 X-ray diffraction

Figure III.1 shows XRD data for $La_{1-x}Y_xO_{0.5}F_{0.5}BiS_2$ ($0 \leq x \leq 0.25$) samples. All XRD patterns are well indexed by the tetragonal $CeOBiS_2$-type crystal structure with space group $P4/nmm$. Figure III.1 (a) displays the XRD pattern and the result of Rietveld refinement of the data for the $La_{0.9}Y_{0.1}O_{0.5}F_{0.5}BiS_2$ sample. The dashed arrow indicates the presence of $La_2O_2S$ and/or $Y_2O_2S$ impurity phases, the amount of which increases gradually with increasing $x$. This implies a possible minor discrepancy between nominal and actual yttrium concentrations. The samples with $x \leq 0.25$ contain the same impurity phase constituting 1%-8% of the sample by mass and less than 1% of possible Y and $Bi/Bi_2S_3$ impurity phases by mass, as estimated by Rietveld refinements. The systematic behavior of the (004) and (110) diffraction peaks is shown in the inset of Fig. III.1 (a) and the $a$ and $c$ lattice parameters are plotted as a function of nominal Y concentration in Fig. III.1 (b).

To estimate the true Y concentration in our samples, we calculated the expected unit cell volume of $YO_{0.5}F_{0.5}BiS_2$ (which has thus far not been successfully synthesized) and then compared the measured volumes of our $La_{1-x}Y_xO_{0.5}F_{0.5}BiS_2$ samples against the expected behavior from Vegard's law. To estimate the unit cell volume of $YO_{0.5}F_{0.5}BiS_2$, we first calculated the total volume of the ions residing in a single unit cell of $LaO_{0.5}F_{0.5}BiS_2$ using ionic radii values of the elements from Ref. [37]. We then computed a scale factor by comparing the total volume of the ions with the measured unit cell volume of $LaO_{0.5}F_{0.5}BiS_2$. Assuming a similar scale factor is appropriate for the compounds containing other rare-earth ions, we made similar calculations to estimate their unit cell volumes. The trend of these estimated unit cell volumes for rare-earth ions is displayed in Fig. III.2 (a) along

with measured values for some compounds. Our estimate seems to work particularly well for $CeO_{0.5}F_{0.5}BiS_2$, but we note that there is a significant spread in experimentally-measured unit cell volumes for the other compounds and that our estimates are reasonable given such uncertainty. Invoking Vegard's law, we plot a line between the measured unit cell volume for $LaO_{0.5}F_{0.5}BiS_2$ and our estimated value for the volume of $YO_{0.5}F_{0.5}BiS_2$, and compare this line with the measured volumes of our $La_{1-x}Y_xO_{0.5}F_{0.5}BiS_2$ samples up to $x = 0.40$ in Fig. III.2 (b). The agreement between measured and estimated volumes is good up to $x = 0.20$ and this simple procedure helps to get an idea of the uncertainty for the Y concentrations; the difference between nominal and estimated concentrations can be as large as 3% for the first batch of the $x = 0.10$ sample, for instance.

For $x \geq 0.25$, the unit cell volumes $V$ are concentration-independent, as seen in Fig. III.2 (b) and the XRD patterns contain impurity phases of Y, $La_2O_2S/Y_2O_2S$, and $Bi/Bi_2S_3$, suggesting that the sample with $x = 0.25$ is near or even beyond the solubility limit. Therefore, we can conservatively conclude that Y is incorporated into the La site up to $x = 0.20$ in this system. Since the system forms with a tetragonal crystal structure ($P4/nmm$), the lattice parameter $a$ has a more dominant effect than the lattice parameter $c$ on the unit cell volume $V$, with both $a$ and $V$ decreasing with increasing $x$. Also, the ionic radius of Y is less than that of La, suggesting that chemical pressure is induced in $La_{1-x}Y_xO_{0.5}F_{0.5}BiS_2$ up to $x = 0.20$.

### III.C.2 Electrical Resistivity

Electrical resistivity $\rho(T)$ data are plotted in Fig. III.3. For all samples in their normal states, electrical resistivity exhibits semiconducting-like behavior and clear drops at the superconducting transition temperature $T_c$. We determined $T_c$ by measuring the temperatures where the electrical resistivity falls to 50% of

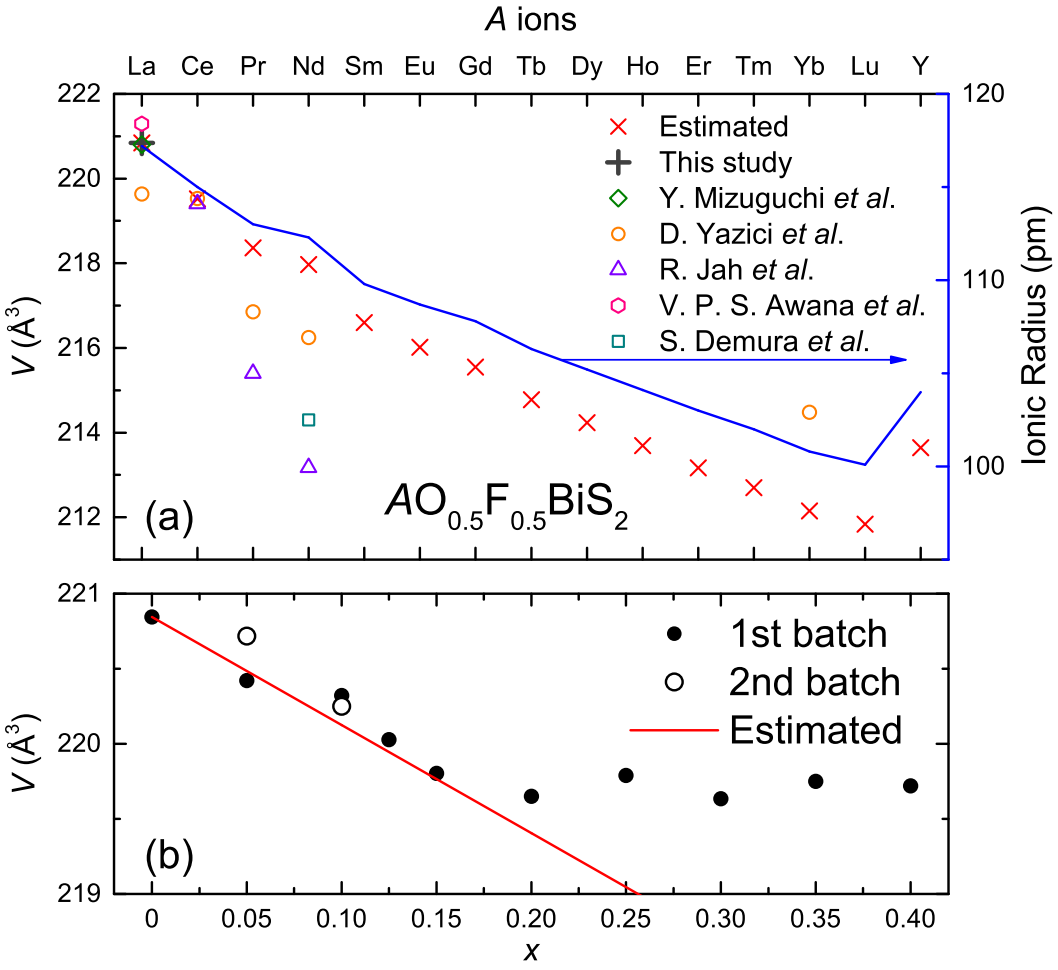


Figure III.2: (a) Estimated volumes and ionic radii versus lanthanide and Y ions are shown for $AO_{0.5}F_{0.5}BiS_2$. The blue line is the trend of ionic radii for lanthanide and Y ions. Red crosses are estimated volumes and other symbols are reported volumes for $LnO_{0.5}F_{0.5}BiS_2$ ($Ln$ = La, Ce, Pr, Nd, Yb). The estimated volume of $YO_{0.5}F_{0.5}BiS_2$ is at the right corner. (b) Black circles and red line are observed and estimated unit cell volumes $V$ versus $x$, respectively. Unfilled circles correspond to a second batch of samples prepared for selected Y concentrations.

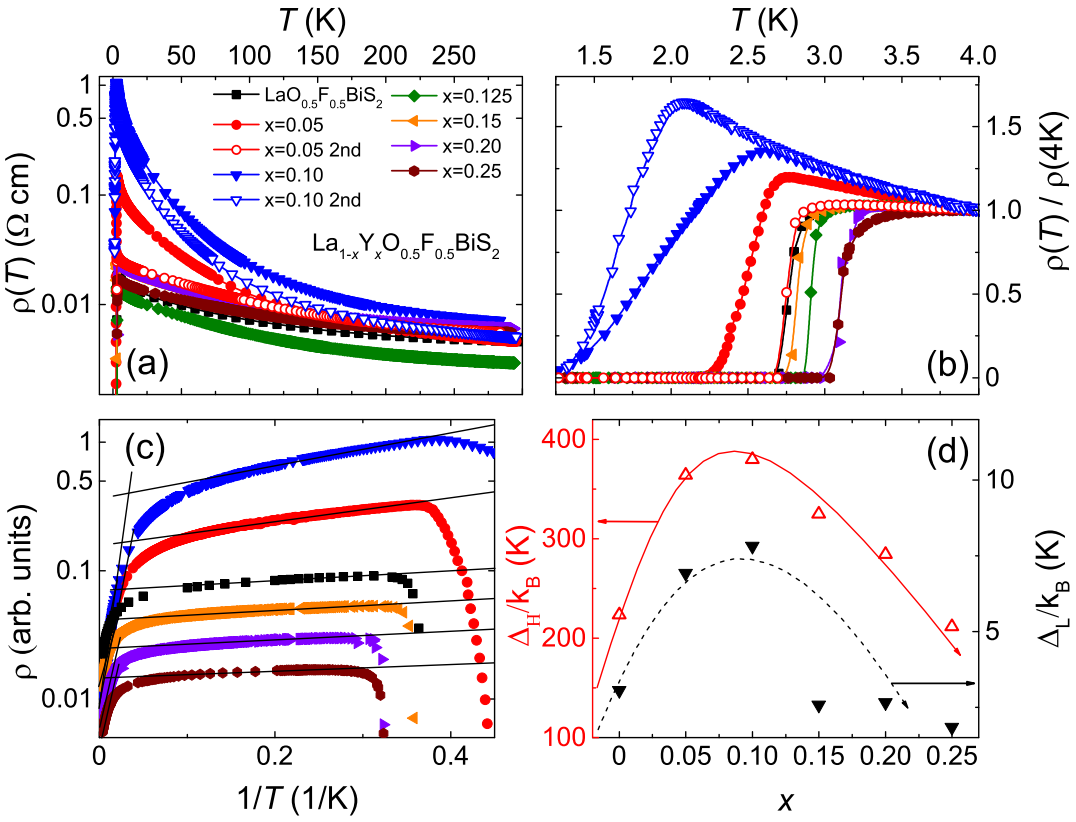


Figure III.3: (a) A semilogarithmic plot of electrical resistivity $\rho$ versus temperature $T$. (b) $\rho$, normalized to its value at 4 K, versus temperature $T$. (c) ln $\rho$ versus $1/T$ for selected samples with $x = 0$, 0.05, 0.10, 0.15, 0.20, and 0.25. The solid lines indicate simple activation-type temperature dependencies from Eq. (III.1). The data are vertically offset for visual clarity. (d) Energy gaps $\Delta_H/k_B$ and $\Delta_L/k_B$ calculated at high and low temperatures respectively, versus nominal yttrium concentration $x$.

its normal-state value, and the broadness of the transitions was characterized by identifying the temperatures where the electrical resistivity decreases to 90% and 10% of the normal-state value. We observe two different types of behavior: for $x \leq 0.10$, $\rho$ increases rapidly with decreasing temperature in its normal-state and a broad superconducting transition is observed, while a slower increase of $\rho$ with decreasing temperature accompanying a sharp superconducting transition is seen for $x > 0.10$. Such behavior is emphasized by plotting $\rho(T)$, normalized by its value at 4 K, versus temperature $T$ in Fig. III.3 (b). To confirm the reproducibility of these different types of behavior, we have synthesized and characterized several additional samples for each Y concentration, especially for $x = 0.05$ and 0.10. Since we observed the same behavior for different samples within all batches, shown in Figs. III.2(b), III.3(a) and (b), and III.6(b), we only present representative data for each concentration in this study. To estimate the energy gaps, we adopted the simple activation-type relation [23],

$$\rho(T) = \rho_0 e^{\Delta/2k_BT}, \tag{III.1}$$

where $\rho_0$ is a constant and $\Delta$ is the energy gap. As shown in Fig. III.3 (c), we fit Eq. III.1 to data for selected samples in two regions, 200 - 300 K and $T_c$ - 20 K, to obtain a high-temperature energy gap $\Delta_H/k_B$ and a low-temperature energy gap $\Delta_L/k_B$, respectively . Both energy gaps are found to first increase with $x$ up to $x = 0.10$ and then decrease with higher concentration, as illustrated in Fig. III.3 (d). This behavior exhibits the same trend as that of the lattice parameter $c$. The behavior of the electrical resistivity up to $x = 0.10$ is different from that observed under applied external pressure on $BiS_2$-based superconducting compounds [23–27, 34], in which semiconducting-like behavior is suppressed with increasing pressure and a metallic state is induced. On the other hand, we note

Table III.1: Impurity phases $La_2O_2S$ and/or $Y_2O_2S$ by mass and superconducting volume fraction at 2 K along with $T_c$ from $\rho$ data for each concentration.

| $x$ | $T_c$ (K) | Imp. (%) | $V$ frac. (%) | Ref. |
|---|---|---|---|---|
| Parent | 2.7 | - | $\sim 6$ | [11] |
| | 3.0 | - | $\sim 13$ | [3] |
| | 3.1 | - | $\sim 60$ | [7] |
| | 2.8 | $< 1$ | - | [This study] |
| 0.05 | 2.5 | $\sim 1$ | $\ll 1$ | |
| 0.10 | 1.8 | $\sim 2$ | $\ll 1$ | |
| 0.125 | 2.9 | $\sim 2$ | $\sim 11$ | [This study] |
| 0.15 | 2.8 | $\sim 3$ | $\sim 3$ | |
| 0.20 | 3.1 | $\sim 4$ | $\sim 4$ | |
| 0.25 | 3.1 | $\sim 8$ | $\sim 8$ | |

that there is currently no data for applied pressures less than 0.3 GPa, which is larger than the chemical pressure in the $x = 0.10$ compound (as will be discussed later). The semiconducting-like behavior is gradually suppressed for $x \geq 0.10$, which is similar to the results reported in pressure studies [26, 27].

### III.C.3 Magnetic Susceptibility

In order to characterize the observed superconductivity in the $La_{1-x}Y_xO_{0.5}F_{0.5}BiS_2$ system, temperature-dependent dc magnetic susceptibility measurements were performed under a 5 Oe magnetic field with both zero-field-cooled (ZFC) and field-cooled (FC) methods, and the results are displayed in Fig. III.4 (a). We performed measurements on selected samples with $x = 0.15$, 0.20, and 0.25 which have superconducting transition temperatures $T_c$ in the accessible temperature range of the MPMS. Clear diamagnetic signals were observed for each of these samples. The $T_c$ values, determined by the temperatures at the onset of the diamagnetic signal, are indicated by the solid arrows in Fig. III.4 (a) and are in good agreement with those estimated from the electrical resistivity data. Alternating current magnetic susceptibility measurements for the samples

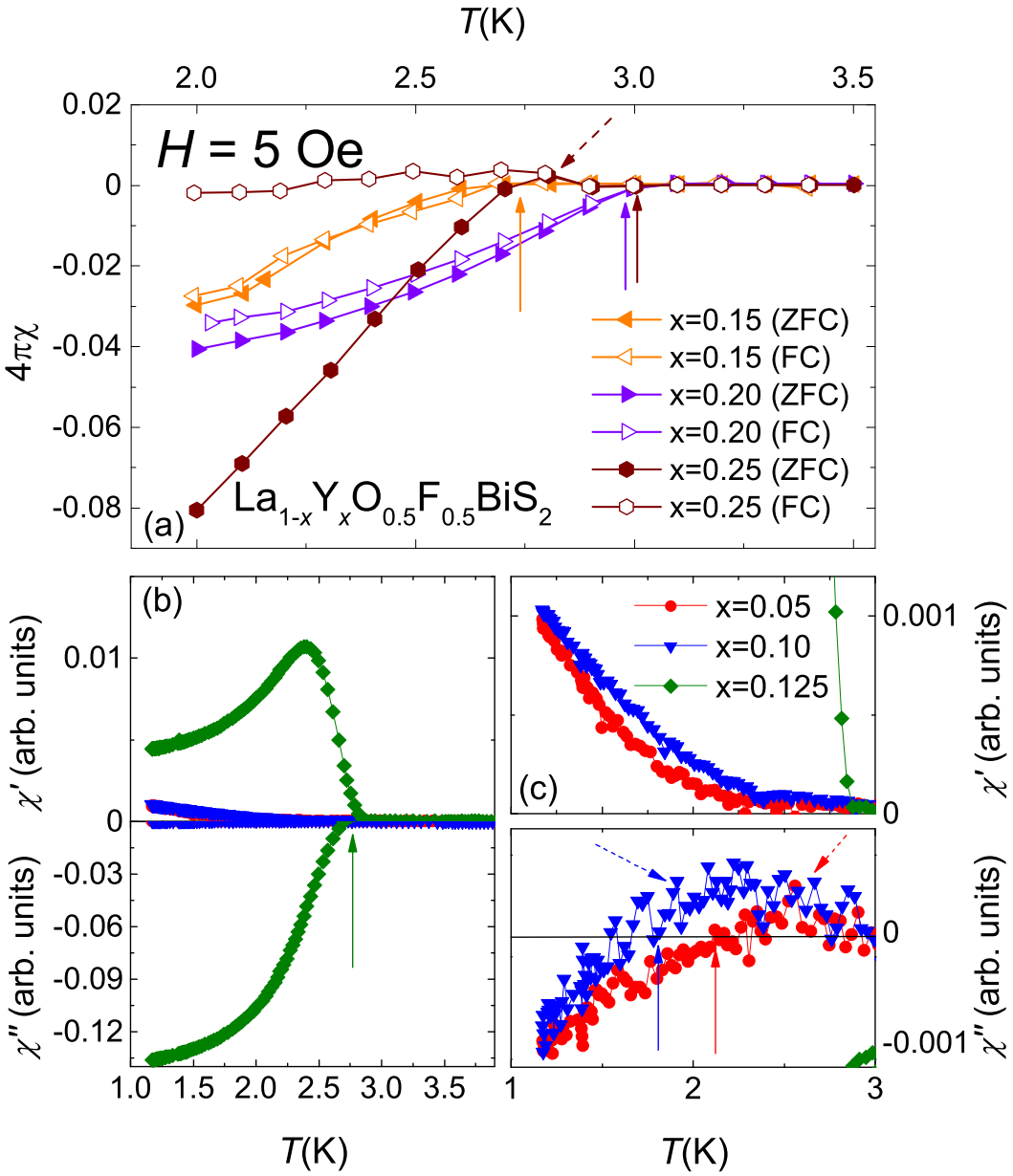


Figure III.4: (a) Magnetic susceptibility $\chi_{dc}$ versus temperature $T$ for $La_{1-x}Y_xO_{0.5}F_{0.5}BiS_2$ ($x = 0.15$, 0.20, and 0.25), measured in field cooled and zero-field cooled conditions. The solid arrows denote the superconducting critical temperature $T_c$ and the dashed arrow emphasizes the presence of a small upturn. (b) and (c) Alternating current magnetic susceptibility $\chi_{ac}$ versus temperature $T$ for $x = 0.05$, 0.10, and 0.125. The solid and dashed arrows have the same meaning as in panel (a).

with $x = 0.05$, 0.10, and 0.125 are shown in Figs. III.4 (b) and (c). A clear signature of superconductivity was observed for $x = 0.125$ and the onset of a SC signal was observed for the $x = 0.05$, 0.10 samples. Though the transitions are not complete, we estimated superconducting shielding fractions of $\sim 13\%$ at 1.1 K for the $x = 0.125$ sample and $\sim 3\%$, $\sim 4\%$, and $\sim 8\%$ at 2 K for the $x = 0.15$, 0.20, and 0.25 samples, respectively. The weak signals for $x = 0.05$, 0.10 followed by increasing shielding fractions for $x \geq 0.125$ seem to correlate with the width of the transitions and the variation of the $T_c$ values observed in electrical resistivity measurements. These shielding fractions are similar to reported values of $\sim 13\%$ and $\sim 6\%$ [3, 11], but smaller than that of the highest value of $\sim 60\%$ [7]. The transition temperatures $T_c$ from $\rho$, the amount of $La_2O_2S$ and/or $Y_2O_2S$ impurity phases by mass, and superconducting volume fractions at 2 K are summarized in Table III.1. These results imply that the volume fractions do not seem to correlate with Y concentrations or the amount of impurity phases; volume fractions more likely correlate with the transition temperatures and the broadness of transitions. The samples with $x = 0.05$, 0.10, and 0.25 exhibit a weak upturn indicated by dashed arrows in dc and ac susceptibility data in Fig. III.4. This behavior is probably due to a small amount of paramagnetic impurities, as observed in other studies [7–10, 13].

### III.C.4 Specific Heat

To further investigate the superconducting properties of this system, measurements of the specific heat, $C$, were performed for the $x = 0.05$ and 0.25 samples in the temperature range from 1.8 K to 30 K. The results of these measurements are displayed in Fig. III.5. Although the specific heat jump for the $x = 0.05$ sample is incomplete, possibly due to its low $T_c$, we observed a broad upturn which is consistent with the $T_c$ values obtained from $\rho$ (2.5 K) and $\chi_{ac}$ (2.2 K), suggesting

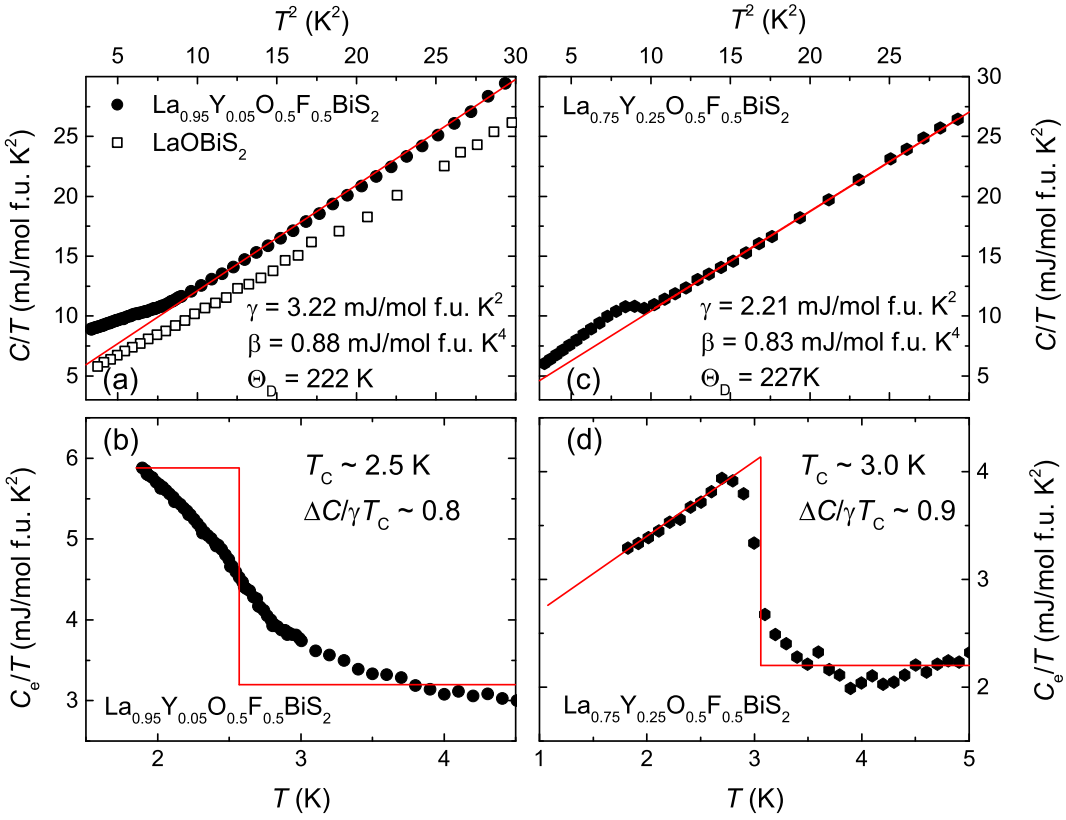


Figure III.5: (a) and (c) Specific heat divided by temperature $C/T$ versus temperature $T$ for $LaOBiS_2$, $La_{0.95}Y_{0.05}O_{0.5}F_{0.5}BiS_2$, and $La_{0.75}Y_{0.25}O_{0.5}F_{0.5}BiS_2$. The red lines represent the best fits of the equation $C(T)/T = \gamma + \beta T^2$ to the data which yield $\gamma = 3.22$ mJ/mol f.u.K$^2$ and $\Theta_D = 222$ K for $x = 0.05$ and $\gamma = 2.21$ mJ/mol f.u.K$^2$ and $\Theta_D = 227$ K for $x = 0.25$. (b) and (d) Plots of the electronic contribution to the specific heat divided by $T$, $C_e/T$, versus temperature $T$. Idealized entropy conserving constructions result in an estimate of $\Delta C/\gamma T_c = 0.8$ for $x = 0.05$ if we use $T_c = 2.5$ K from electrical resistivity measurements (see text) and $T_c = 3.0$ K and $\Delta C/\gamma T_c = 0.9$ for $x = 0.25$.

that this feature is assocaited with superconductivity. For the $x = 0.25$ sample, a clear specific heat jump is observed at $T_c \simeq 3.0$ K, in good agreement with the $T_c$ values from $\rho$ (3.1 K) and $\chi_{dc}$ (3.0 K). The appearance of a jump in $C/T$ at $T_c$ is strong evidence that the superconductivity for $x = 0.05$ and 0.25 is a bulk phenomenon. The specific heat at low temperature can be written,

$$C(T) = \gamma T + \beta T^3, \tag{III.2}$$

where the terms $\gamma T$ and $\beta T^3$ account for the electronic and phonon contributions, respectively. The data were fitted to this expression, yielding the electronic coefficient $\gamma = 3.22$ mJ/mol f.u.K$^2$ and the lattice coefficient $\beta = 0.88$ mJ/mol f.u.K$^4$ for the $x = 0.05$ sample and $\gamma = 2.21$ mJ/mol f.u.K$^2$ and $\beta = 0.83$ mJ/mol f.u.K$^4$ for the $x = 0.25$ sample. The best fits, shown in Figs. III.5 (a) and (c), yield the fitting parameters listed in the figures. To obtain the ratios of the specific heat jump to $\gamma T_c$, the lattice contributions were subtracted revealing the upturn and specific heat jump in Fig. III.5 (b) and (d), respectively. Since the jump was incomplete for the $x = 0.05$ sample, a rough estimate of the ratio $\Delta C/\gamma T \sim 0.8$ was extracted from the size of the upturn and assuming $T_c \sim 2.5(1)$ K, as illustrated in Fig. III.5 (b). This value is comparable to the value of 0.9 for the $x = 0.25$ sample, and both of these are smaller than the value of 1.43 predicted by the weak-coupling Bardeen-Cooper-Schrieffer (BCS) theory of superconductivity; on the other hand, our values of $\gamma$, $\Theta_D$, and $\Delta C/\gamma T$ are similar to $\gamma = 2.53$ mJ/mol f.u.K$^2$, $\Theta_D = 221$ K, and $\Delta C/\gamma T = 0.94$ reported for $LaO_{0.5}F_{0.5}BiS_2$ [7].

It is noteworthy that the electronic specific heat behaves so differently from the predictions of the BCS theory. According to the BCS weak-coupling limit, the electronic specific heat below $T_c$ decreases exponentially with decreasing temperature and almost reaches zero near $T_c/5$ [38]. In contrast to the BCS limit, our data

for $x = 0.25$ are still larger than the normal state value at $T_c/2$, as seen in Fig. III.5 (d). Similar behavior of specific heat was observed in previous studies [13, 14]. Attempts to fit the specific heat data for $x = 0.25$ to a simple BCS expression for the low-temperature electronic specific heat, $C_e/\gamma T_c = 1.34(\Delta(0)/T)^{3/2}e^{-\Delta(0)/T}$ [39], where the exponential drop is determined by the zero-temperature energy gap, $\Delta(0)$, required the inclusion of additional temperature dependent and constant terms to satisfactorily fit the data (data and fits not shown). It is already known that these samples are not completely homogeneous, and such behavior suggests that part of the sample behaves as a bulk superconductor while the rest (the impurity phase portions of the sample) provide a non-superconducting contribution to $C/T$. The combination of these contributions presumably leads to the distinctly non-BCS temperature dependence we have observed in the behavior of $C_e(T)/T$ below $T_c$. We also note that there is a debate regarding whether or not $BiS_2$-based superconductors actually exhibit conventional BCS superconductivity: weak electron-phonon coupling, a rather large value of $2\Delta/k_BT_c \sim 17$, giant superconducting fluctuations, and an anomalous semiconducting normal state have been considered for these compounds [22, 40, 41]. More investigations will be needed to determine the mechanism and nature of superconductivity in $BiS_2$-based compounds.

## III.D Discussion

We summarize the results from $\rho$, $\chi_{dc}$, $\chi_{ac}$, and $C$ measurements in a phase diagram of transition temperature $T_c$ versus nominal yttrium concentration $x$, as shown in Fig. III.6 (b). $T_c$ decreases from 2.8 K to 1.8 K with increasing $x$ until $x = 0.10$ and is roughly constant with a value of $\sim 3.0$ K for $x \geq 0.125$. $T_c$ was found to decrease slightly in a study of the $LaO_{0.5}F_{0.5}BiS_2$ system under low ap-

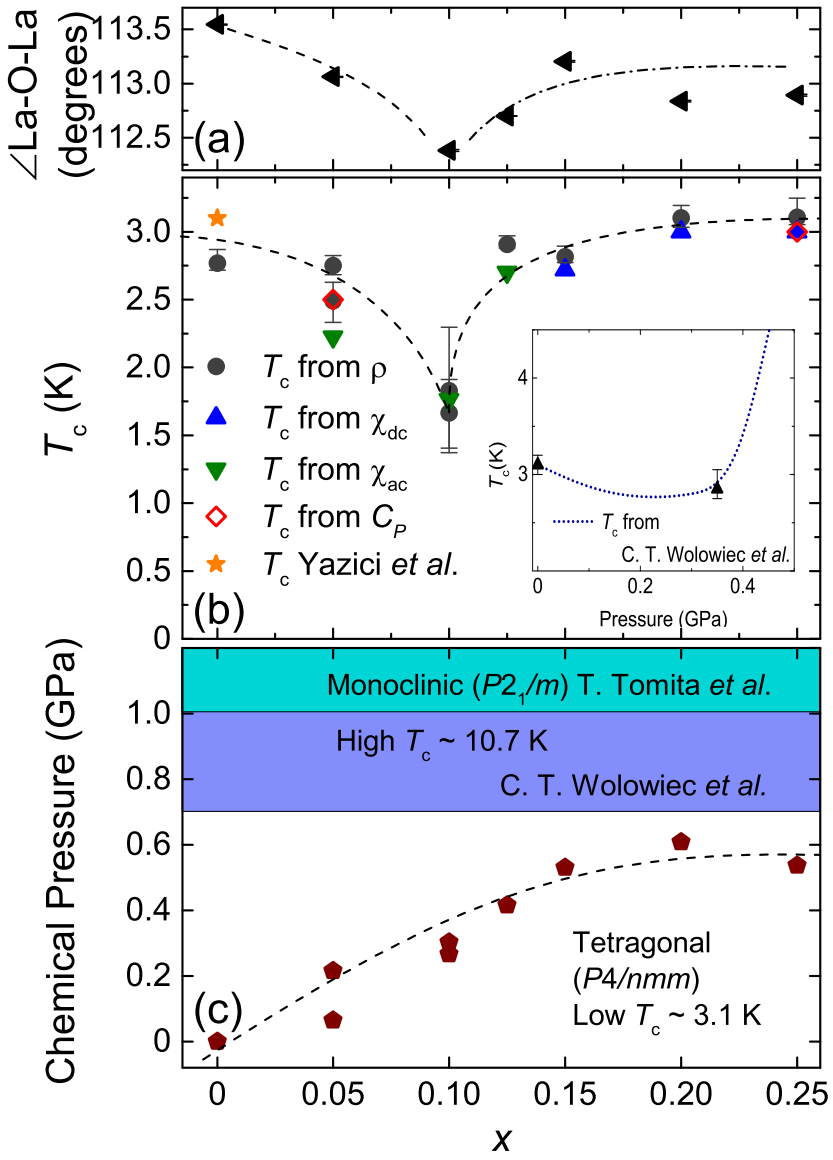


Figure III.6: (a) La/Y-O/F-La/Y bond angle ∠La-O-La versus nominal yttrium concentration $x$. (b) Superconducting transition temperature $T_c$ versus nominal yttrium concentration $x$ for the $La_{1-x}Y_xO_{0.5}F_{0.5}BiS_2$ system. The orange star is the maximum $T_c$ obtained from electrical resistivity measurements of $LaO_{0.5}F_{0.5}BiS_2$ reported in Ref. [7]. The inset shows the behavior of $T_c$ under applied pressure [27]. (c) Chemical pressure versus nominal yttrium concentration. Two regions with low $T_c$ and high $T_c$ (purple and blue regions) are separated by the reported critical pressure value $P_c \sim 0.7$ GPa [23, 26, 34]. The tetragonal (unfilled and purple regions) and monoclinic (blue region) phases are distinguished by the critical pressure $P_T \sim 1$ GPa for the structural phase transition [34].

plied pressures [26, 27], as shown in the inset of Fig. III.6 (b). This behavior of $T_c(P)$ resembles that of $T_c(x)$ in $La_{1-x}Y_xO_{0.5}F_{0.5}BiS_2$. This observation probably indicates that there is a relationship between $T_c$ and crystal structure details. With that possibility in mind, we found that $T_c(x)$ is related to the lattice constant $c$ (see Fig. III.1 (b)) and the La-O-La bond angle (see Fig. III.6 (a)).

Since the unit cell volume $V$ decreases with increasing Y concentration until $x = 0.20$, the variation of $T_c$ could be discussed in the context of chemical pressure. We adopted a value of the isothermal compressibility [34], $-d(V/V_0)/dP = 0.0089$ $GPa^{-1}$ (bulk modulus is 112 GPa), where $V$ and $V_0$ are the unit cell volumes with and without Y, respectively. A graph of chemical pressure versus the nominal Y concentration $x$ is plotted in Fig. III.6 (c) and the high $T_c$ transition pressure $P_c \sim 0.7$ GPa [23, 26] and structural phase transition pressure $P_T \sim 1$ GPa [34] are illustrated as purple and blue regions, respectively. Since $LaO_{0.5}F_{0.5}BiS_2$ with the tetragonal crystal structure ($P4/nmm$) is stable up to $\sim 0.8$ GPa and then experiences a complete structural phase transition above $\sim 1.5$ GPa, as discussed in previous studies of Tomita *et al.* and Mizuguchi *et al.* [3, 34], the monoclinic phase is presumably responsible for the high-$T_c$ superconducting phase. Our results show that chemical pressure increases with Y concentrations $0 \leq x \leq 0.20$ and saturates at a value of $\sim 0.6$ GPa at the solubility limit. In Fig. III.6 (c), it is clear that the induced chemical pressure is insufficient to induce the high-$T_c$ or the monoclinic phase. If the chemical pressure could be further increased, we expect that the high-$T_c$ and monoclinic phases would be induced for $x \geq 0.20$. This is a simple explanation for why this system did not exhibit an enhancement of superconductivity.

Chemical pressure alone is unable to account for the suppression of superconductivity for $x \leq 0.10$. The lattice parameter $c$ shows different behavior from the unit cell volume $V$. It increases slowly with increasing $x$ to $x = 0.10$ and then

decreases for $x \geq 0.15$ (see Fig. III.1 (b)), in contrast to the monotonic increase of chemical pressure to $x = 0.20$. One possible scenario is that the La/Y-O/F-La/Y ($\angle$La-O-La) bond angle evolves with $x$. As shown in Fig. III.6 (a), we observed a decrease of the bond angle for $0 \leq x \leq 0.10$ and then an increase for $0.125 \leq x \leq 0.25$, as obtained in our Rietveld refinements. Under applied pressure, the lattice parameters $a$ and $c$ of $LaO_{0.5}F_{0.5}BiS_2$ decrease continuously until a structural phase transition is induced near 1 GPa [34]. However, chemical pressure is insufficient to induce the structural phase transition. The suppression and subsequent enhancement of superconductivity with $x$ are probably related to the variation of the lattice parameter $c$, suggesting that the superconducting transition temperature is tuned by $c$ in $BiS_2$-based systems, which is consistent with the conclusions of another recent experimental study [42]. The width of the superconducting transition, energy gap values, and superconducting volume fractions also seem to vary systematically with the lattice parameter $c$.

To the best of our knowledge, studies on $BiS_2$-based compounds still report difficulties synthesizing homogeneous samples; superconducting critical temperatures for the same systems show perceptible discrepancies between studies [3, 4, 6–10]. Also, the lattice parameters or volumes of the same compounds vary for different studies, as seen in Fig. III.2(a). Often, the systematic chemical substitution studies of the same systems have different phase diagrams [4, 6, 8, 12, 15, 16]. Sometimes $T_c$ does not change and seems to be independent of substituent concentrations until a solubility limit emerges, even though both parent compounds are stable and can be synthesized [13].

These discrepancies in the lattice parameters, phase diagrams, and transition temperatures $T_c$ between studies might have one or more possible causes: Fluorine substitution studies for $LnO_{1-x}F_xBiS_2$ ($Ln$ = La, Ce, Nd) [3, 4, 6] showed variations of lattice parameters and $T_c$ for similar nominal fluorine concentrations.

Because of the quantitative inaccuracy of EDX measurements for these materials [41], it is difficult to estimate the exact amount of fluorine in $BiS_2$ compounds. Thus, it is probable that the actual and nominal fluorine ratio could be different, resulting in differences of lattice parameters and $T_c$. On the other hand, recent studies of angle-resolved photoemission spectroscopy (ARPES) and optical spectroscopy [43, 44] on Nd(O,F)$BiS_2$ report rather small electron doping levels of roughly 7 % per Bi site, which is smaller than the high electron doping level, $x \sim 0.5$, expected from theoretical studies. A low electron doping level, intrinsic structural instabilities [22], and possible bismuth deficiencies [45] in $BiS_2$ compounds also complicate our ability to compare results from different studies and combinations of those factors possibly yield such disparities in crystallographic and superconducting properties between studies. In order to advance our understanding of superconductivity in $BiS_2$-based compounds, these materials issues must be addressed.

## III.E Concluding Remarks

We have studied the effect of partial chemical substitution of yttrium for lanthanum in the superconducting $LaO_{0.5}F_{0.5}BiS_2$ system. We synthesized polycrystalline samples of $La_{1-x}Y_xO_{0.5}F_{0.5}BiS_2$ up to $x = 0.40$ and observed a solubility limit near $x = 0.20$. All samples crystallized in the $CeOBiS_2$-type structure. The physical properties of the system were investigated via electrical resistivity, dc and ac magnetic susceptibility, and specific heat measurements. We found a correlation between the lattice constant $c$, the La-O-La bond angle, and the critical temperature $T_c$. The chemical pressure induced by yttrium substitution for lanthanum is insufficient to induce the high-$T_c$ and/or the structural phase transitions observed in measurements of $LaO_{0.5}F_{0.5}BiS_2$ under applied pressure.

The text and data presented in this chapter are reprints of material that appears in "Effect of yttrium substitution on the superconducting properties of $La_{1-x}Y_xO_{0.5}F_{0.5}BiS_2$," I. Jeon, D. Yazici, B. D. White, A. J. Friedman, and M. B. Maple, *Phys. Rev. B* **90**, 054510 (2014). The dissertation author is the primary investigator and author of this article.

## Bibliography

[1] Y. Mizuguchi, H. Fujihisa, Y. Gotoh, K. Suzuki, H. Usui, K. Kuroki, S. Demura, Y. Takano, H. Izawa, and O. Miura, Phys. Rev. B **86**, 220510 (2012).

[2] S. K. Singh, A. Kumar, B. Gahtori, Shruti, G. Sharma, S. Patnaik, and V. P. S. Awana, J. Am. Chem. Soc. **134**, 16504 (2012).

[3] Y. Mizuguchi, S. Demura, K. Deguchi, Y. Takano, H. Fujihisa, Y. Gotoh, H. Izawa, and O. Miura, J. Phys. Soc. Jpn. **81**, 114725 (2012).

[4] S. Demura, Y. Mizuguchi, K. Deguchi, H. Okazaki, H. Hara, T. Watanabe, S. J. Denholme, M. Fujioka, T. Ozaki, H. Fujihisa, Y. Gotoh, O. Miura, T. Yamaguchi, H. Takeya, and Y. Takano, J. Phys. Soc. Jpn. **82**, 033708 (2013).

[5] K. Deguchi, Y. Mizuguchi, S. Demura, H. Hara, T. Watanabe, S. J. Denholme, M. Fujioka, H. Okazaki, T. Ozaki, H. Takeya, T. Yamaguchi, O. Miura, and Y. Takano, Europhys.Lett. **101**, 17004 (2013).

[6] J. Xing, S. Li, X. Ding, H. Yang, and H.-H. Wen, Phys. Rev. B **86**, 214518 (2012).

[7] D. Yazici, K. Huang, B. D. White, A. H. Chang, A. J. Friedman, and M. B. Maple, Philos. Mag. **93**, 673 (2012).

[8] R. Jha and V. P. S. Awana, J. Sup. Novel Mag. **27**, 1 (2014).

[9] R. Jha, A. Kumar, S. Kumar Singh, and V. P. S. Awana, J. Appl. Phys. **113**, 056102 (2013).

[10] R. Jha, A. Kumar, S. K. Singh, and V. P. S. Awana, J. Sup. Novel Mag. **26**, 499 (2013).

[11] V. P. S. Awana, A. Kumar, R. Jha, S. Kumar Singh, A. Pal, Shruti, J. Saha, and S. Patnaik, Solid State Commun. **157**, 21 (2013).

[12] R. Jha and V. P. S. Awana, Mater. Res. Express **1**, 016002 (2014).

[13] D. Yazici, K. Huang, B. D. White, I. Jeon, V. W. Burnett, A. J. Friedman, I. K. Lum, M. Nallaiyan, S. Spagna, and M. B. Maple, Phys. Rev. B **87**, 174512 (2013).

[14] X. Lin, X. Ni, B. Chen, X. Xu, X. Yang, J. Dai, Y. Li, X. Yang, Y. Luo, Q. Tao, G. Cao, and Z. Xu, Phys. Rev. B **87**, 020504 (2013).

[15] Y. Li, X. Lin, L. Li, N. Zhou, X. Xu, C. Cao, J. Dai, L. Zhang, Y. Luo, W. Jiao, Q. Tao, G. Cao, and Z. Xu, Supercond. Sci. Technol. **27**, 035009 (2014).

[16] H. Sakai, D. Kotajima, K. Saito, H. Wadati, Y. Wakisaka, M. Mizumaki, K. Nitta, Y. Tokura, and S. Ishiwata, J. Phys. Soc. Jpn. **83**, 014709 (2014).

[17] H. Usui, K. Suzuki, and K. Kuroki, Phys. Rev. B **86**, 220501 (2012).

[18] X. Wan, H.-C. Ding, S. Y. Savrasov, and C.-G. Duan, Phys. Rev. B **87**, 115124 (2013).

[19] Shruti, P. Srivastava, and S. Patnaik, J. Phys.: Condens. Matter **25**, 339601 (2013).

[20] G. Lamura, T. Shiroka, P. Bonfa, S. Sanna, R. De Renzi, C. Baines, H. Luetkens, J. Kajitani, Y. Mizuguchi, O. Miura, K. Deguchi, S. Demura, Y. Takano, and M. Putti, Phys. Rev. B **88**, 180509 (2013).

[21] T. Yildirim, Phys. Rev. B **87**, 020506 (2013).

[22] J. Lee, M. B. Stone, A. Huq, T. Yildirim, G. Ehlers, Y. Mizuguchi, O. Miura, Y. Takano, K. Deguchi, S. Demura, and S. H. Lee, Phys. Rev. B **87**, 205134 (2013).

[23] H. Kotegawa, Y. Tomita, H. Tou, H. Izawa, Y. Mizuguchi, O. Miura, S. Demura, K. Deguchi, and Y. Takano, J. Phys. Soc. Jpn. **81**, 103702 (2012).

[24] G. Kalai Selvan, M. Kanagaraj, S. Esakki Muthu, R. Jha, V. P. S. Awana, and S. Arumugam, Phys. Status Solidi R **7**, 510 (2013).

[25] G. Kalai Selvan, M. Kanagaraj, R. Jha, V. P. S. Awana, and S. Arumugam, arXiv:1307.4877 (2013).

[26] C. T. Wolowiec, D. Yazici, B. D. White, K. Huang, and M. B. Maple, Phys. Rev. B **88**, 064503 (2013).

[27] C. T. Wolowiec, B. D. White, I. Jeon, D. Yazici, K. Huang, and M. B. Maple, J. Phys.: Condens. Matter **25**, 422201 (2013).

[28] J. Kajitani, K. Deguchi, A. Omachi, T. Hiroi, Y. Takano, H. Takatsu, H. Kadowaki, O. Miura, and Y. Mizuguchi, Solid State Commun. **181**, 1 (2014).

[29] K. Mori, Y. Isikawa, K. Kobayashi, M. Sasakawa, and K. Sato, Physica B+C **148**, 465 (1987).

[30] T. F. Liao, H. H. Sung, K. J. Syu, and W. H. Lee, Solid State Commun. **149**, 448 (2009).

[31] H. Mizoguchi, T. Kuroda, T. Kamiya, and H. Hosono, Phys. Rev. Lett. **106**, 237001 (2011).

[32] P. M. Shirage, K. Miyazawa, H. Kito, H. Eisaki, and A. Iyo, Phys. Rev. B **78**, 172503 (2008).

[33] M. Tropeano, C. Fanciulli, F. Canepa, M. R. Cimberle, C. Ferdeghini, G. Lamura, A. Martinelli, M. Putti, M. Vignolo, and A. Palenzona, Phys. Rev. B **79**, 174523 (2009).

[34] T. Tomita, M. Ebata, H. Soeda, H. Takahashi, H. Fujihisa, Y. Gotoh, Y. Mizuguchi, H. Izawa, O. Miura, S. Demura, K. Deguchi, and Y. Takano, J. Phys. Soc. Jpn. **83**, 063704 (2014).

[35] A. C. Larson and R. B. V. Dreele, Los Alamos National Laboratory Report (1994).

[36] B. Toby, J. Appl. Crystallogr. **34**, 210 (2001).

[37] R. D. Shannon, Acta Cryst. A **32**, 751 (1976).

[38] F. Bouquet, Y. Wang, R. A. Fisher, D. G. Hinks, J. D. Jorgensen, A. Junod, and N. E. Phillips, Europhys. Lett. **56**, 856 (2001).

[39] N. W. Ashcroft and N. D. Mermin, *Solid State Physics* (Saunders College, Philadelphia, 1976).

[40] S. Li, H. Yang, D. Fang, Z. Wang, J. Tao, X. Ding, and H. Wen, Sci. China-Phys. Mech. Astron. **56**, 2019 (2013).

[41] J. Liu, D. Fang, Z. Wang, J. Xing, Z. Du, S. Li, X. Zhu, H. Yang, and H.-H. Wen, Europhys. Lett. **106**, 67002 (2014).

[42] J. Kajitani, K. Deguchi, T. Hiroi, A. Omachi, S. Demura, Y. Takano, O. Miura, and Y. Mizuguchi, J. Phys. Soc. Jpn. **83**, 065002 (2014).

[43] L. K. Zeng, X. B. Wang, J. Ma, P. Richard, S. M. Nie, H. M. Weng, N. L. Wang, Z. Wang, T. Qian, and H. Ding, arXiv:1402.1833 (2014).

[44] X. B. Wang, S. M. Nie, H. P. Wang, P. Zheng, P. Wang, T. Dong, H. M. Weng, and N. L. Wang, Phys. Rev. B **90**, 054507 (2014).

[45] Z. R. Ye, H. F. Yang, D. W. Shen, J. Jiang, X. H. Niu, D. L. Feng, Y. P. Du, X. G. Wan, J. Z. Liu, X. Y. Zhu, H. H. Wen, and M. H. Jiang, Phys. Rev. B **90**, 045116 (2014).

# Chapter IV

# Investigation of superconducting and normal-state properties of the filled-skutterudite system $PrPt_4Ge_{12-x}Sb_x$

## IV.A Introduction

Filled-skutterudite compounds with the generic chemical formula $MT_4X_{12}$, where $M$ is an alkali metal, alkaline earth, lanthanide, or actinide, $T$ is a transition metal from the Fe or Co column, and $X$ is a pnictogen [1], have been of interest to physicists and chemists worldwide due to the various types of strongly correlated electron behaviors they exhibit and their potential for use in applications; intriguing properties studied in filled skutterudite compounds include conventional BCS-type superconductivity, unconventional superconductivity, Kondo-lattice behavior, valence fluctuations, non-Fermi liquid behavior, heavy-fermion behavior, Kondo-insulator behavior, metal-insulator transitions, magnetic ordering, spin fluctuations, and quadrupolar order [2–16]. Filled skutterudites also have

demonstrated potential viability for use in thermoelectric applications [3, 14, 15].

Among the filled-skutterudite compounds, Pr-based systems, in particular, exhibit unusual physical properties [2, 4, 12, 17, 18], including a metal-insulator transition and a low-field ordered phase in $PrRu_4P_{12}$ and $PrFe_4P_{12}$, respectively [17, 19]. The heavy-fermion superconducting state in $PrOs_4Sb_{12}$ has attracted considerable interest and was the first such state to be discovered in a Pr-based system. It has a very large Sommerfeld coefficient, $\gamma \sim 500$ mJ/mol K$^2$ [4, 11], and exhibits unconventional superconductivity in which there is evidence for time-reversal symmetry breaking [8], multiple superconducting bands [16, 20, 21], point nodes in the energy gap [21, 22], and potential spin-triplet pairing of electrons [23].

Recently, a new class of filled-skutterudite compounds with the chemical formula $MPt_4Ge_{12}$ has been synthesized and studied [24–30]. The compounds with $M$ = Sr, Ba, La, Pr, and Th have all been found to display superconductivity. For (Sr,Ba)$Pt_4Ge_{12}$, the superconducting transition temperatures, $T_c$, are $\sim$ 5.4 and 5.1 K, respectively, and BCS-like superconductivity is observed, originating from the Pt-Ge cage structure. For (La,Pr)$Pt_4Ge_{12}$, superconductivity occurs at relatively high temperatures of $T_c \sim 8.2$ and 7.9 K, respectively. Both $LaPt_4Ge_{12}$ and $ThPt_4Ge_{12}$ exhibit conventional BCS-type superconductivity; however, $ThPt_4Ge_{12}$ was also found to be a clean-limit strong-coupling superconductor with $T_c = 4.6$ K.

In contrast, the compound $PrPt_4Ge_{12}$ displays unconventional superconductivity that is similar to that of $PrOs_4Sb_{12}$ in several ways. Transverse muon spin relaxation ($\mu$SR) and specific heat measurements suggest point nodes in the superconducting energy gap of $PrPt_4Ge_{12}$, and zero-field $\mu$SR measurements provide evidence for time-reversal symmetry breaking in the superconducting state [28, 31]. The compound $PrPt_4Ge_{12}$ exhibits a similar type of multiband unconventional su-

perconductivity [32–34]. A recent study of Ce substitution into the filler sites for Pr ions in $PrPt_4Ge_{12}$ reported the suppression of superconductivity with increasing Ce concentration and suggested a crossover from a nodal to nodeless superconducting energy gap or the suppression of multiple superconducting energy bands, revealing a single, robust BCS-type superconducting energy gap [35].

A few studies attempting to understand the effect of chemical substitution within the Pt-Ge cage have been conducted. Upon substitution of Au for Pt in $BaPt_4Ge_{12}$, the electronic density of states and superconducting transition temperature $T_c$ increase with increasing Au concentration [36]. The effect of Sb substitution for Ge has also been studied for several Pt-Ge based skutterudite compounds: The compound $CePt_4Ge_{12}$ is close to a boundary between Ce intermediate valence and Kondo-lattice behavior [27, 37]. By substituting Sb for Ge, $CePt_4Ge_{12}$ is tuned from a nearly intermediate-valent paramagnet, through a non-Fermi liquid phase, and into an antiferromagnetically-ordered phase with localized Ce $4f$ magnetic moments [38, 39]. A rapid suppression of superconductivity in the system $LaPt_4Ge_{12-x}Sb_x$ with increasing $x$ is observed, accompanied by a decrease of charge-carrier density and an increase of the Seebeck effect at room temperature by about one order of magnitude [40].

Motivated by previous studies, and in order to further investigate the unresolved nature of superconductivity in the compound $PrPt_4Ge_{12}$, we undertook a systematic study of the $PrPt_4Ge_{12-x}Sb_x$ system. The evolution of superconducting properties with increasing Sb concentration was investigated by means of x-ray diffraction, electrical resistivity in zero and applied magnetic fields, DC and AC magnetic susceptibility, and specific heat measurements. We observed a suppression of superconductivity with positive curvature in a plot of $T_c$ versus Sb concentration; above $x = 4$, there is no evidence for superconductivity down to 140 mK. Our results from specific heat measurements is similar to that of previous

studies, suggesting a possible crossover from a nodal to a nodeless superconducting energy gap or from multiple energy gaps to a single BCS-type superconducting energy gap [32–35]. Evidence for a "rattling" mode for the Pr ions was observed throughout the series, but does not seem to have a strong effect on superconductivity. Conjectures about an observed feature or phase transition of unknown origin above $x = 4$ are also discussed.

## IV.B Experimental Details

Polycrystalline specimens of the $PrPt_4Ge_{12-x}Sb_x$ system were synthesized by arc-melting on a water-cooled copper hearth under an Ar atmosphere with a Zr getter. The starting materials were obtained from Pr ingots (Alfa Aesar 99.9%), Pt sponge (99.9999+%), Ge pieces (Alfa Aesar 99.9999+%), and Sb pieces (Alfa Aesar 99%). These starting materials were weighed out in accordance with the stoichiometric ratios and arc-melted, turned over, and arc-melted again a total of five times to promote homogeneity of the samples. The arc-melted boules were then annealed in sealed quartz ampoules (containing 150 torr of Ar at room temperature) for 336 hours at 750 °C. The crystal structure was determined by x-ray powder diffraction (XRD) using a Bruker D8 Discover x-ray diffractometer with Cu-$K_\alpha$ radiation, and XRD patterns were analyzed via Rietveld refinement using the GSAS+EXPGUI software package [41, 42]. The electrical resistivity was measured from 1.1 K to 300 K using a standard four-wire method with a Linear Research LR700 AC resistance bridge in a home-built probe in a liquid $^4$He Dewar, and down to 140 mK using a commercial $^3$He-$^4$He dilution refrigerator. Magnetic susceptibility measurements were performed between 2 K and 300 K in magnetic fields up to 7 T using a Quantum Design Magnetic Property Measurement System (MPMS). Alternating current magnetic susceptibility measurements were made

down to $\sim$ 1.1 K in a liquid $^4$He Dewar using home-built mutual inductance coils. Specific heat measurements were carried out at temperatures down to 1.8 K with a Quantum Design Physical Property Measurement System (PPMS) DynaCool.

## IV.C Results

### IV.C.1 X-ray diffraction

Figure 1 shows results from XRD data for $PrPt_4Ge_{12-x}Sb_x$ ($0 \leq x \leq 5$). All of the XRD patterns are well indexed with the cubic filled-skutterudite crystal structure with space group $Im\bar{3}$. The conventional residual parameters, $R_p$, are in the range from 0.0910 to 0.1595 for $x \leq 5$. Figure IV.1(a) shows a representative XRD pattern for the $PrPt_4Ge_{12-x}Sb_x$ system (for $x = 3.5$) and the resultant fit from the Rietveld refinement. The stars indicate the presence of Pr and/or $PtSb_2$ impurity phases, the amount of which gradually increases with $x$ from $\sim$ 0.2 to 1% by molar ratios for $3 \leq x \leq 5$. Additionally, Ge, $PrSb_2$, and PrPtGe impurities were observed; however, the amount of these impurities is less than 1% by molar ratio, suggesting very weak effects on the properties of these samples. For samples with $x \geq 6$, the dominant phase is $PtSb_2$; the molar ratios of $PtSb_2$ by Rietveld refinement are 6% and 52% for $x = 6$ and 7, respectively, indicating the solubility limit is near or just beyond $x = 6$. This result is consistent with the observation that the lattice parameter $a$ exhibits a plateau for $x \geq 5$ (data not shown). Since the atomic radius of Sb is larger than that of Ge, it is expected that $a$ increases with increasing Sb concentrations. As seen in Figure IV.1(b), we observed that the thermal displacement parameters, $U_{iso}$, for Pr atoms are large compared with values of Pt or Ge/Sb atoms, which is a common feature in filled-skutterudite systems. Figure IV.1(c) displays the occupancies of the Pr and Pt crystallographic positions and the relative ratios of Sb to Sb+Ge occupancies, suggesting that the

Pr sites are not fully occupied down to $\sim 0.7$ for $x \geq 3.5$. A similar result is occasionally observed in other filled skutterudite compounds [43, 44]. This result is also consistent with the increase of Pr-based impurity phases for samples with $x \geq 3$.

### IV.C.2 Electrical Resistivity

Electrical resistivity, $\rho(T)$, data taken in zero magnetic field are shown in Fig. IV.2. All concentrations of Sb display metallic behavior, as shown in Fig. IV.2(a). We show only representative concentrations for visual clarity. The residual resistivity ratio, RRR, versus $x$ is presented in Fig. IV.2(b); a semilogarithmic plot of $(\rho_{300}/\rho_0)$ versus $x$, where $\rho_{300}$ is the room temperature resistivity and $\rho_0$ is the resistivity value right above the superconducting transitions, shows a rapid decrease with increasing $x$ for $0 \leq x \leq 1$, consistent with increased disorder produced by the substitution of Sb for Ge in $PrPt_4Ge_{12}$. A general trend of increasing residual resistivity $\rho_0$ is observed with increasing Sb concentration; however, there is some scatter due to uncertainties in the measurement of the geometrical factors of the resistivity samples. Figure IV.2(c) displays $\rho(T)$ normalized to its value at 10 K versus $x$. $T_c$ was defined as the temperature where $\rho(T)/\rho_{10}$ drops to 50% of its value (i.e., 0.5), and the width of the transition was characterized by the temperatures where $\rho(T)/\rho_{10}$ is 0.9 and 0.1. Even though the superconducting transitions are slightly broadened for $x = 0.5$, 1.5, and 2.5, all transitions are still relatively sharp, indicating good sample homogeneity or small amounts of impurity phases in the samples. $T_c$ is suppressed more rapidly with initial Sb substitution with the effect becoming weaker with increasing $x$, similar to the behavior of the RRR versus $x$. Superconductivity onsets are observed for $x = 3.5$ and 4 in measurements performed down to 140 mK.

Figure IV.3(a) shows $\rho$ versus $T^2$ for representative concentrations, with

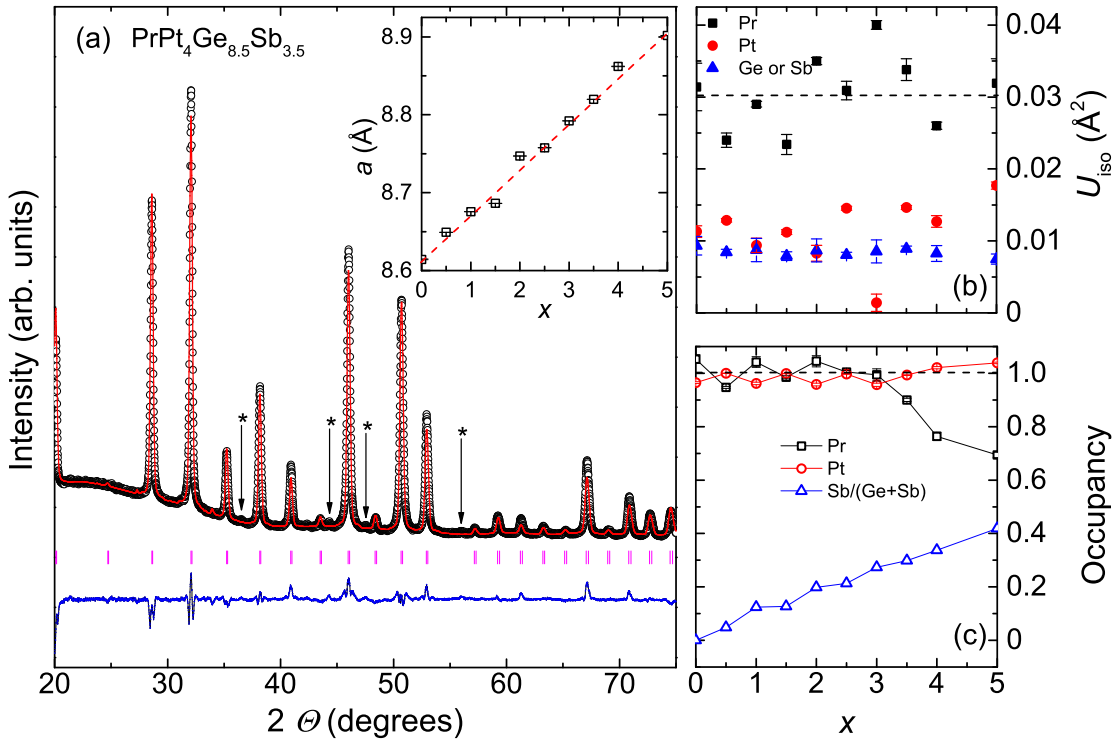


Figure IV.1: (a) X-ray diffraction pattern for $PrPt_4Ge_{8.5}Sb_{3.5}$. The black circles represent the experimental data and the red line represents the fit from the Rietveld refinement of the data. The purple vertical marks indicate the position of expected Bragg reflections for the refined $PrPt_4Ge_{8.5}Sb_{3.5}$ crystal structure and the blue line at the bottom is the difference between observed and calculated intensities. The stars indicate Bragg reflections associated with a Pr or $PtSb_2$ impurity phase. The inset shows a plot of the lattice parameter $a$ versus nominal antimony concentration $x$. The red dashed line is a guide to the eye. (b) Thermal displacement parameter, $U_{\text{iso}}$, of elements versus Sb concentration. Pr atoms have large values compared with Pt and Ge/Sb atoms. (c) Occupancies of Pr and Pt crystallographic positions and the ratio of Sb to Ge + Sb versus Sb concentration $x$. A significant decrease of Pr site occupancy is observed for $x \geq 3.5$.

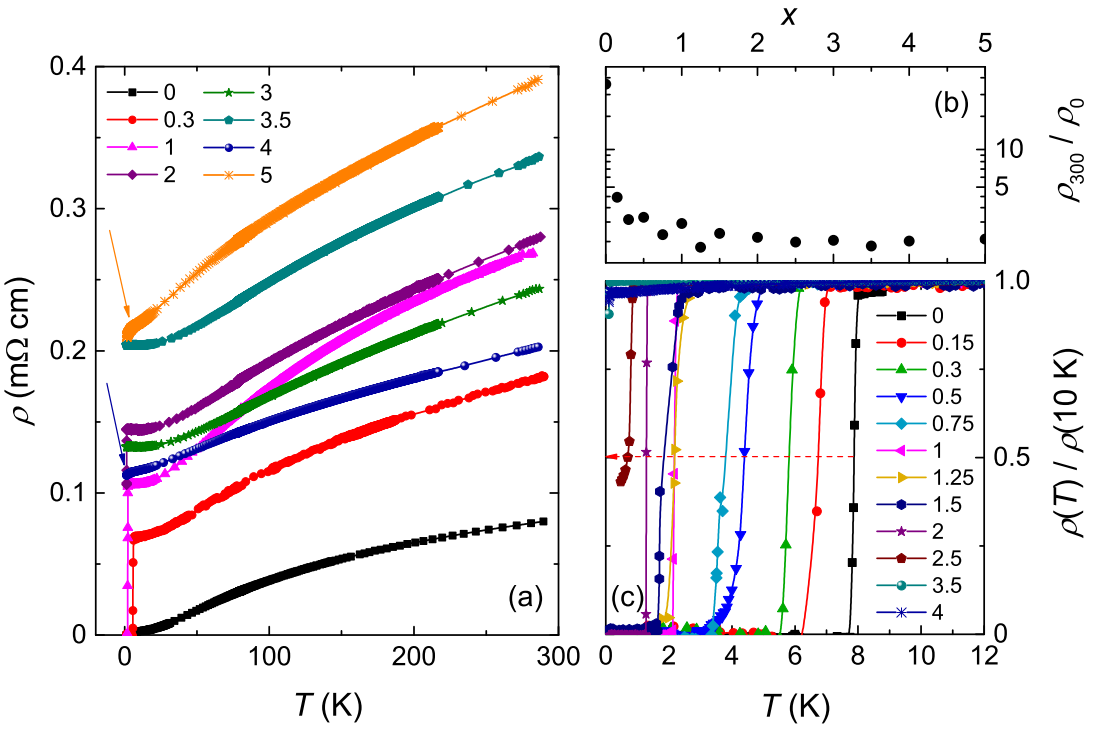


Figure IV.2: (a) Electrical resistivity data $\rho$ versus $T$ for selected $PrPt_4Ge_{12-x}Sb_x$ samples with Sb concentrations $x$ shown in the legend. The arrows indicate a weak downturn feature for $x = 4$ and 5, possibly due to an impurity phase. (b) A semilogarithmic plot of the residual resistivity ratio RRR ($\rho_{300}/\rho_0$) versus $x$ for $PrPt_4Ge_{12-x}Sb_x$. The decrease in RRR with increasing $x$ displays a positive curvature. (c) $\rho(T)$, normalized to its value at 10 K, versus $x$ for selected $PrPt_4Ge_{12-x}Sb_x$ samples. Superconducting transition temperatures $T_c$ decrease with increasing $x$ and onsets of superconductivity are observed for $x = 3.5$ and 4. The red dashed arrow is a guide to the eye.

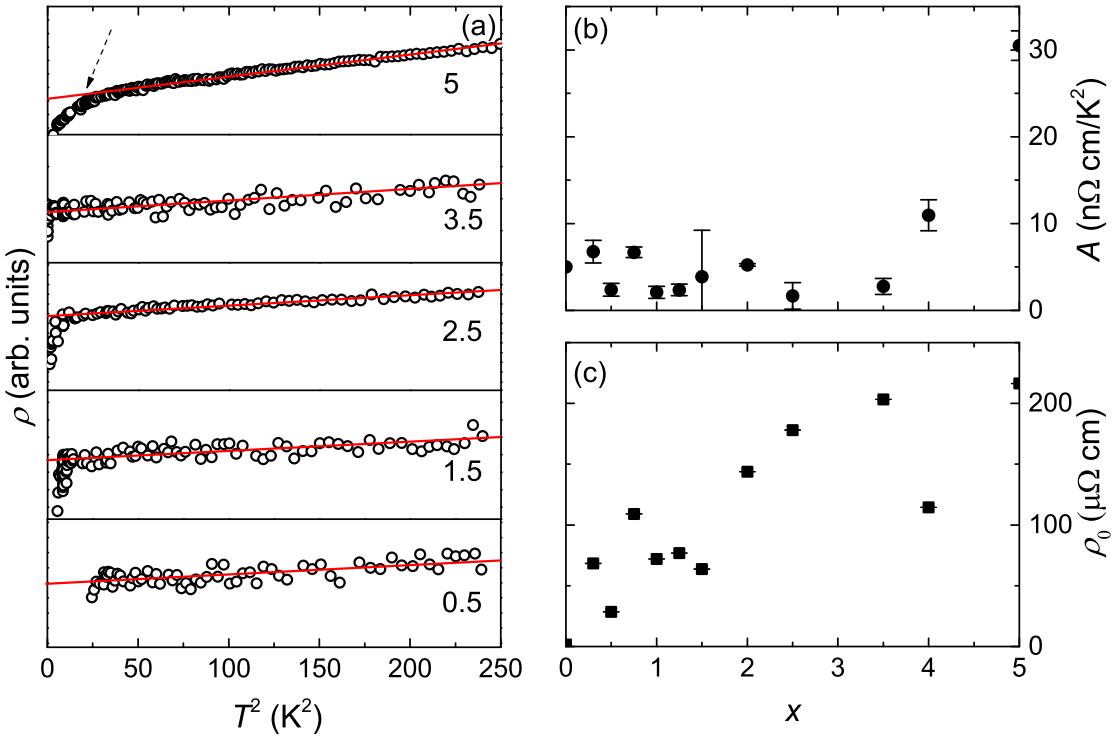


Figure IV.3: (a) A plot of $\rho$ versus $T^2$ for selected concentrations with different y-scales for visual clarity. Power-law fits of $\rho(T) = \rho_0 + AT^2$ were performed up to 250 $K^2$, indicated by the red solid lines. The dashed arrow indicates the deviation from the fit, possibly due to an impurity phase. (b) Coefficient $A$ versus $x$. $A$ scatters between 2 to 7 n$\Omega$ cm/$K^2$ and increases rapidly for $x \geq 4$. (c) The residual resistivity, $\rho_0$, from the fits versus $x$ is shown. $\rho_0$ increases rapidly from $\sim$1.7 to $\sim$216 $\mu\Omega$ cm, consistent with disorder introduced by Sb substitution into $PrPt_4Ge_{12}$.

different y-scales for visual clarity. The red solid lines represent least squares fits to the data with the formula $\rho(T) = \rho_0 + AT^2$ in the temperature range between $T_c^2$ and 250 K$^2$, suggesting Fermi-liquid behavior in $PrPt_4Ge_{12-x}Sb_x$ for $0 \leq x \leq 5$ [35]. Deviations from the fits were observed for the $x = 4$ and 5 samples, which is probably due to the $PtSb_2$ impurity phase. We also performed a resistivity measurement on the samples with $x = 6$, 7, and 12 (data not shown); these inhomogeneous samples exhibit the same feature marked by arrows in Figs. IV.2 and IV.3 at the same temperature and with the same character. For $x = 6$ and 7, the amount of the $PtSb_2$ phase is large; moreover, the $x = 12$ sample turned out to be the compound $PtSb_2$, with a very small amount of $PrPt_4Ge_7Sb_5$. The coefficient, $A$, scatters between 2 to 7 n$\Omega$ cm/K$^2$, increasing to 30 n$\Omega$ cm/K$^2$ for $x \geq 4$. Figure IV.3(c) shows that values of the residual resistivity $\rho_0$ versus $x$, obtained from the fits, increase from $\sim$ 2 to 216 $\mu\Omega$ cm; though, the values of $\rho_0$ fluctuate strongly with increasing $x$ due to uncertainties in the measurement of the geometrical factors of the resistivity samples, as we mentioned previously to explain the behavior seen in Fig. IV.2(a).

We also measured the upper critical fields, $H_{c2}(T)$, for selected samples. In Fig. IV.4(a), the data points were determined from the temperature where $\rho(T)$ decreases to 50% of its value in the normal state just above $T_c$ at fixed magnetic fields, and the width of the transitions was defined using the 10% and 90% values of the drop in $\rho(T)$. In general, the superconducting transitions become broader at higher applied magnetic fields. The derivative $(\mathrm{d}H_{c2}/\mathrm{d}T)_{T=T_c}$ was obtained by fitting straight lines to the data near $H_{c2} = 0$ and estimated values are $\sim -0.39$ T/K for all concentrations. Using the Werthamer-Helfand-Hohenberg (WHH) model [32, 45], where $H_{c2}(0)$ is $-0.693T_c(\mathrm{d}H_{c2}/T)_{T=T_c}$, the temperature dependence of $H_{c2}$ was extracted, as shown in Fig. 4(a). Figure IV.4(b) reveals a rapid decrease of $H_{c2}(0)$ with increasing $x$, showing similar behavior to those

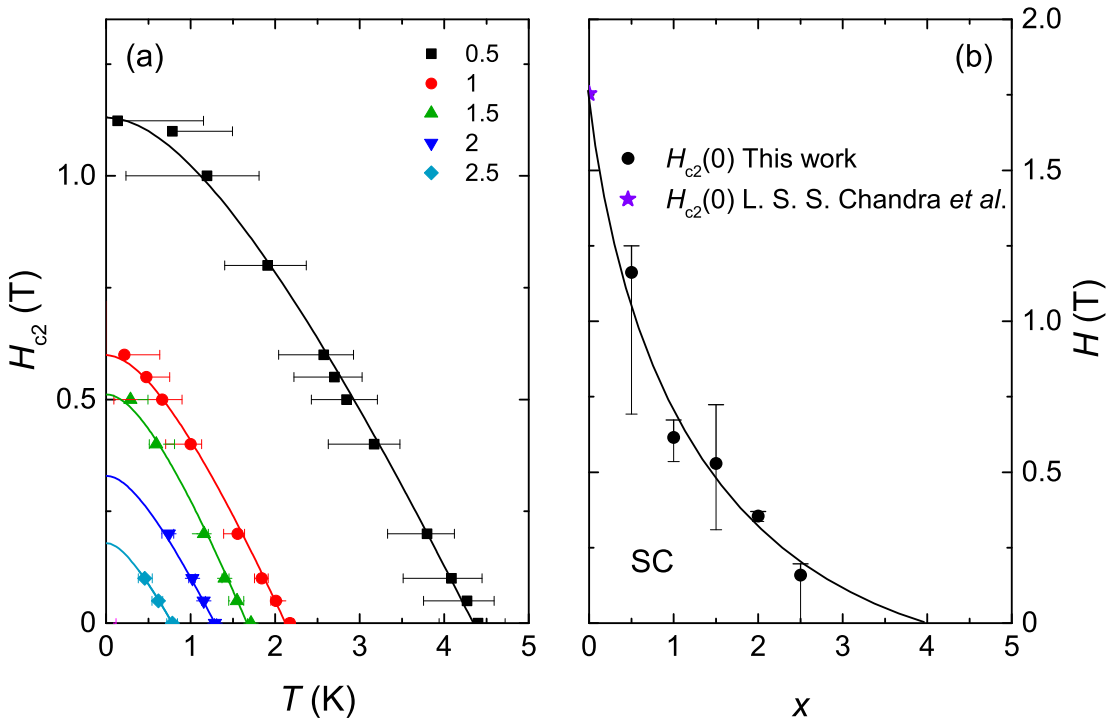


Figure IV.4: (a) Temperature-dependence of the upper critical field $H_{c2}$ for selected samples. The horizontal bars are the transition widths, determined as described in the text. Solid lines are fits of the WHH theory to the data. (b) Magnetic field $H$ - $x$ phase diagram of $PrPt_4Ge_{12-x}Sb_x$ at $T = 0$ K. The solid line, which is a guide to the eye, represents the rapid suppression of the 0 K value of the upper critical field, $H_{c2}(0)$, with increasing $x$. The values of $H_{c2}(0)$ were determined from the WHH fits in Fig. IV.4(a).

observed in the rapid suppressions of $T_c$ and the RRR with increasing $x$. It is noteworthy that the curvature of $H_{c2}(T)$ seems to decrease with increasing $x$, similar to the behavior previously observed in the $Pr(Os_{1-x}Ru_x)_4Sb_{12}$ system [46].

### IV.C.3 Magnetic Susceptibility

Magnetization divided by applied magnetic field, $M/H$, versus $T$ data are displayed in Fig. IV.5(a). We performed measurements under applied magnetic field of $H = 0.5$ T for the $x = 0$ sample and 1 T for the rest of the samples containing Sb. The magnitude of $M/H$ decreases with increasing $x$; however, an increase in magnitude and low-temperature upturns were observed for $x \geq 4$, which are expected from the XRD results. The decrease of the estimated Pr occupancy (see Fig. IV.1(c)) and presence of ∼1 atomic percent of Pr and $PtSb_2$ impurity phases in $x = 4$ and 5 samples might be the reasons. The inset of Fig. IV.5(a) shows superconducting transitions for $x = 0$ and 0.5 under an applied magnetic field $H = 10$ Oe. $T_c$ was defined by the point where zero-field-cooled (ZFC) and field-cooled (FC) data deviated from one another. The superconducting volume fractions were estimated from the ZFC $\chi(T)$ data by using the relation $4\pi\chi \times d$, where $d$ is the molar density of the samples in units of mol/cm$^3$. The superconducting samples with $x = 0$, 0.5, 1, 1.5, and 2 have volume fractions slightly greater than 1, which results from exclusion of demagnetization factor corrections in this analysis; nevertheless, these results offer strong support for bulk superconductivity in the system $PrPt_4Ge_{12-x}Sb_x$.

We fit the $M/H$ versus $T$ data in Fig. IV.5(a) to a Curie-Weiss law in the temperature range from 75 to 300 K,

$$M/H = C_0/(T - \Theta_{\mathrm{CW}}), \tag{IV.1}$$

where $C_0$ is the Curie constant and $\Theta_{\rm CW}$ is the Curie-Weiss temperature. The average effective magnetic moment, $\mu_{eff}$, of the Pr ion is extracted from the relation $C_0 = \mu_{eff}^2 N_A/3k_B$, where $N_A$ is Avogadro's number and $k_B$ is Boltzmann's constant. The best fit values are shown in Fig. IV.6. Values of $\mu_{eff}$ scatter around $3.58\mu_B$, the value for $Pr^{3+}$ free ions, calculated using Hund's rules. The Curie-Weiss temperatures, $\Theta_{\rm CW}$, are nearly independent of $x$ with a value of $\sim -10$ K. Real and imaginary components of the alternating current magnetic susceptibility, $\chi'$ and $\chi''$, respectively, for the samples with $x = 1$, 1.5, and 2 are shown in Fig. IV.5(b). Clear signatures of superconductivity were observed and $T_c$ was defined as the temperatures where $\chi''$ drops sharply.

Isothermal magnetization measurements were also performed at 2 K under applied magnetic fields up to 7 T (data not shown). We observed a rapid suppression of superconductivity below 1 T and above that, paramagnetism was observed; however, slight curvatures in the isothermal magnetization for the samples with $x = 4$ and 5 were seen, possibly due to small concentrations of paramagnetic impurities, as we discussed in previous sections. In order to roughly estimate the concentrations of paramagnetic impurities, Gd was used as a standard impurity and assumed to be located at the Pr sites. This choice was arbitrary; it could be other lanthanide ions on the Pr site or $3d$ transition metal ions such as Fe on the Pt site. The impurity concentration ($N/V$) was determined in two ways: Curie law fits to the upturns at low temperatures and the procedure described in reference [47], using isothermal magnetization data. For the Curie law fits, we used the relation $N/V = 3C_0 k_{\rm B}/(N_{\rm A}\mu_{\rm eff}^2)$, where $\mu_{\rm eff}^2$ is the effective magnetic moment of Gd ions (7.94 $\mu_{\rm B}$). Both methods yielded estimates of the impurity concentration of about $1 \sim 2\%$ of the lanthanide ions, consistent with the results from XRD measurements. Since we have evidence for larger amounts of impurities in the samples with high Sb concentrations, we excluded other possibilities for the upturn at low

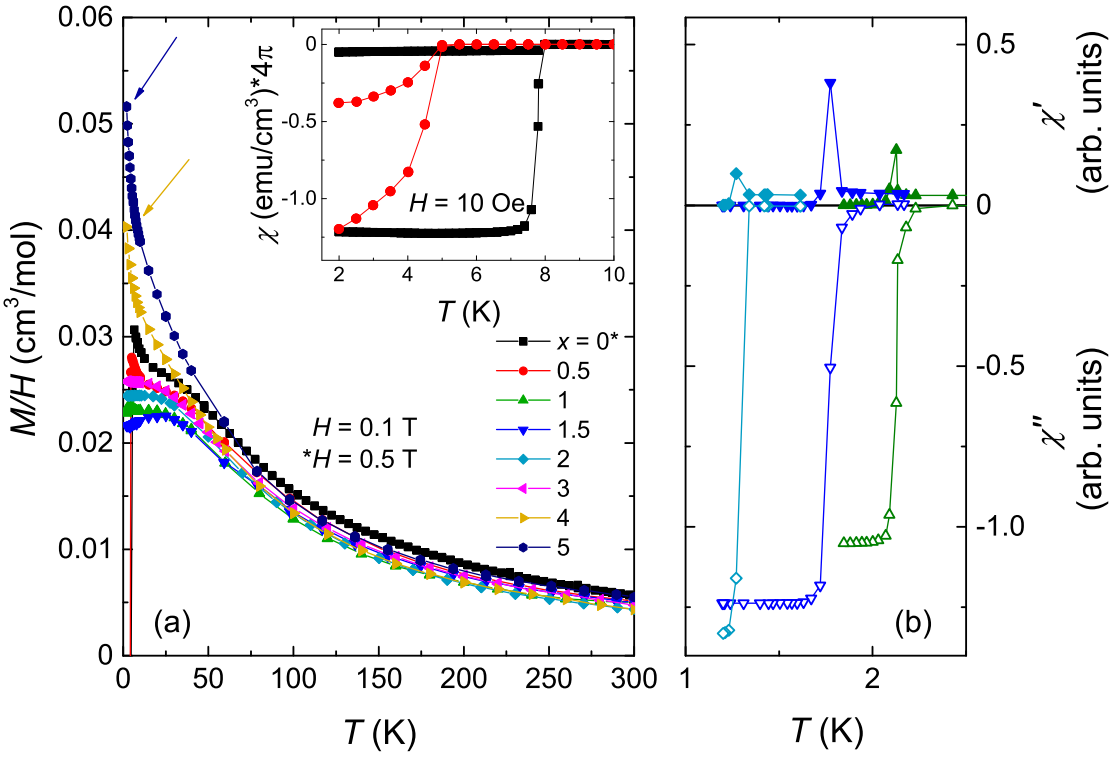


Figure IV.5: (a) Magnetization divided by applied magnetic field, $M/H$, versus temperature $T$ for $PrPt_4Ge_{12-x}Sb_x$ with selected concentrations, measured in applied magnetic fields of $H = 0.5$ T for the sample with $x = 0$ and $H = 1$ T for the samples with $x > 0$. Solid arrows indicate upturns due to small amounts of paramagnetic impurities, as discussed in the text. The inset highlights the Meissner effect and diamagnetic shielding plotting $4\pi\chi$ versus $T$ for the $x = 0$ and 0.5 samples. (b) Alternating current magnetic susceptibility $\chi'$ and $\chi''$ versus temperature $T$ for $x = 1$, 1.5, and 2. (a), (b) Superconducting volume fractions are close to 1. The deviations from unity are presumably due to not accounting for the demagnetization factor.

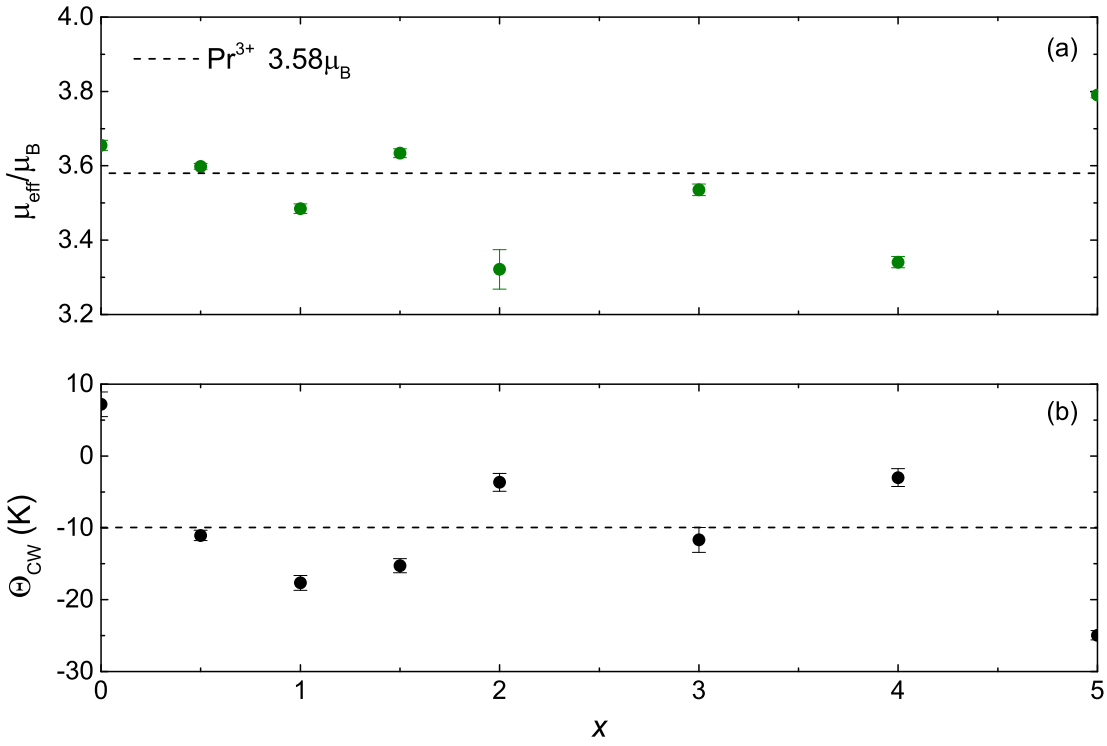


Figure IV.6: (a), (b) Effective magnetic moment ($\mu_{eff}/\mu_B$) and Curie-Weiss temperature $\Theta_{\rm CW}$ versus $x$ from the Curie-Weiss fits to $M/H$ data. $\mu_{eff}/\mu_B$ values scatter around $\mu_{eff} = 3.58\mu_B$, the value expected for the $Pr^{3+}$ free ion, indicated by the dashed line. Both $\mu_{eff}/\mu_B$ and $\Theta_{\rm CW}$ are nearly $x$ independent. The dashed line in (b) is a guide to the eye.

temperatures, such as a change in the crystalline electric field ground state of the Pr ions.

### IV.C.4 Specific Heat

Specific heat, $C$, versus $T$ data are shown in Fig. IV.7(a). The feature in $C/T$ associated with superconductivity was only observed in the $x = 0$ and 0.5 samples (the $T_c$ values for $x \geq 1$ are at temperatures below the low temperature limit of the PPMS DynaCool). Superconducting transition temperatures $T_c$ were determined with the aid of an idealized entropy-conserving constructions (not shown). The resultant $T_c$ values are consistent with the values obtained from the $\rho(T)$ and $\chi(T)$ measurements.

In order to analyze the behavior of the electronic and phonon contributions to $C$, we first attempted to employ linear fits of $C/T$ versus $T^2$ to the data, which is a commonly-used method [35]. However, this method is inappropriate for $PrPt_4Ge_{12-x}Sb_x$; the electronic specific heat coefficient, $\gamma'$, becomes negative for $x \geq 4$, possibly due to low temperature upturns in the $C/T$ versus $T^2$ plots (data not shown). The Debye temperature, $\Theta'_{\rm D}$, extracted from the coefficient $\beta$ using the equation $C(T)/T = \gamma' + \beta T^2$, increases from $\sim$ 192 K to $\sim$ 271 K over the entire concentration range (data not shown). Possible explanations will be addressed below in the discussion section.

Since we have evidence that the specific heat data need to be analyzed using an alternative method, we considered contributions due to rattling motion of Pr ions or a Pr nuclear Schottky. We reasoned that a nuclear Schottky contribution is not reasonable since it could not fully account for the continuous increase of the Debye temperature, $\Theta'_{\rm D}$, for all $x$. We found that introducing an Einstein contribution is more appropriate for the analysis in this study. For example, the Einstein model accurately describes the temperature dependence of the specific heat of filled

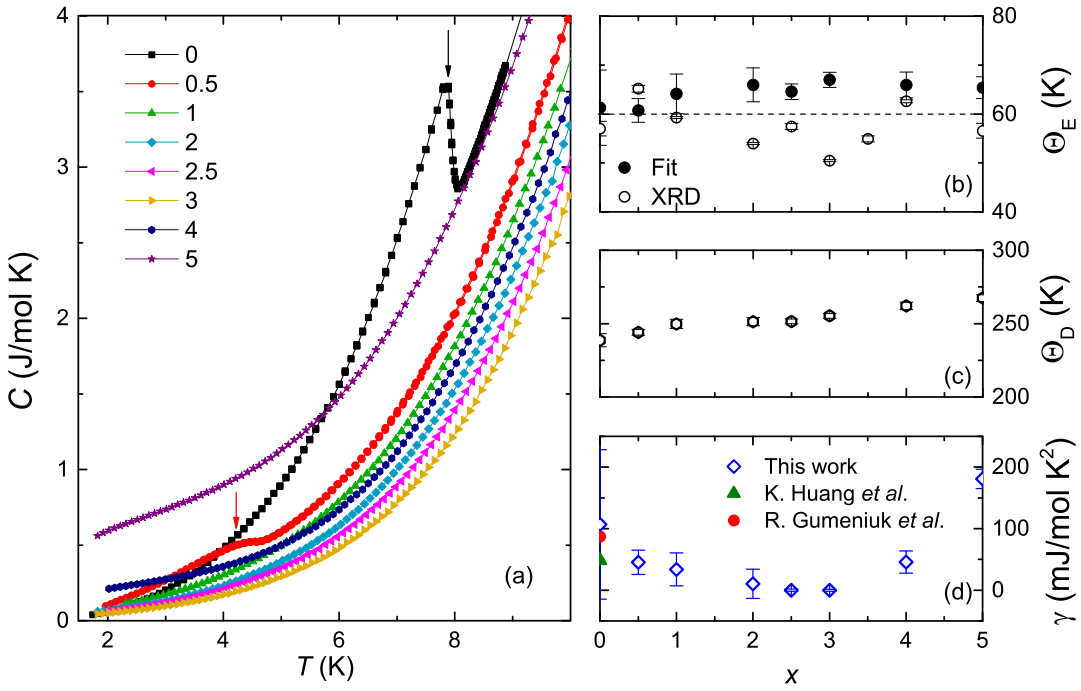


Figure IV.7: (a) Specific heat $C$ versus temperature $T$ for $PrPt_4Ge_{12-x}Sb_x$. Arrows indicate superconducting transitions for the $x = 0$ and 0.5 samples. (b) Einstein temperature, $\Theta_E$, versus $x$. Solid data points are from fits of the specific heat data that include the Einstein model. Open circles are extracted from the relation between $\Theta_E$ and thermal displacement parameter, $U_{iso}$, from Rietveld refinement of the XRD data (see text). $\Theta_E$ scatters around $\sim 60$ K; the dashed line is a guide to the eye. (c) Debye temperature, $\Theta_D$, versus $x$. $\Theta_D$ increases slightly with increasing $x$. (d) The Sommerfeld coefficient, $\gamma$, obtained from fits using the Einstein model, versus $x$. The electronic specific heat coefficient $\gamma$ decreases as $x$ increases until $x = 3$, and is enhanced as $x$ increases up to $x = 5$. The value of $\gamma$ for $PrPt_4Ge_{12}$ in this work has a large error bar since we included the Einstein model; thus, the values obtained using other methods are also presented for reference [26, 35].

$Tl_{0.22}Co_4Sb_{12}$ and unfilled $Co_4Sb_{12}$ skutterudite compounds [48]. Also, the broad kink observed in the $C/T$ versus $T^2$ data for $NdOs_4Sb_{12}$ was explained by using a combination of Debye and Einstein models [49], so there exists some precedent for including an Einstein model in analysis of specific heat data. If Pr ions behave as Einstein oscillators, the relationship between the thermal displacement parameter, $U_{\mathrm{iso}}$, and the Einstein temperature, $\Theta_{\mathrm{E}}$, is given by the expression:

$$U_{\mathrm{iso}} = \frac{\hbar^2}{2m_{\mathrm{Pr}}k_{\mathrm{B}}\Theta_{\mathrm{E}}} \coth\left(\frac{\Theta_{\mathrm{E}}}{2T}\right), \tag{IV.2}$$

where $m_{\mathrm{Pr}}$ is the mass of the Pr ion and $k_{\mathrm{B}}$ is the Boltzman constant. For all $x$, estimated values of $\Theta_{\mathrm{E}}$ are $\sim$ 60 K, as shown in Fig. IV.7(b). Since there is support for the possibility that Pr ions are behaving like Einstein oscillators, the specific heat can be expressed as $C = \gamma T + C_{\mathrm{Ein}}(T) + C_{\mathrm{Deb}}(T)$ [49], where

$$C_{\mathrm{Ein}}(T) = r \cdot 3R\frac{(\Theta_{\mathrm{E}}/T)^2 e^{(\Theta_{\mathrm{E}}/T)}}{(e^{(\Theta_{\mathrm{E}}/T)}-1)^2}, \tag{IV.3}$$

$$C_{\mathrm{Deb}}(T) = (17-r) \cdot \frac{12\pi^4}{5} R\left(\frac{T}{\Theta_{\mathrm{D}}}\right)^3, \tag{IV.4}$$

$r$ is the mixing ratio of Pr ions, and $R$ is the universal gas constant. We assumed that only Pr ions are behaving like Einstein oscillators in this analysis; thus, the mixing ratio is constrained to be $r \leq 1$. The least-squares fits of $\gamma T + C_{\mathrm{Ein}}(T) + C_{\mathrm{Deb}}(T)$ to the $C(T)$ data were performed in the temperature range between 1.8 and 30 K and corresponding best-fit values for $\gamma$, $\Theta_{\mathrm{E}}$, and $\Theta_{\mathrm{D}}$ were extracted. As shown in Fig. IV.7(b), $\Theta_{\mathrm{E}}$ scatters in the range of $\sim$ 60 to 65 K, indicating a consistent result with the values from the XRD analysis using Eq. (IV.2). The $\Theta_{\mathrm{D}}$ versus $x$ plot in Fig. IV.7(c) exhibits a relatively modest increase of $\Theta_{\mathrm{D}}$ with $x$ compared to the analysis of $C(T)/T = \gamma' + \beta T^2$ fits to the specific data. The electronic specific heat coefficient $\gamma$, presented in Fig. IV.7(d), first decreases from

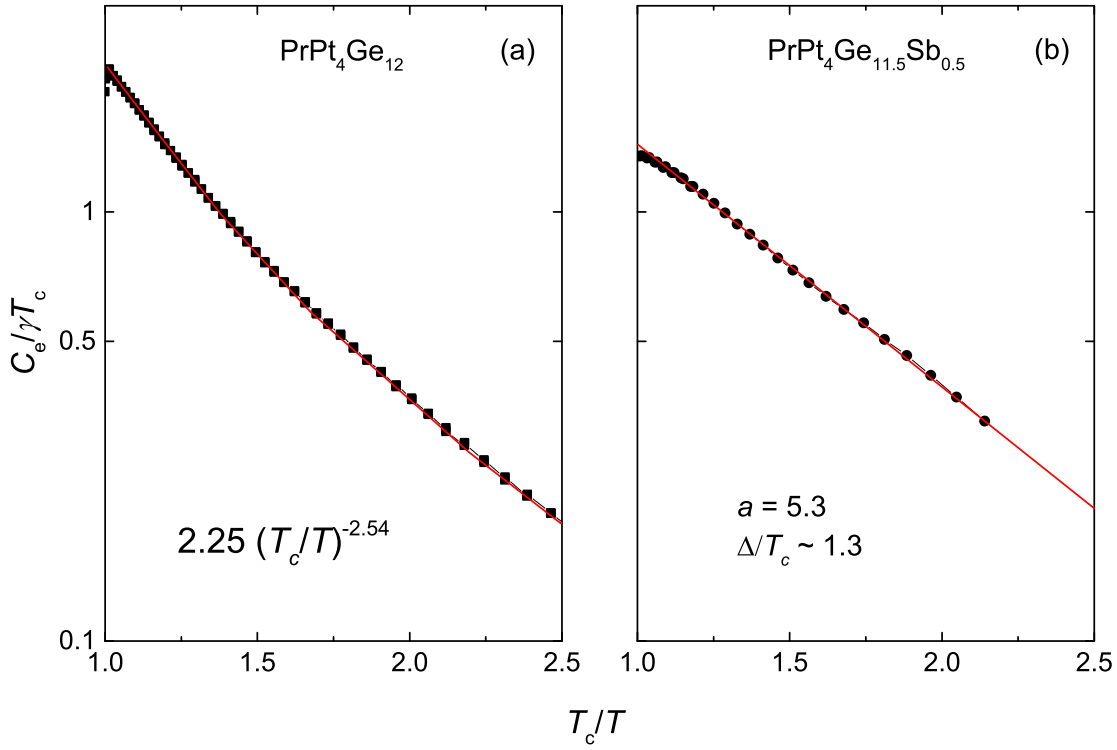


Figure IV.8: (a) and (b): Semilogarithmic plots of the electronic contribution to specific heat, $C_e/\gamma T_c$, in the superconducting state versus $T_c/T$ for $PrPt_4Ge_{12}$ and $PrPt_4Ge_{11.5}Sb_{0.5}$, respectively. The red lines represent the best fits to the data with $2.25(T_c/T)^{-2.54}$ and $ae^{-\Delta/T_c}$, where $a = 5.3$ and $\Delta/T_c = 1.3$ for $PrPt_4Ge_{12}$ and $PrPt_4Ge_{11.5}Sb_{0.5}$, respectively.

$\sim 107$ at $x = 0$ to $\sim 1$ mJ/mol K$^2$ at $x = 3$, and then increases to $\sim 180$ mJ/mol K$^2$ for $x \geq 4$. Both $\Theta_D$ and $\gamma$ values for $x = 0$ are larger than previously reported values, $\gamma'$, of 48 and 87 mJ/mol K$^2$, respectively [26, 35]; however, this is expected due to the different methods used to extract the $\Theta_D$ and $\gamma$ values.

The electronic contribution to the specific heat, $C_e(T)$, was extracted by subtracting the phonon contribution, $C_{ph}(T) = C_{Ein}(T) + C_{Deb}(T)$, from the $C(T)$ data. Figure IV.8 displays semilogarithmic plots of $C_e/\gamma T_c$ versus $T_c/T$ for $PrPt_4Ge_{12}$ and $PrPt_4Ge_{11.5}Sb_{0.5}$. The fits to the data were performed in the range $1 \leq T_c/T \leq 2.5$. The red line in Fig. IV.8(a) demonstrates that $PrPt_4Ge_{12}$ is well described by $b(T_c/T)^n$, where $n \sim -2.5$, suggesting multiband superconductivity or nodes in the gap function in this compound [28]. The fit values for $b$

and $n$ are slightly different from the previous report [35], because different phonon contributions to the specific heat were subtracted. Figure IV.8(b) shows that the sample with $x = 0.5$ can be fit by an exponential temperature dependence, $ae^{-\Delta/T_c}$, where $a$ is a fitting parameter and $\Delta$ is the superconducting energy gap. The coefficient $a$ is around 5.3 and $\Delta/T_c$ is $\sim$1.3, which is somewhat smaller than the value of 1.76 from the BCS prediction of weak-coupled superconductivity. This change from power law to exponential temperature dependence is similar to behaviors observed in previous reports for the $Pr(Os_{1-x}Ru_x)_4Sb_{12}$ and $Pr_{1-x}Ce_xPt_4Ge_{12}$ systems [35, 50] and could be explained by a crossover in the structure of the superconducting energy gap from one containing point-nodes to one that is nodeless, or a suppression of one or more superconducting energy gaps in a multiband superconductor [28, 33, 34, 51].

## IV.D Discussion

Figure IV.9 summarizes results from $\rho(T)$, $\chi(T)$, $\chi''(T)$, and $C(T)$ measurements in a phase diagram of superconducting transition temperature $T_c$ versus nominal antimony concentration $x$. The $T_c$ values were taken from the onset of diamagnetic signals for the $\chi''(T)$ and $\chi(T)$ measurements. For the $C(T)$ measurements, $T_c$ was determined from the results of idealized entropy-conserving constructions [52, 53] (data not shown). This suppression of $T_c$ with $x$ is also consistent with the decrease of the upper critical field as shown in Fig. IV.4(b).

In order to understand the suppression of superconductivity, we need to consider the effects of Sb substitution in this system, including the increase of disorder, the increase in unit-cell volume, and the increase in electron concentration (electron doping). It has been reported that in Pt-Ge based skutterudite compounds, a large density of states (DOS) at the Fermi level is a common feature, and it is

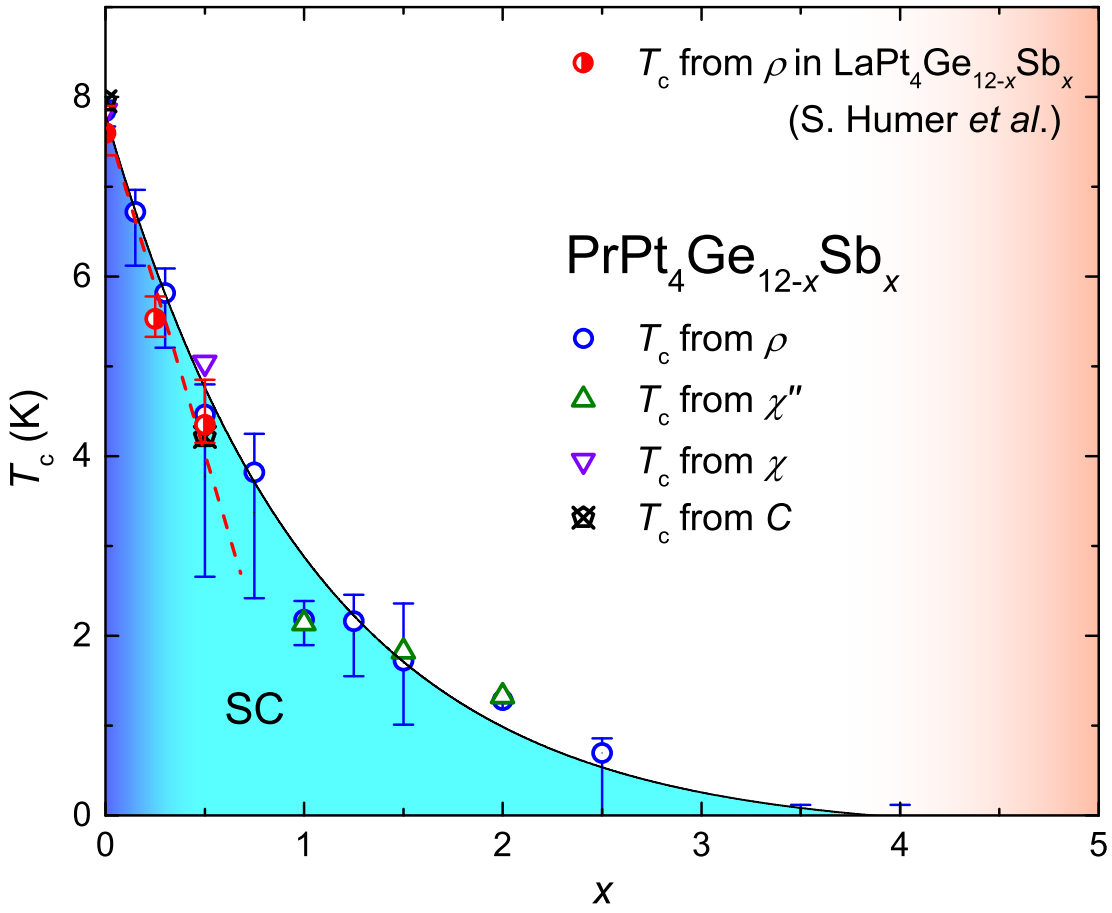


Figure IV.9: Phase diagram of the superconducting transition temperature $T_c$ as a function of Sb concentration $x$ based on electrical resistivity, AC and DC magnetic susceptibility, and specific heat measurements. The vertical bars for in the $T_c$ data represent the widths of the superconducting transitions and were derived from the $\rho(T)$ measurements as described in the text. $T_c$ is rapidly suppressed with $x$ up to $x \simeq 4$, and only the onset of superconductivity is observed for $x \geq 3.5$ in measurements performed down to $\sim 50$ mK. The gradient-filled area of the SC region under the $T_c$ versus $x$ curve indicates the change of the superconducting energy gap. The red dashed line shows the suppression of superconductivity observed in $LaPt_4Ge_{12-x}Sb_x$ [40].

believed to facilitate superconductivity [24, 26]. Moreover, soft x-ray valence-band photoemission spectroscopy on $PrPt_4Ge_{12}$ and $LaPt_4Ge_{12}$ display almost identical spectra, indicating that the electronic structures for both systems are very similar with one another [54]. Both have a similar $T_c$ near 8 K and exhibit evidence for multiband superconductivity; however, $PrPt_4Ge_{12}$ shows time-reversal symmetry breaking of the superconducting state [31]. Therefore, a comparison of the suppression of superconductivity and the effect of Sb substitution on these two different systems, $LaPt_4Ge_{12}$ and $PrPt_4Ge_{12}$, may provide new insights. Our careful comparison reveals that there are several similarities and one significant difference [40]. The increase in disorder results in a rapid decrease of RRR (see Fig. IV.2), indicating a correlation between disorder and the suppression of superconductivity for low $x$ concentrations, consistent with the result in $LaPt_4Ge_{12-x}Sb_x$. The unit-cell volume of superconducting Pt-Ge based skutterudites seems to be uncorrelated or very weakly correlated to their superconducting states, because the changes of $T_c$ upon applied pressure are small or non-monotonic; $T_c$ is probably more dependent on the electronic structure [55, 56]. Humer *et al.* discussed the decrease of the DOS and $\gamma$ values with Sb substitution, and its role in facilitating a rapid suppression of superconductivity [40]; a very similar decrease of $\gamma$ values for samples in the range $0 \leq x \leq 3$ is observed in this study .

The response of superconductivity to Sb substitution observed in this study contrasts with what was reported for $LaPt_4Ge_{12-x}Sb_x$. Even though there were no samples with Sb concentrations between $x = 0.5$ and 3 in the previous report on $LaPt_4Ge_{12-x}Sb_x$, no evidence of superconductivity was observed at $x = 3$ down to 0.4 K; moreover, a first principles calculation predicts that the system moves toward a metal-to insulator transition with higher Sb concentration. With these facts in mind, we conjecture that the suppression of superconductivity in $LaPt_4Ge_{12-x}Sb_x$ with $x$ could be faster than and/or different from that of

$PrPt_4Ge_{12-x}Sb_x$, as indicated by the red dashed line in Fig. IV.9. Similarly, a different suppression rate of $T_c$ is observed upon substitution of Ce ions into the La and Pr sites [57]. The observed differences in the suppression of $T_c$, therefore, could be explained by differing pairing mechanisms in these two systems; $PrPt_4Ge_{12}$ exhibits an unconventional type of superconductivity, while $LaPt_4Ge_{12}$ is a conventional BCS-type superconductor. However, there is evidence that $PrPt_4Ge_{12}$ has multiple isotropic BCS-type energy gaps, which cannot be ruled out from this study [32–34]. Also, the expected behavior associated with point nodes in specific heat measurements on polycrystalline samples is not supported by the results from a single crystal study: Polycrystalline specimens show a $T^3$ temperature dependence of the electronic specific heat, which has been attributed to a possible nuclear Schottky anomaly arising from Pr-containing surface contamination [34].

A rattling mode of the rare-earth ion has been observed in several filled skutterudite compounds [58, 59], especially in the $ROs_4Sb_{12}$ ($R$ = rare earth) family [60–62]. On the other hand, the Pt-Ge based skutterudites exhibit no strong evidence for off-center displacements of filler ions; thus, the DOS, composed of Ge-$p$ and Pt-5$d$ states, has more significant effects on various phenomena [30]. However, the introduction of Gd ions into the La site in $LaPt_4Ge_{12}$ provides an extra phonon mode with $\Theta_{\rm E} \sim 24$ K [63]. In this work, a weak "rattling" mode with a value of $\Theta_{\rm E} \sim 60$ K was estimated. In analogy with the behavior of Gd ions, the introduction of Sb ions into the Pt-Ge cage might produce additional phonon modes. The value of $\Theta_{\rm E}$ stays roughly constant throughout the entire range of $x$, suggesting that the rattling motion is independent of $x$; rattling in the $PrPt_4Ge_{12-x}Sb_x$ systems does not seem to have significant effects on either the superconducting state nor the localized $Pr^{+3}$ electronic configuration, consistent with the $x$-independent behavior of $\mu_{eff}/\mu_B$ as seen in Fig. IV.6(a).

We are currently unable to definitively address the relationships among the

Pr site occupancy, rattling dynamics, and the observed enhancement of electronic correlations for $x \geq 4$ samples. It has been reported that the partial filling of the Pr sites does not have a significant effect on the superconducting properties of $PrPt_4Ge_{12}$ [64]. A Pr Schottky anomaly could make it difficult to properly analyze the specific heat data [34], possibly leading to an artificial enhancement of $\gamma$. The presence of small concentrations of impurities could also potentially be responsible for an anomalous enhancement of the specific heat at low temperature for higher $x$ (see Fig. IV.7(a)). All of these factors complicate our ability to clearly determine the phenomena or phase that occurs in the gradient-filled region for $x \geq 4$ in Fig. IV.9. In order to have a better understanding of not only the features in the properties of samples with high Sb concentrations, but also the nature of superconductivity in $PrPt_4Ge_{12}$, future research such as neutron scattering, ultrasonic, or NMR-NQR measurements on high-quality single crystalline specimens will be necessary.

## IV.E Concluding Remarks

We have studied the superconducting and normal-state properties of $PrPt_4Ge_{12}$-based pseudoternary compounds in which Sb has been substituted for Ge. Polycrystalline samples of $PrPt_4Ge_{12-x}Sb_x$ with Sb concentrations up to $x = 5$ were investigated via x-ray diffraction, electrical resistivity, magnetic susceptibility, and specific heat measurements. We observed a suppression of superconductivity with increasing Sb substitution up to $x = 4$, above which, no signature of superconductivity was observed down to 140 mK. The electronic coefficient of specific heat $\gamma$ decreases with increasing Sb concentration in the superconducting region, indicating that the density of states might be an important parameter that facilitates superconductivity. The specific heat data for $x = 0.5$ exhibits an exponential temperature dependence in the superconducting state, suggesting a nodeless superconducting energy gap. A constant "rattling" mode of Pr ions with a value of $\Theta_E \sim 60$ K across the entire substitution range was suggested by Rietveld refinements of XRD data and fits of the Einstein model to specific heat data; however, it does not seem to be correlated with superconductivity in this system.

The text and data presented in this chapter are reprints of material that appears in "Investigation of superconducting and normal-state properties of the filled-skutterudite system $PrPt_4Ge_{12-x}Sb_x$," I. Jeon, K. Huang, D. Yazici, N. Kanchanavatee, B. D. White, P.-C. Ho, N. Pouse, and M. B. Maple, *Phys. Rev. B* **93**, 104507 (2016). The dissertation author is the primary investigator and author of this article.

## Bibliography


[1] W. Jeitschko and D. Braun, Acta Crystallogr. B **33**, 3401 (1977).

[2] I. Shirotani, T. Uchiumi, K. Ohno, C. Sekine, Y. Nakazawa, K. Kanoda, S. Todo, and T. Yagi, Phys. Rev. B **56**, 7866 (1997).

[3] B. C. Sales, in *Handbook on the Physics and Chemistry of Rare Earths*, edited by K. Gschneidner, J.-C. Bünzli, and V. Pecharsky (Elsevier, 2003), vol. 33, pp. 1 – 34.

[4] E. D. Bauer, N. A. Frederick, P.-C. Ho, V. S. Zapf, and M. B. Maple, Phys. Rev. B **65**, 100506 (2002).

[5] E. D. Bauer, A. Slebarski, E. J. Freeman, N. A. Frederick, B. J. Taylor, C. Sirvent, and M. B. Maple, Physica B **312-313**, 230 (2002).

[6] M. B. Maple, P.-C. Ho, V. S. Zapf, N. A. Frederick, E. D. Bauer, W. M. Yuhasz, F. M. Woodward, and J. W. Lynn, J. Phys. Soc. Jpn. **71**, 23 (2002).

[7] D. E. MacLaughlin, J. E. Sonier, R. H. Heffner, O. O. Bernal, B.-L. Young, M. S. Rose, G. D. Morris, E. D. Bauer, T. D. Do, and M. B. Maple, Phys. Rev. Lett. **89**, 157001 (2002).

[8] Y. Aoki, A. Tsuchiya, T. Kanayama, S. R. Saha, H. Sugawara, H. Sato, W. Higemoto, A. Koda, K. Ohishi, K. Nishiyama, and R. Kadono, Phys. Rev. Lett. **91**, 067003 (2003).

[9] R. Vollmer, A. Faißt, C. Pfleiderer, H. v. Löhneysen, E. D. Bauer, P.-C. Ho, V. Zapf, and M. B. Maple, Phys. Rev. Lett. **90**, 057001 (2003).

[10] H. Suderow, S. Vieira, J. D. Strand, S. Bud'ko, and P. C. Canfield, Phys. Rev. B **69**, 060504 (2004).

[11] M. B. Maple, N. A. Frederick, P.-C. Ho, W. M. Yuhasz, T. A. Sayles, N. P. Butch, J. R. Jeffries, and B. J. Taylor, Physica B **359-361**, 830 (2005).

[12] W. M. Yuhasz, N. P. Butch, T. A. Sayles, P.-C. Ho, J. R. Jeffries, T. Yanagisawa, N. A. Frederick, M. B. Maple, Z. Henkie, A. Pietraszko, S. K. McCall, M. W. McElfresh, and M. J. Fluss, Phys. Rev. B **73**, 144409 (2006).

[13] M. B. Maple, Z. Henkie, W. M. Yuhasz, P.-C. Ho, T. Yanagisawa, T. A. Sayles, N. P. Butch, J. R. Jeffries, and A. Pietraszko, J. Magn. Magn. Mater. **310**, 182 (2007).

[14] M. B. Maple, Z. Henkie, R. E. Baumbach, T. A. Sayles, N. P. Butch, P.-C. Ho, T. Yanagisawa, W. M. Yuhasz, R. Wawryk, T. Cichorek, and A. Pietraszko, J. Phys. Soc. Jpn. **77**, 7 (2008).

[15] H. Sato, Y. Aoki, D. Kikuchi, H. Sugawara, W. Higemoto, K. Ohishi, T. U. Ito, R. Heffner, S. R. Saha, A. Koda, K. H. Satoh, K. Nishiyama, R. Kadono, N. Nishida, L. Shu, and D. E. MacLaughlin, Physica B **404**, 749 (2009).

[16] L. Shu, D. E. MacLaughlin, W. P. Beyermann, R. H. Heffner, G. D. Morris, O. O. Bernal, F. D. Callaghan, J. E. Sonier, W. M. Yuhasz, N. A. Frederick, and M. B. Maple, Phys. Rev. B **79**, 174511 (2009).

[17] H. Sato, H. Sugawara, T. Namiki, S. R. Saha, S. Osaki, T. D. Matsuda, Y. Aoki, Y. Inada, H. Shishido, R. Settai, and Y. Onuki, J. Phys.: Condens. Matter **15**, S2063 (2003).

[18] N. P. Butch, W. M. Yuhasz, P.-C. Ho, J. R. Jeffries, N. A. Frederick, T. A. Sayles, X. G. Zheng, M. B. Maple, J. B. Betts, A. H. Lacerda, F. M. Woodward, J. W. Lynn, P. Rogl, and G. Giester, Phys. Rev. B **71**, 214417 (2005).

[19] Y. Aoki, T. Namiki, T. D. Matsuda, K. Abe, H. Sugawara, and H. Sato, Phys. Rev. B **65**, 064446 (2002).

[20] G. Seyfarth, J. P. Brison, M. A. Méasson, D. Braithwaite, G. Lapertot, and J. Flouquet, Phys. Rev. Lett. **97**, 236403 (2006).

[21] R. W. Hill, S. Li, M. B. Maple, and L. Taillefer, Phys. Rev. Lett. **101**, 237005 (2008).

[22] K. Izawa, Y. Nakajima, J. Goryo, Y. Matsuda, S. Osaki, H. Sugawara, H. Sato, P. Thalmeier, and K. Maki, Phys. Rev. Lett. **90**, 117001 (2003).

[23] E. E. M. Chia, M. B. Salamon, H. Sugawara, and H. Sato, Phys. Rev. Lett. **91**, 247003 (2003).

[24] E. Bauer, A. Grytsiv, X.-Q. Chen, N. Melnychenko-Koblyuk, G. Hilscher, H. Kaldarar, H. Michor, E. Royanian, G. Giester, M. Rotter, R. Podloucky, and P. Rogl, Phys. Rev. Lett. **99**, 217001 (2007).

[25] E. Bauer, X.-Q. Chen, P. Rogl, G. Hilscher, H. Michor, E. Royanian, R. Podloucky, G. Giester, O. Sologub, and A. P. Gonçalves, Phys. Rev. B **78**, 064516 (2008).

[26] R. Gumeniuk, W. Schnelle, H. Rosner, M. Nicklas, A. Leithe-Jasper, and Y. Grin, Phys. Rev. Lett. **100**, 017002 (2008).

[27] M. Toda, H. Sugawara, K. ichi Magishi, T. Saito, K. Koyama, Y. Aoki, and H. Sato, J. Phys. Soc. Jpn. **77**, 124702 (2008).

[28] A. Maisuradze, M. Nicklas, R. Gumeniuk, C. Baines, W. Schnelle, H. Rosner, A. Leithe-Jasper, Y. Grin, and R. Khasanov, Phys. Rev. Lett. **103**, 147002 (2009).

[29] F. Kanetake, H. Mukuda, Y. Kitaoka, H. Sugawara, K. Magishi, K. M. Itoh, and E. E. Haller, Physica C **470**, S703 (2010).

[30] R. Gumeniuk, H. Borrmann, A. Ormeci, H. Rosner, W. Schnelle, M. Nicklas, Y. Grin, and A. Leithe-Jasper, Z. Kristallogr. **225**, 531 (2010).

[31] A. Maisuradze, W. Schnelle, R. Khasanov, R. Gumeniuk, M. Nicklas, H. Rosner, A. Leithe-Jasper, Y. Grin, A. Amato, and P. Thalmeier, Phys. Rev. B **82**, 024524 (2010).

[32] L. S. S. Chandra, M. K. Chattopadhyay, and S. B. Roy, Phil. Mag. **92**, 3866 (2012).

[33] Y. Nakamura, H. Okazaki, R. Yoshida, T. Wakita, H. Takeya, K. Hirata, M. Hirai, Y. Muraoka, and T. Yokoya, Phys. Rev. B **86**, 014521 (2012).

[34] J. L. Zhang, Y. Chen, L. Jiao, R. Gumeniuk, M. Nicklas, Y. H. Chen, L. Yang, B. H. Fu, W. Schnelle, H. Rosner, A. Leithe-Jasper, Y. Grin, F. Steglich, and H. Q. Yuan, Phys. Rev. B **87**, 064502 (2013).

[35] K. Huang, L. Shu, I. K. Lum, B. D. White, M. Janoschek, D. Yazici, J. J. Hamlin, D. A. Zocco, P.-C. Ho, R. E. Baumbach, and M. B. Maple, Phys. Rev. B **89**, 035145 (2014).

[36] R. Gumeniuk, H. Rosner, W. Schnelle, M. Nicklas, A. Leithe-Jasper, and Y. Grin, Phys. Rev. B **78**, 052504 (2008).

[37] R. Gumeniuk, K. O. Kvashnina, W. Schnelle, M. Nicklas, H. Borrmann, H. Rosner, Y. Skourski, A. A. Tsirlin, A. Leithe-Jasper, and Y. Grin, J. Phys.: Condens. Matter **23**, 465601 (2011).

[38] M. Nicklas, S. Kirchner, R. Borth, R. Gumeniuk, W. Schnelle, H. Rosner, H. Borrmann, A. Leithe-Jasper, Y. Grin, and F. Steglich, Phys. Rev. Lett. **109**, 236405 (2012).

[39] B. D. White, K. Huang, and M. B. Maple, Phys. Rev. B **90**, 235104 (2014).

[40] S. Humer, E. Royanian, H. Michor, E. Bauer, A. Grytsiv, M. X. Chen, R. Podloucky, and P. Rogl, in *New Materials for Thermoelectric Applications: Theory and Experiment*, edited by V. Zlatic and A. Hewson (Springer Netherlands, 2013), NATO Science for Peace and Security Series B: Physics and Biophysics, pp. 115–127.

[41] A. C. Larson and R. B. V. Dreele, Los Alamos National Laboratory Report, 1994 (unpublished).

[42] B. Toby, J. Appl. Crystallogr. **34**, 210 (2001).

[43] E. Bauer, S. Berger, C. Paul, M. D. Mea, G. Hilscher, H. Michor, M. Reissner, W. Steiner, A. Grytsiv, P. Rogl, and E. W. Scheidt, Phys. Rev. B **66**, 214421 (2002).

[44] E. D. Bauer, A. Slebarski, N. A. Frederick, W. M. Yuhasz, M. B. Maple, D. Cao, F. Bridges, G. Giester, and P. Rogl, J. Phys.: Condens. Matter **16**, 5095 (2004).

[45] N. R. Werthamer, E. Helfand, and P. C. Hohenberg, Phys. Rev. **147**, 295 (1966).

[46] P.-C. Ho, T. Yanagisawa, N. P. Butch, W. M. Yuhasz, C. C. Robinson, A. A. Dooraghi, and M. B. Maple, Physica B **403**, 1038 (2008).

[47] H. G. Lukefahr, O. O. Bernal, D. E. MacLaughlin, C. L. Seaman, M. B. Maple, and B. Andraka, Phys. Rev. B **52**, 3038 (1995).

[48] B. C. Sales, B. C. Chakoumakos, D. Mandrus, J. W. Sharp, N. R. Dilley, and M. B. Maple, Mater. Res. Soc. Symp. Proc. **545** (1999).

[49] P.-C. Ho, W. M. Yuhasz, N. P. Butch, N. A. Frederick, T. A. Sayles, J. R. Jeffries, M. B. Maple, J. B. Betts, A. H. Lacerda, P. Rogl, and G. Giester, Phys. Rev. B **72**, 094410 (2005).

[50] N. A. Frederick, T. A. Sayles, S. K. Kim, and M. B. Maple, J. Low Temp. Phys. **147**, 321 (2007).

[51] M. Sigrist and K. Ueda, Rev. Mod. Phys. **63**, 239 (1991).

[52] E. Bonjour, R. Calemczuk, J. Y. Henry, and A. F. Khoder, Phys. Rev. B **43**, 106 (1991).

[53] S. B. Ota, V. S. Sastry, E. Gmelin, P. Murugaraj, and J. Maier, Phys. Rev. B **43**, 6147 (1991).

[54] Y. Nakamura, H. Okazaki, R. Yoshida, T. Wakita, M. Hirai, Y. Muraoka, H. Takeya, K. Hirata, H. Kumigashira, M. Oshima, and T. Yokoya, J. Phys. Soc. Jpn. **79**, 124701 (2010).

[55] R. T. Khan, E. Bauer, X.-Q. Chen, R. Podloucky, and P. Rogl, J. Phys. Soc. Jpn. **77**, 350 (2008).

[56] N. Foroozani, J. J. Hamlin, J. S. Schilling, R. E. Baumbach, I. K. Lum, L. Shu, K. Huang, and M. B. Maple, Physica C **485**, 160 (2013).

[57] K. Huang, D. Yazici, B. D. White, A. Breindel, N. Pouse, and M. B. Maple, (Unpublished).

[58] V. Keppens, D. Mandrus, B. C. Sales, B. C. Chakoumakos, P. Dai, R. Coldea, M. B. Maple, D. A. Gajewski, E. J. Freeman, and S. Bennington, Nature **395**, 876 (1998).

[59] Y. Nakai, K. Ishida, K. Magishi, H. Sugawara, D. Kikuchi, and H. Sato, J. Magn. Magn. Mater. **310**, 255 (2007).

[60] T. Yanagisawa, T. Mayama, H. Hidaka, H. Amitsuka, A. Yamaguchi, K. Araki, Y. Nemoto, T. Goto, N. Takeda, P.-C. Ho, and M. B. Maple, Physica B **404**, 3235 (2009).

[61] J.-i. Yamamura and Z. Hiroi, J. Phys. Soc. Jpn. **80**, 054601 (2011).

[62] T. Keiber, F. Bridges, R. E. Baumbach, and M. B. Maple, Phys. Rev. B **86**, 174106 (2012).

[63] F. A. Garcia, R. Gumeniuk, W. Schnelle, J. Sichelschmidt, A. Leithe-Jasper, Y. Grin, and F. Steglich, Phys. Rev. B **85**, 134402 (2012).

[64] D. Venkateshwarlu, S. S. Samatham, M. Gangrade, and V. Ganesan, J. Phys.: Conf. Ser. **534**, 012040 (2014).

# Chapter V

# Crossover and coexistence of superconductivity and antiferromagnetism in the filled-skutterudite system $Pr_{1-x}Eu_xPt_4Ge_{12}$

## V.A Introduction

A new class of filled-skutterudite compounds with the chemical formula $MPt_4Ge_{12}$ ($M$ = alkali metal, alkaline earth, lanthanide, or actinide) has recently been reported [1–7]. These new Pt-Ge based skutterudite systems exhibit various strongly correlated electron phenomena. The compound $PrPt_4Ge_{12}$ is especially interesting since it is an unconventional superconductor that has properties similar to those of $PrOs_4Sb_{12}$: point nodes in the superconducting energy gap indicated by transverse muon spin relaxation ($\mu$SR) and specific heat measurements,

evidence for time-reversal symmetry breaking (TRSB) from zero-field $\mu$SR measurements [5, 8], and multiband unconventional superconductivity (SC) suggested from previous reports [9–11]. Several chemical substitution studies based on specific heat measurements reveal a suppression of superconductivity in $PrPt_4Ge_{12}$, accompanied by a crossover from a nodal to a nodeless superconducting energy gap or the suppression of multiple superconducting energy bands with increasing substituent composition [12–14].

Unconventional SC seems to be correlated with magnetism. The interplay between these two phenomena often leads to rich and intriguing physics with complex temperature $T$ versus substituent composition or applied pressure phase diagrams, including pseudogaps, structural phase transitions, non-Fermi-liquid (NFL) behavior, or quantum criticality. In many Fe-pnictide and cuprate compounds, the interplay between unconventional SC and antiferromagnetic (AFM) order is manifested in generic phase diagrams, in which the unconventional SC appears to emerge in a dome shaped region near the composition or pressure where the antiferromagnetic order has been suppressed towards 0 K [15, 16]. The filled-skutterudite system $Pr_{1-x}Nd_xOs_4Sb_{12}$ shows the effect of magnetic moments on the normal and SC states of $PrOs_4Sb_{12}$, suggesting superconductivity and magnetism coexist within the superconducting state [17, 18]. However, such an interplay between magnetism and unconventional SC in $PrPt_4Ge_{12}$ has not yet been reported, to the best of our knowledge.

In the end member compound $EuPt_4Ge_{12}$, the Eu ion is divalent and the electronic configuration is the same as $Gd^{3+}$ ion, $J = S = 7/2$. The compound $EuPt_4Ge_{12}$ orders antiferromagnetically with a Néel temperature, $T_N \sim 1.7$ K with an effective magnetic moment, $\mu_{eff} \sim 7.4\ \mu_B$ and a Curie-Weiss temperature, $\Theta_{CW} \sim -11$ K [19]. The value of $T_N$ for $EuPt_4Ge_{12}$ is fairly low compared to other Eu-based filled-skutterudite compounds with the $Eu^{2+}$ electronic configuration.

For example, the compounds $EuFe_4X_{12}$ ($X$ = Sb, As) are ferromagnetic with Curie temperatures, $T_c \sim 88$ K and $\sim 152$ K, respectively, where the enhanced $T_c$ has been attributed to the existence of a small magnetic moment ($\sim 0.21\ \mu_B$ for the Fe-Sb cage) on the Fe ion [20, 21]. The low $T_N$ value for $EuPt_4Ge_{12}$ is possibly due to absence of a magnetic moment on Pt in the Pt-Ge cage, leading to a decrease of the Ruderman-Kittel-Kasuya-Yosida (RKKY) interaction between the $Eu^{2+}$ localized magnetic moment and the conduction electron spins [19, 22]. This is seen in previous reports for the compounds $EuRu_4X_{12}$ with non-magnetic Ru-$X$ cages (ferromagnetic transition temperature, $T_m \sim 3.3$ K for $X$ = Sb and no magnetic anomaly down to 2 K for $X$ = As) [20, 21, 23]. In addition, $EuPt_4Ge_{12}$ has a large Sommerfeld coefficient, $\gamma \sim 220$ mJ/mol K, which has been attributed to $Eu^{2+}$ spin fluctuations [19, 24].

In this paper, we report a study of the $Pr_{1-x}Eu_xPt_4Ge_{12}$ system. The evolution of superconducting and magnetic properties with increasing Eu concentration, $x$, was studied by means of x-ray diffraction, electrical resistivity, magnetic susceptibility, and specific heat measurements. We observed a crossover from SC to AFM and a suppression of SC with negative curvature as a function of $x$, and a Eu concentration range within which the two phases coexist. Our results from specific heat measurements are similar to those of previous studies ($Pr_{1-x}Ce_xPt_4Ge_{12}$ and $PrPt_4Ge_{12-x}Sb_x$), suggesting a possible crossover from a nodal to a nodeless superconducting energy gap or from multiple energy gaps to a single BCS-type superconducting energy gap [9–14]; however, the crossover in the present case is much slower. In the normal state, we observed a crossover from Fermi-liquid (FL) to non-Fermi-liquid (NFL) behavior in the Eu rich region, suggesting the intrinsic electronic structure is correlated to SC, AFM, and other possible complex physical phenomena in this system.

## V.B Experimental Details

Polycrystalline samples of $Pr_{1-x}Eu_xPt_4Ge_{12}$ were synthesized by arc-melting on a water-cooled copper hearth under an Ar atmosphere with a Zr getter and then annealed. The starting materials were Pr ingots (Alfa Aesar 99.9%), Eu ingots (Alfa Aesar 99.9%), Pt sponge (Engelhard 99.95%), and Ge pieces (Alfa Aesar 99.9999+%). The detailed procedures used to prepare the samples are reported elsewhere [13]. The crystal structure was determined by x-ray powder diffraction (XRD) using a Bruker D8 Discover x-ray diffractometer with Cu-$K_\alpha$ radiation, and XRD patterns were analyzed via Rietveld refinement using the GSAS+EXPGUI software package [25, 26]. The electrical resistivity was measured from 1.1 K to 300 K using a standard four-wire method with a Linear Research LR700 AC resistance bridge in a home-built probe in a liquid $^4$He Dewar, and down to $\sim$ 100 mK (data below 0.35 K were rejected due to noise) using a commercial $^3$He-$^4$He dilution refrigerator. Magnetic susceptibility measurements were made between 2 K and 300 K in magnetic fields up to 7 T using a Quantum Design Magnetic Property Measurement System (MPMS). Specific heat measurements were performed at temperatures down to 1.8 K with a Quantum Design Physical Property Measurement System (PPMS) DynaCool and down to 0.5 K with the $^3$He option for the PPMS DynaCool.

## V.C Results

### V.C.1 X-ray diffraction

Figure V.1 shows results from XRD data for the $Pr_{1-x}Eu_xPt_4Ge_{12}$ ($0 \leq x \leq 1$) system. All of the XRD patterns are well indexed with the cubic filled-skutterudite crystal structure with space group $Im\bar{3}$. Figure V.1 displays a representative XRD pattern of the $Pr_{0.5}Eu_{0.5}Pt_4Ge_{12}$ compound and the best fit from

the Rietveld refinement. The dashed arrows indicate the contents of small impurity phases of Ge and/or $PtGe_2$ (at most up to $\sim 5\%$ by molar mass ratio), as is commonly observed in the Pt-Ge based skutterudites [3, 4, 7, 9, 11, 13, 27, 28]. Since Eu ions are divalent in the end member compound $EuPt_4Ge_{12}$ [19, 24], and the atomic radius of $Eu^{2+}$ ions is larger than that of the $Pr^{3+}$ ions, the lattice parameter $a$ exhibits a linear increase throughout the entire range of $x$, as shown in the inset of Fig. V.1; however, there are discrepancies in the $a$ values for $EuPt_4Ge_{12}$ between previous reports and our study, which is possibly due to a known sample dependence in the Pt-Ge based filled skutterudites; reported values of $a$ for $EuPt_4Ge_{12}$ differ by roughly 0.5% [3, 28].

### V.C.2 Electrical Resistivity

The results of electrical resistivity, $\rho(T)$, measurements are shown in Fig. V.2. All samples exhibit metallic behavior in their normal states, as seen in Fig. V.2(a); we show some representative concentrations for visual clarity. The residual resistivity ratio, RRR ($\rho_{300}/\rho_0$), versus $x$ is shown in the inset of Fig. V.2(a), where $\rho_{300}$ is the room temperature resistivity and $\rho_0$ is the resistivity value right above the SC/AFM transitions. The RRR($x$) exhibits a parabolic shape with the minimum around $x = 0.5$, consistent with the expected minimum for simple alloys. Figure V.2(b) displays $\rho(T)$ normalized to its value at 10 K versus $x$. The $T_c$ value was defined as the temperature where the value of $\rho(T)/\rho_{10}$ drops to 0.5, and the width of the transition was determined by the temperatures where $\rho(T)/\rho_{10}$ is 0.9 and 0.1. A monotonic decrease of $T_c$ is observed to $x = 0.5$, with slightly broadened transitions for $x > 0.3$. We also performed $\rho(T)$ measurements down to 0.35 K on the selected samples with $x = 0.6$, 0.8, and 0.9; however, there was no sign of SC. In Fig. V.2(c), $\rho(T)$ data for Eu rich compounds, shown with vertical translations for visual clarity, exhibit kinks associated with AFM transitions [19]. The Néel

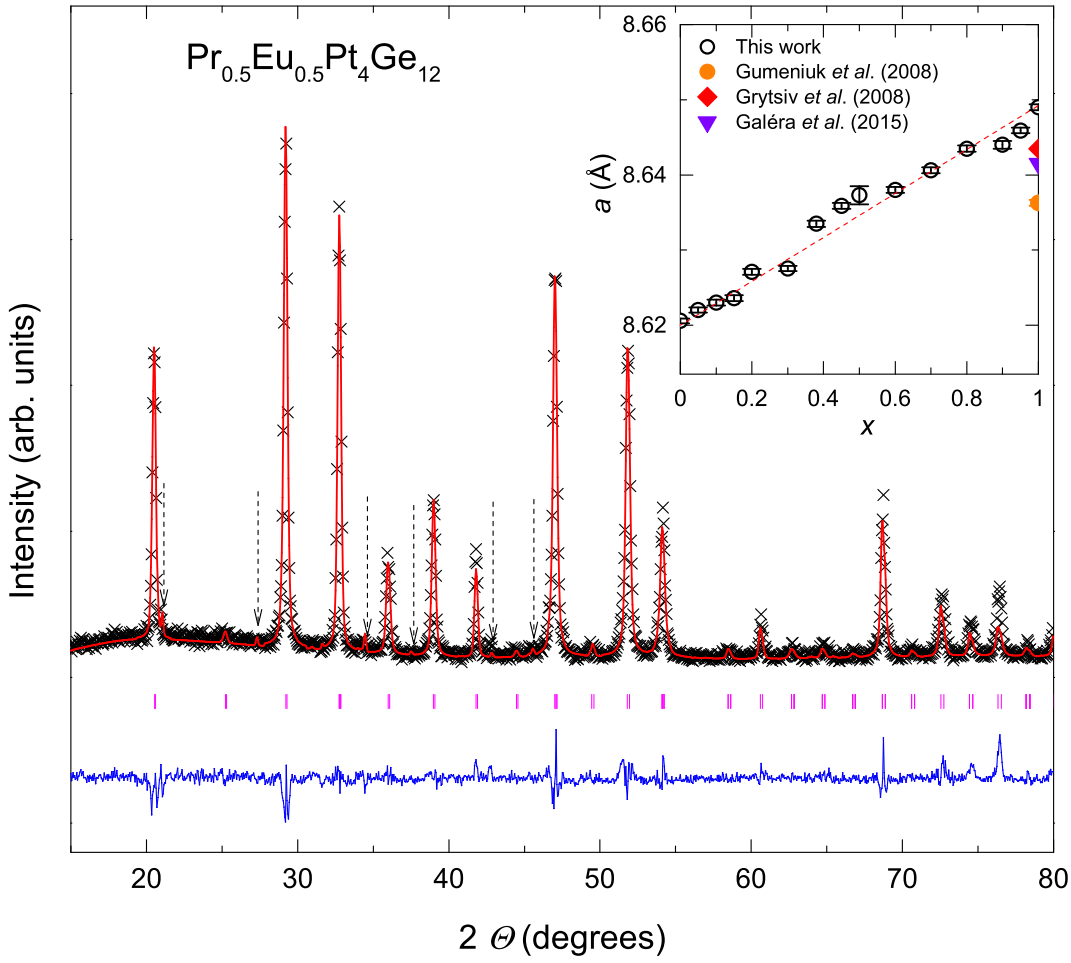


Figure V.1: X-ray diffraction pattern for $Pr_{0.5}Eu_{0.5}Pt_4Ge_{12}$. The black crosses represent the experimental data and the red line represents the fit from the Rietveld refinement of the data. The magenta vertical marks indicate the position of expected Bragg reflections and the blue line at the bottom is the difference between observed and calculated intensities. The dashed arrows indicate Bragg reflections associated with a Ge or $PtGe_2$ impurity phase. The inset shows a plot of the lattice parameter $a$ versus nominal Eu concentration $x$. The red dashed line is a guide to the eye.

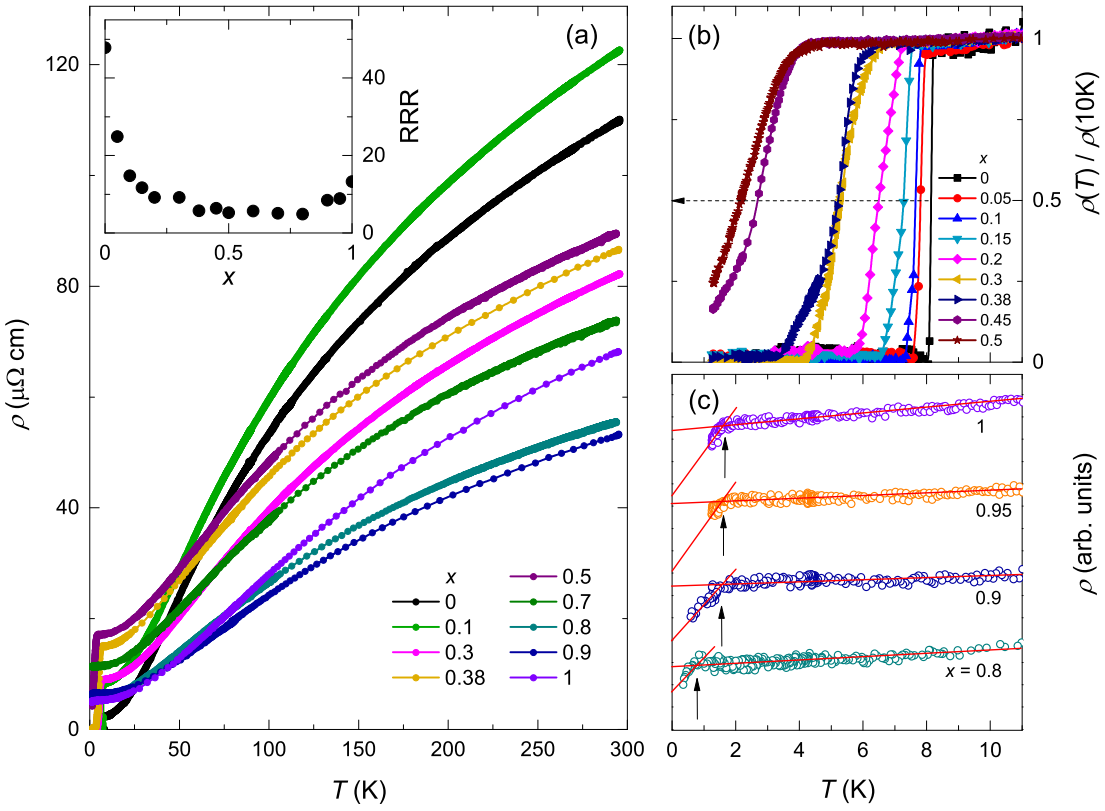


Figure V.2: (a) Electrical resistivity data $\rho$ versus $T$ for selected $Pr_{1-x}Eu_xPt_4Ge_{12}$ samples. Displayed in the inset is a plot of the residual resistivity ratio RRR versus $x$ for $Pr_{1-x}Eu_xPt_4Ge_{12}$. The RRR shows a parabolic shape with the minimum at $x = 0.5$. (b) $\rho(T)$, normalized to its value at 10 K, versus $x$ for superconducting $Pr_{1-x}Eu_xPt_4Ge_{12}$ samples. The superconducting transition temperature, $T_c$, decreases with increasing $x$. The dashed arrow is a guide to the eye. (c) $\rho(T)$ versus $x$ with offsets for Eu rich compounds exhibiting kinks associated with an antiferromagnetic transition, indicated by solid arrows. The Néel temperature, $T_N$, decreases slowly from $x = 1$ to 0.8.

temperature, $T_{\rm N}$, decreases from $\sim$ 1.7 K for $x = 1$ to $\sim$ 0.8 K for $x = 0.8$; we did not observe any clear feature associated with the AFM transitions for samples with $x < 0.8$, down to 0.35 K.

Fig. V.3(a) shows a log-log plot of $\rho - \rho_0$ versus $T$ with vertical translations for visual clarity. The red solid lines represent least squares fits to the data with the formula:

$$\log(\rho(T) - \rho_0) = \log(A_n) + n\log(T), \tag{V.1}$$

in the temperature range from just above $T_{\rm c}$ or $T_{\rm N}$ to $\sim$ 15 K. Interestingly, a gradual change of $n$ values was observed throughout the entire substitution range from $n \sim 5$ at $x = 0$ to $n \sim 1$ at $x = 1$. For Pr rich samples, they are consistent with the Bloch-Grüneisen behavior, since they have rather large $n$ values from $\sim$ 4 to $\sim$ 5 as seen in Fig. V.2 (a). The negative curvature of $\rho(T)$ at elevated temperatures is indicative of a narrow feature in the electronic density of states at the Fermi level [29]. For $EuPt_4Ge_{12}$, it has been reported that evidence of a FL ground state, a $T^2$ dependence of $\rho(T)$, is not recovered even under applied magnetic field at 12 T [19], suggesting that system may show a crossover from a FL to a NFL ground state. For $x > 0.5$, we observe kinks in Fig. V.3 (a), where the slopes, $n$, change. As shown in Fig. V.3 (b), the value of $n$ decreases from $\sim$ 5 to 1, suggesting a type of crossover from FL to NFL behavior with decreasing temperature; this result may indicate that magnetic fluctuations associated with Eu ions in the $EuPt_4Ge_{12}$ [19] become even weaker with increasing Pr substitution. The corresponding fitting parameters $A_n$ and $\rho_0$ versus $x$ are shown in Fig. V.3 (c) and (d), respectively. The coefficient, $A_n$, increases monotonically while the residual resistivity, $\rho_0$, has a parabolic shape with a maximum at $x \sim 0.5$. The scatter in the values of $A_n(x)$ and $\rho_0(x)$ are probably due to uncertainties in the measurement of the geometrical factors of the resistivity samples.

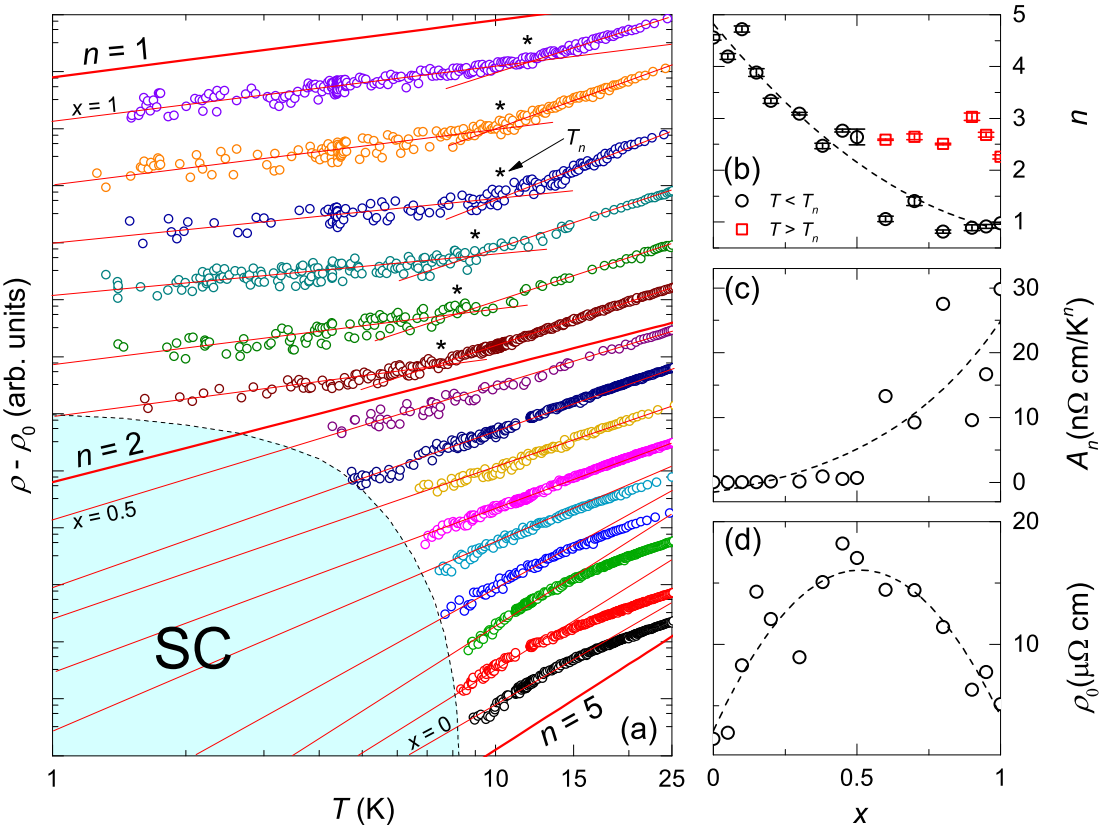


Figure V.3: (a) A double logarithmic plot of $\rho - \rho_0$ versus $T$ for $Pr_{1-x}Eu_xPt_4Ge_{12}$ with vertical translations for visual clarity. Linear fits of Eq. V.1 were made to data up to $T \sim 15$ K, indicated by the red solid lines. The gradual change of $n$ from $\sim 5$ at $x = 0$ to $\sim 1$ at $x = 1$ was observed. The thicker solid lines are for reference, with different $n$ values ($n = 1$, 2, and 5, respectively). The black asterisks point out the temperatures where the value of $n$ changes for Eu rich compounds. The light blue filled area denotes the SC region. The corresponding fitting parameters $n$ and $A$, and residual resistivity $\rho_0$, versus $x$ are shown in (b), (c), and (d), respectively.

### V.C.3 Magnetic Susceptibility

Magnetization divided by applied magnetic field, $M/H$, versus $T$ data are displayed in Fig. V.4 (a). Measurements were made under an applied magnetic field of $H = 0.1$ T. The overall magnitude of $M/H$ increases with increasing $x$, becoming more temperature dependent. Figure V.4(b) shows superconducting transitions for $0 \leq x \leq 0.45$ in an applied magnetic field $H = 10$ Oe. We defined $T_c$ as the temperature where zero-field-cooled (ZFC) and field-cooled (FC) data start to deviate from one another. The superconducting volume fractions were estimated from the ZFC $M(T)/H$ data by using the relation $4\pi d \times M/H$ ($\equiv 4\pi\chi_{\rm vol}$), where $d$ is the molar density of the samples in units of mol/cm$^3$. The values of the volume fractions, $4\pi\chi_{\rm vol}$, scatter around 1, which results from the uncertainties in determining demagnetization factors for this analysis. We fit the $M(T)/H$ data to a Curie-Weiss law in the temperature ranges from 75 to 300 K for $0 \leq x \leq 0.2$ due to the observed broad maxima near 75 K for $PrPt_4Ge_{12}$ [4, 12, 13] and from possible lowest temperatures to 300 K for the rest of samples

$$M/H = C_0/(T - \Theta_{\rm CW}), \tag{V.2}$$

where $C_0$ is the Curie constant and $\Theta_{\rm CW}$ is the Curie-Weiss temperature. The average effective magnetic moment, $\mu_{\rm eff}$, of the Eu and Pr mixture is estimated using the relation $C_0 = \mu_{\rm eff}^2 N_{\rm A}/3k_{\rm B}$, where $N_{\rm A}$ is Avogadro's number and $k_{\rm B}$ is Boltzmann's constant. The best fit values are shown in Fig. V.4 (c) and (d). Values of $\mu_{\rm eff}(x)$ increase from $\sim 3.64\ \mu_{\rm B}$ to $\sim 7.9\ \mu_{\rm B}$. The data are consistent with the calculated values, indicated by the red line in Fig. V.4 (b), using the relation:

$$\mu_{\rm eff}(x) = \sqrt{(\mu_{\rm Pr^{3+}})^2(1-x) + (\mu_{\rm Eu^{2+}})^2(x)}, \tag{V.3}$$

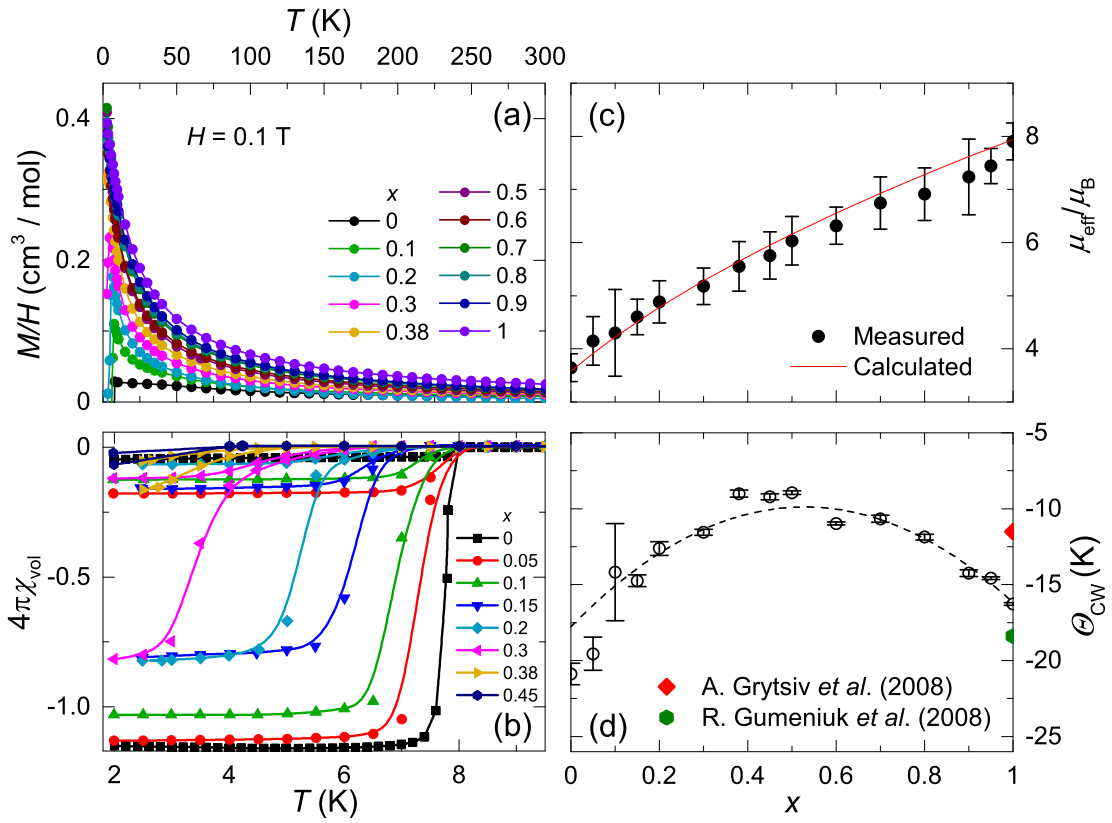


Figure V.4: (a) A plot of magnetization divided by applied magnetic field, $M/H$, versus temperature $T$, measured in an applied magnetic field $H = 0.1$ T for selected samples of $Pr_{1-x}Eu_xPt_4Ge_{12}$ for visual clarity. (b) The Meissner and diamagnetic shielding fractions $4\pi\chi_{\rm vol}$ versus $T$ for superconducting samples. The diamagnetic shielding fractions are close to 1. The deviations from unity are probably due to uncertainties in estimating the demagnetization factor. (c) Effective magnetic moment, obtained from the fit, $(\mu_{\rm eff}/\mu_{\rm B})$ versus $x$; the value of $\mu_{\rm eff}(x)/\mu_{\rm B}$ increases from $\mu_{\rm eff} \sim 3.64\ \mu_{\rm B}$ at $x = 0$ to $\mu_{\rm eff} \sim 7.9\ \mu_{\rm B}$ at $x = 1$. The red line is determined from a calculation using Eq. V.3. (d) Curie-Weiss temperature $\Theta_{\rm CW}$ versus $x$. As $x$ is increased, $\Theta_{\rm CW}$ first increases to $x \sim 0.5$ and then decreases to $x = 1$. The dashed lines are guides to the eye.

where the free ion values of $\mu_{Pr^{3+}}$ and $\mu_{Eu^{+2}}$ are 3.58 $\mu_B$ and 7.94 $\mu_B$, respectively. This result indicates that the spin configuration of the $Eu^{2+}$ ion is stable in our alloy system, as would be expected for $Gd^{3+}$ substitution in $PrPt_4Ge_{12}$.

The dependence of the Curie-Weiss temperature, $\Theta_{CW}$, on $x$ has a parabolic shape with a maximum around $x \sim 0.5$, as shown in Fig. V.4 (d). Note that for $PrPt_4Ge_{12}$, there is evidence of crystalline electric field (CEF) splitting of the Hund's rule ground state multiplet with a $\Gamma_4^{(1)}$ triplet as the first excited state [4], while there are no CEF effects in $EuPt_4Ge_{12}$ since $Eu^{2+}$ is an S-state ion [19]. The systematic substitution of Eu for Pr could be a reason for the decrease in magnitude of the $\Theta_{CW}$ up to $x \sim 0.5$, possibly due to the dilution of CEF effects. The increase in magnitude of $\Theta_{CW}$ for $x \geq 0.5$ is probably due to the AFM order.

### V.C.4 Specific Heat

Specific heat, $C$, versus $T$ data are shown in Fig. V.5(a) and (b) for selected samples for the sake of visual clarity. Anomalies associated with the onset of SC were observed in samples with $x < 0.45$. Since Néel temperatures, $T_N$, are below 1.8 K in the resistivity data, we performed low-temperature specific heat measurements on samples with $x = 0.95$, 0.9, 0.8, 0.7, 0.5, 0.38, and 0.3, down to 0.5 K. In Fig. V.5(c), the values of $T_N$ (indicated by red arrows) are suppressed with increasing Pr content until $x \sim 0.38$. These results are consistent with those from the resistivity data. A previous study on $EuPt_4Ge_{12}$ by Nicklas *et al.* [24] reported that $EuPt_4Ge_{12}$ exhibits complex magnetic order at low temperature (indicated by black arrows in Fig. V.5 (c)). It seems these additional transitions are suppressed with increasing Pr concentration for $x = 0.95$, 0.9, 0.8, and 0.7 at least; however, further investigations are needed, since the nature of this complex magnetic order has not yet been clarified.

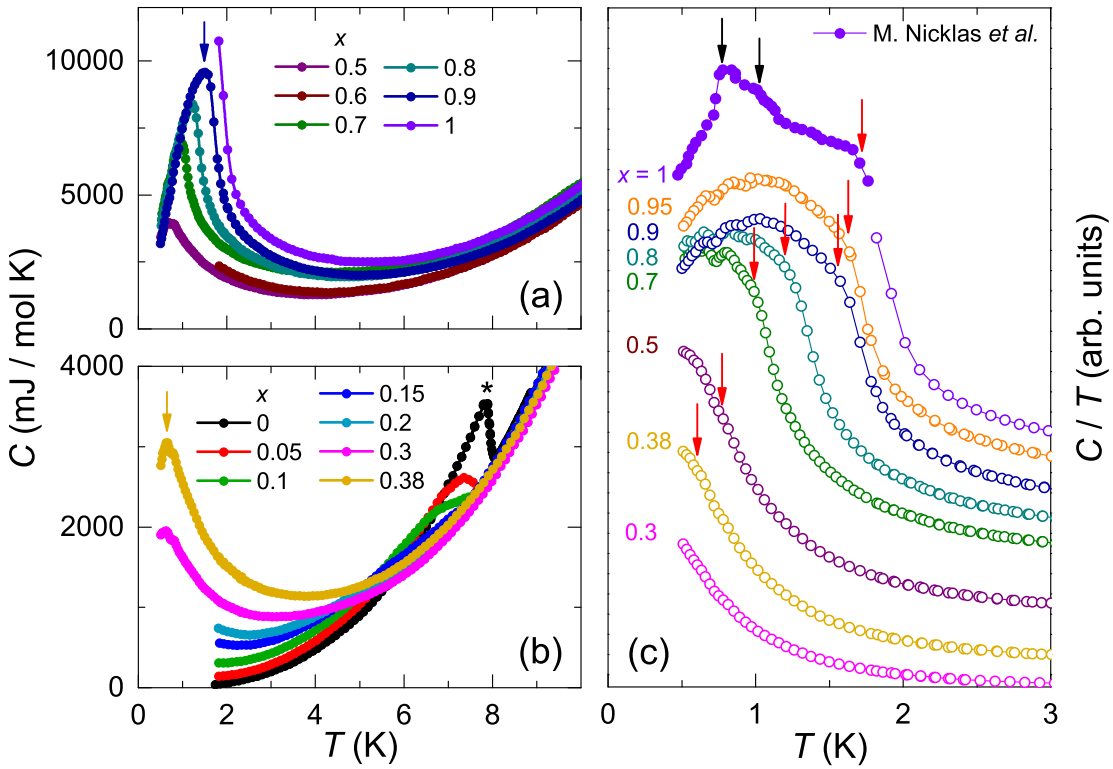


Figure V.5: (a) and (b) Specific heat $C$ versus temperature $T$ for $Pr_{1-x}Eu_xPt_4Ge_{12}$. Arrows indicate features associated with AFM transitions and the black asterisk locates the SC anomaly. (c) $C/T$ versus $T$ data at low temperatures for Eu rich compounds. The Néel temperature, $T_N$ are suppressed with increasing Pr content, as indicated by red arrows. The multiple magnetic transitions (black arrows) defined by M. Nicklas *et al*. [30] are shown as a reference.

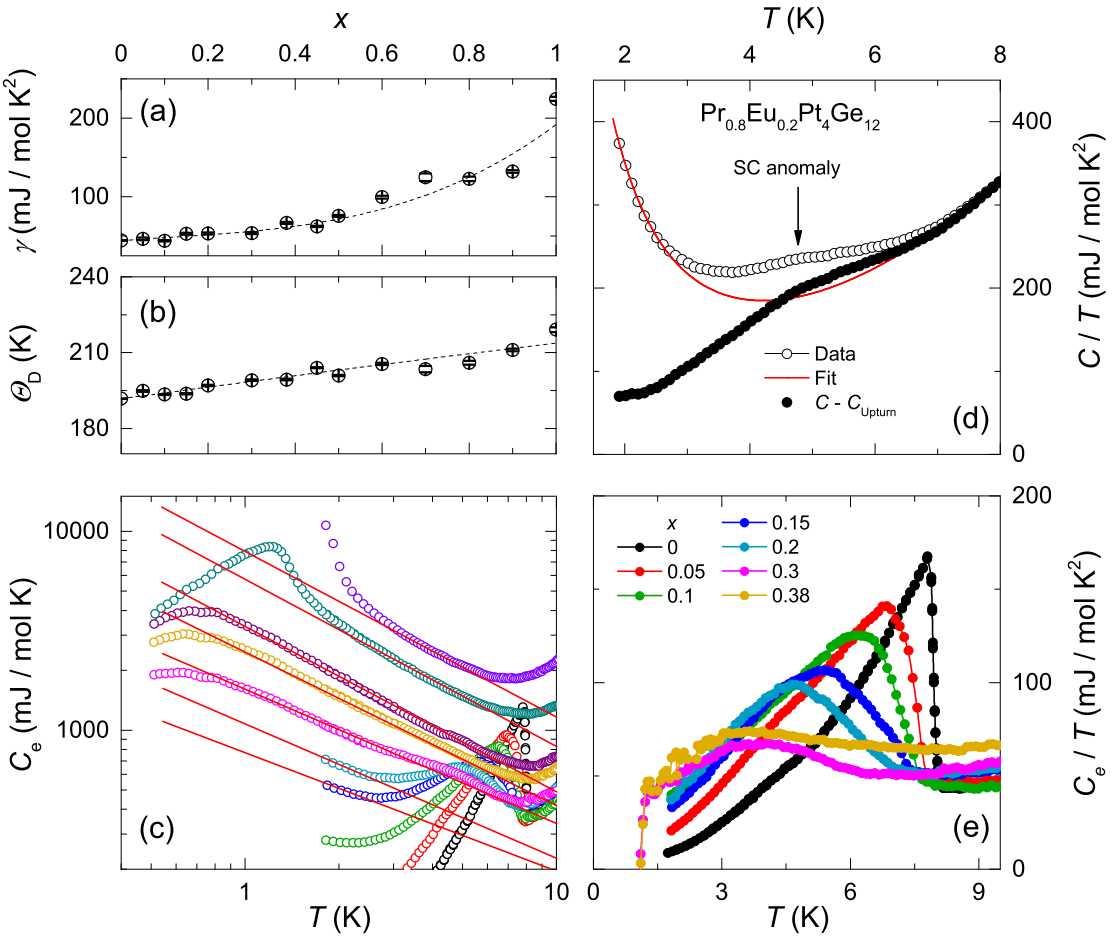


Figure V.6: (a) and (b) Plots of the electronic specific heat cofficient, $\gamma$, and Debye temperature $\Theta_{\rm D}$, versus $x$. The values were obtained from linear fits of Eq. V.4 to the data. The $\gamma$ values first increase slowly to $x = 0.5$ then increase faster to $x = 1$ (see text), while the values of $\Theta_{\rm D}$ show a moderate increase with increasing $x$. Dashed lines are guides to the eye. (c) A systematic increase of the upturn in $C(T)$ at low temperature is displayed as a log-log plot of the electronic specific heat contribution, $C_{\rm e}$ versus $T$. Red lines are guides to the eye. (d) A procedure for subtraction of the upturn in $C(T)$ is displayed in a plot of $C/T$ versus $T$ for the superconducting $Pr_{0.8}Eu_{0.2}Pt_4Ge_{12}$ compound. Open circles are raw data, the red line is the fit, using Eq. V.5, and the solid circles are the $C(T)$ data after subtraction of the upturn. (e) Plots of $C_{\rm e}$ versus $T$ showing SC anomalies for $x < 0.45$ after subtraction of the low temperature upturn in $C(T)$ for each sample.

The coefficients of the electronic and lattice contributions to the specific heat, $\gamma$ and $\beta$, respectively, were determined using linear fits:

$$C(T)/T = \gamma + \beta T^2, \tag{V.4}$$

in the range from the lowest non-ordered temperature to $\sim$ 250 K$^2$ (data not shown). In Fig. V.6 (a), the $\gamma$ values first increase from $\sim$ 45 mJ/mol K$^2$ at $x = 0$ to $\sim$ 76 mJ/mol K$^2$ at $x = 0.5$ in the SC region and then increase more rapidly up to $\sim$ 224 mJ/mol K$^2$ at $x = 1$ in the Eu rich region. Such different rates of increase in the $\gamma$ values suggest that stronger electronic correlations or $Eu^{2+}$ spin fluctuations, as reflected in the AFM nature of $EuPt_4Ge_{12}$ [19, 22], are more clearly manifested in the Eu rich region. The value we obtained for $\gamma$ of $PrPt_4Ge_{12}$ deviates from the values reported in other studies; however this could be due to the different methods employed for determining $\gamma$ values [3, 5, 11, 13, 14]. Even though the $\gamma$ value for $x = 1$ is about half of $\gamma \sim 500$ mJ/mol K$^2$ for $PrOs_4Sb_{12}$ [31, 32], it is still a fairly large enhancement of $\gamma$; further research on $EuPt_4Ge_{12}$ would be of interest. The Debye temperature, $\Theta_{\rm D}$, was obtained using the relation: $\Theta_{\rm D} = [1944 \times (n_{\rm f.u.}/\beta)]^{1/3}$ K, where $n_{\rm f.u.} = 17$, the number of atoms in the formula unit. As seen in Fig. V.6 (b), $\Theta_{\rm D}$ shows a small increase with increasing $x$.

Since the systematic upturns in the specific heat at low temperature (see Fig. V.5(b)) are simultaneously present with SC anomalies, our ability to determine the exact $T_{\rm c}$ values is compromised. The electronic contribution to the specific heat, $C_{\rm e}(T)$, was obtained by subtracting the phonon contribution, $C_{\rm ph}(T) = \beta T^3$, from the $C(T)$ data. A log-log plot of $C_{\rm e}$ versus $T$ in Fig. V.6 (c) shows the upturns in $C(T)$ have a power-law type divergence; the values of the slopes scatter around $\sim -1$. We, therefore, subtracted this upturn in $C(T)$ from the data, using the

relation:

$$C(T) = \gamma T + \beta T^3 + pT^{-q}, \tag{V.5}$$

where $p$ and $q$ are the fitting parameters. First, we fixed the $\gamma$ and $\beta$ values obtained from linear fits using Eq. V.4 and performed least-squares fits of Eq. V.5 to data, in order to determine $p$ and $q$ values and subtract only the upturn from the data. An example for $Pr_{0.8}Eu_{0.2}Pt_4Ge_{12}$ is displayed in Fig. V.6 (d). The fitting parameter $q$ scattered between $\sim 0.8$ and $\sim 1.1$, consistent with the observation in Fig. V.6(c). The SC anomalies after subtraction of the upturns are shown as a plot of $C_e/T$ versus $T$ in Fig. V.6 (e), showing a systematic decrease of $T_c$, consistent with results obtained from resistivity and magnetization data. However, we did not observe clear features of SC for the $x = 0.45$ and 0.5 samples, possibly due to broad superconducting transitions and low $T_c$ values.

Fig. V.7 displays semilogarithmic plots of $C_e/\gamma T_c$ versus $T_c/T$ for $Pr_{1-x}Eu_xPt_4Ge_{12}$ up to $x = 0.3$. The fits to the data were performed in the range $1 \leq T_c/T \leq T_c/T_{min}$, where $T_{min}$ is the lowest temperature available in the data. The red lines in Fig. V.7 (a,b,c) show that the compounds with $x \leq 0.1$ are best described by the power-law formula $b(T_c/T)^{-m}$, where $b$ and $m$ are the fitting parameters, whose values are listed in Fig. V.7. This power-law temperature-dependence suggests multiband superconductivity or nodes in the gap function in these compounds [5]. In the case of nodes in the gap structure, it is intriguing to note that such a change in $m$ values from $\sim 3$ to $\sim 2$ may suggest that the gap structure evolves from point-like to line nodes [33]. In Fig. V.7 (d,e,f), the blue lines are the fits of an exponential temperature dependence, $ae^{-\Delta/T_c}$, where $a$ is a fitting parameter and $\Delta$ is the SC energy gap; these values are listed in Fig. V.7 (d,e,f). These results suggest that the compounds with $x \geq 0.15$ exhibit single-band isotropic s-wave SC.

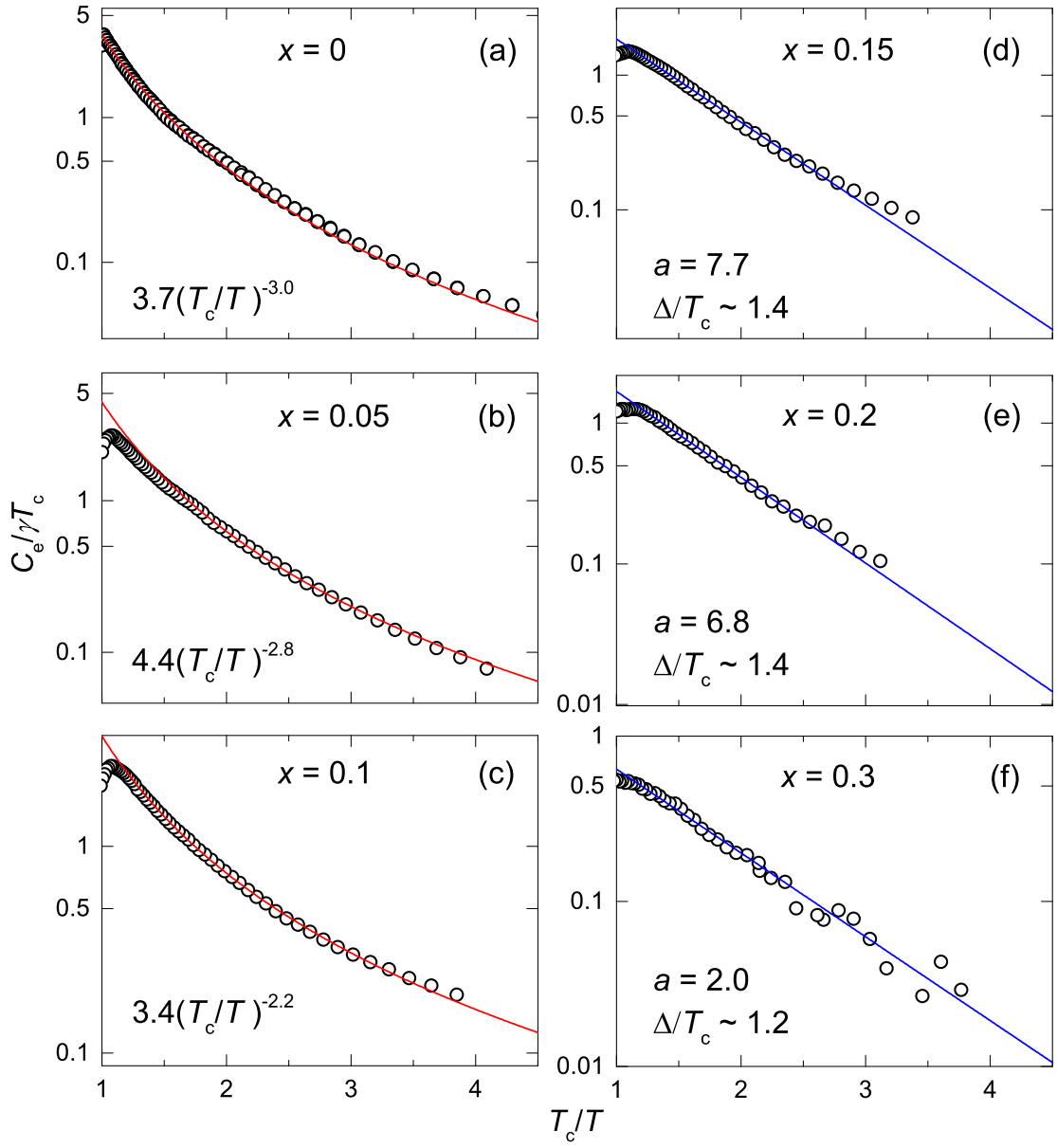


Figure V.7: Semilogarithmic plots of the electronic contribution to specific heat, $C_e(T)/\gamma T_c$, below $T_c$, versus $T_c/T$ for $Pr_{1-x}Eu_xPt_4Ge_{12}$ with $x = 0$, 0.5, 0.1, 0.15, 0.2, and 0.3. The red and blue lines represent the best fits to the data with (a, b, c) power-law behavior, $b(T_c/T)^{-m}$, and (d, e, f) exponential behavior, $ae^{-\Delta/T_c}$, respectively.

Similar crossovers or changes from power law to exponential temperature dependence in $C(T)$ the superconducting state were observed in the studies on the $Pr(Os_{1-x}Ru_x)_4Sb_{12}$, $Pr_{1-x}Ce_xPt_4Ge_{12}$, $La_{1-x}Ce_xPt_4Ge_{12}$, and $PrPt_4Ge_{12-x}Sb_x$ systems [12, 13, 34, 35]. A possible explanation for this change is a crossover in the superconducting energy gap from point-nodes to nodeless structures, or a suppression of one or more superconducting energy gaps in a multiband superconductor [5, 10, 11, 33]. Recently, low-temperature specific heat measurements on $Pr_{1-x}Ce_xPt_4Ge_{12}$ suggest the presence of both a nodal and a nodeless gap on different parts of the Fermi surface in $PrPt_4Ge_{12}$, which are suppressed with different rates upon increasing Ce substitutions [14]. This scenario would be another explanation for the non-integer values of $m$ in the $x = 0.05$ and 0.1 data and the low-temperature upturns or deviations from the linear fits for the $x = 0.15$ and 0.2 samples. However, the latter deviations could also be due to the fact that the values of $\Delta/T_c$ could vary depending on the fitting range [36]. More detailed studies of low-temperature specific heat on the $Pr_{1-x}Eu_xPt_4Ge_{12}$ system are underway. These studies will be able to discriminate between these different scenarios and will reveal the nature of the superconducting order parameters and their evolution with Eu concentration.

## V.D Discussion

Figure V.8 summarizes the results from $\rho(T)$, $\chi_{vol}(T)$, and $C(T)$ measurements in a temperature, $T$, versus europium, $x$, $(T - x)$, phase diagram. The SC transition temperature, $T_c$, values were taken from the onset of diamagnetic signals in the $\chi_{vol}(T)$ data. For the $C(T)$ measurements, $T_c$ was determined from the results of idealized entropy-conserving constructions [37, 38] (data not shown). The error bars were taken from the width of transitions in both resistivity and specific

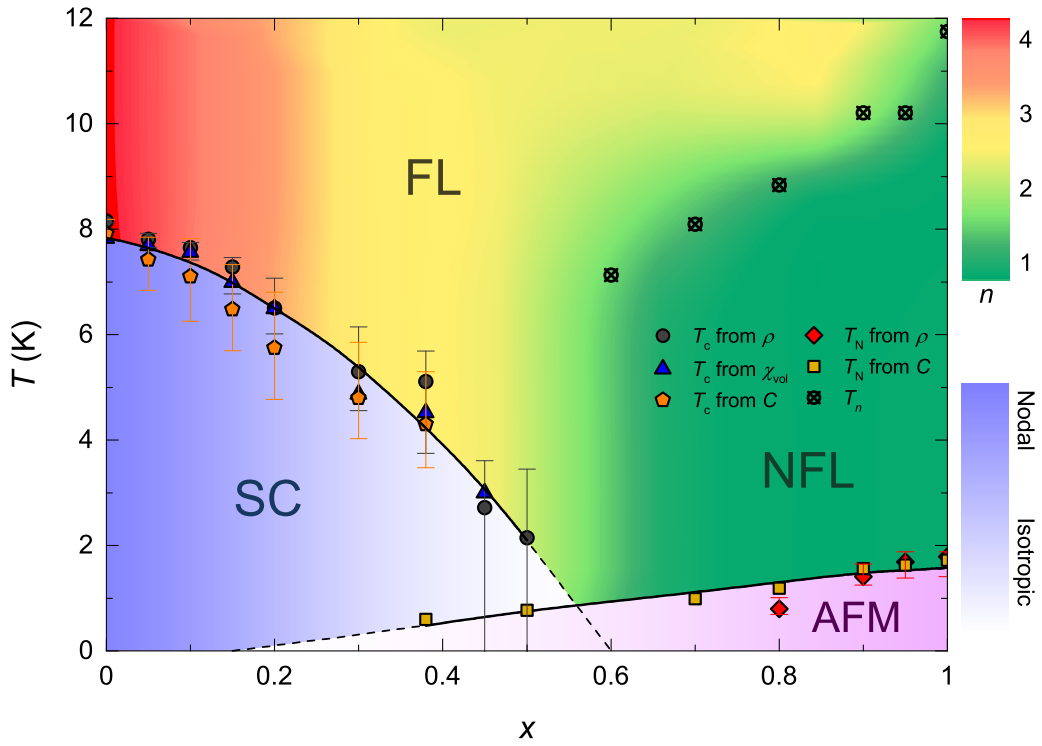


Figure V.8: A plot of temperature $T$ versus Eu concentration $x$, $(T - x)$, phase diagram. The vertical bars in the $T_c(x)$ data represent the widths of the superconducting transitions (see text). The suppression of $T_c$ with $x$ has negative curvature and extrapolates to 0 K near $x = 0.6$. The blue gradient-filled area under the $T_c$ versus $x$ curve represents the change of the temperature-dependence of low-temperature specific heat, $C_e/\gamma T_c = b(T_c/T)^{-m}$ to $ae^{-\Delta/T_c}$. The Néel temperature $T_N$ decreases slowly from $x = 1$ to $x \simeq 0.38$. SC and AFM may coexist in the region between $x \simeq 0.2$ and $\simeq 0.6$. The black circles with crosses are the temperatures, $T_n$, where resistivity slopes have kinks as seen in Fig. V.3(a). The color contour plot in the background displays the evolution of the power $n$ values in the formula, $\log(\rho(T) - \rho_0) = \log(A_n) + n\log(T)$.

heat data. These $T_c$ values estimated by different measurements exhibit a consistent trend, in which SC is suppressed with negative curvature up to $x \simeq 0.6$. The suppression rate of $T_c$ for $Pr_{1-x}Eu_xPt_4Ge_{12}$ is different compared to our previous substitution studies of $Pr_{1-x}Ce_xPt_4Ge_{12}$ and $PrPt_4Ge_{12-x}Sb_x$, which show suppressions of $T_c$ with positive curvature [12, 13]. Since Eu ions have a stable divalent electronic state in the skutterudite structure [24], the crystalline electric field effects are expected to be absent. Thus, we could consider the effect on SC of substituting $Eu^{+2}$ ions as similar to that of substituting $Gd^{3+}$ for Pr. The monotonic change of our $\mu_{\rm eff}$ data (see Fig. V.4(c)) supports this scenario. Rare earth impurities with stable valences are believed to exhibit ferromagnetic exchange interactions with a host superconductor (this case, $PrPt_4Ge_{12}$) wherein the depression of $T_c$ with paramagnetic impurity concentration is described by the Abrikosov-Gor'kov (AG) theory [39], as has been demonstrated for the $La_{1-x}Gd_xAl_2$ system [40]. The negative curvature of $T_c(x)$ in this study seems to be consistent with the AG theory, compared to the results of the Ce substitution study, in which the depression of $T_c$ with $x$ resembles the behavior expected for a system in which the paramagnetic impurities produce a Kondo effect in which the Kondo temperature is much larger than the SC transition temperature $T_c$. On the other hand, the substitution of $Eu^{2+}$ ions (hole doping), is different from that of $Gd^{3+}$ (isoelectronic substitution). A non-isovalent mixture of Pr/Eu would probably affect $T_c$ in $Pr_{1-x}Eu_xPt_4Ge_{12}$, since charge is transferred from the rare-earth guest ions to the host material. This would, in turn, change the Fermi level, which is one of crucial parameters that controls SC in the $MPt_4Ge_{12}$ compounds, as reported in a previous study on the $BaPt_{4-x}Au_xGe_{12}$ system [41]. However the doping into the Pr site may have a weaker effect on SC than doping into the Pt-Ge cage, since the Fermi surface of $PrPt_4Ge_{12}$ is mainly composed of the Ge-4$p$ orbitals with small contributions from the Pt-5$d$ orbitals [7]. In the SC states of the $Pr_{1-x}Eu_xPt_4Ge_{12}$

system, the situation is more complicated than in $La_{1-x}Gd_xAl_2$, as we observed evidence for a crossover in the SC energy gap from point-nodes to nodeless structures, or a suppression of one or more superconducting energy gaps in a multiband superconductor [5, 10, 11, 14, 33]. This crossover behavior is depicted by color gradient below the $T_c$ versus $x$ curve in Fig. V.8.

The Néel temperatures, $T_N$, were consistent between the $\rho(T)$ and the low-temperature $C(T)$ data. The $Pr_{1-x}Eu_xPt_4Ge_{12}$ system exhibits a crossover from SC to AFM states with increasing $x$ and, more interestingly, a coexistence of those two states in the range of $0.2 \simeq x \simeq 0.6$. Such a coexistence of AFM and SC has been observed in other conventional and unconventional SC containing localized magnetic moments [42–44]. As recently suggested by Singh *et al.* [14], our system seems to show that the nodal gap is being suppressed relatively slowly upon Eu substitution in the SC and coexistence regions, compared to the rapid suppressions observed in previous reports [12, 13]. In the non-ordered states, i.e., the high-temperature region, the system shows an evolution of the power dependence of the resistivity in the formula $\rho(T) = \rho_0 + AT^n$, shown as a color contour plot in Fig. V.8. The values of $n$ change from $n \sim 5$ at Pr rich sites to $n \sim 2$ (FL behavior) at $x \sim 0.5$, and then enters a NFL state with $n \sim 1$ at Eu rich sites. Such FL to NFL transition is also manifested by small kinks observed in the resistivity data (see Fig. V.3). In the specific heat data, we did not observe a very clear logarithmic divergence (data not shown), $C(T)/T \sim (-1/T_0)\ln(T/T_0)$, which is believed to be a nearly universal feature of NFL behavior in specific heat [45]; however, a weak power-law divergence could be also an indication for NFL behavior [45] and the divergence in specific heat could vary between different systems [46]. Therefore, we speculate that the rather large jumps in the specific heat for the Eu rich compounds are possibly the combination of AFM transitions and the divergence due to the NFL behavior. However, there are other possible scenarios for the observed

kinks in resistivity, for example, subtle structural phase transitions, which have been reported in skutterudite-related systems [47].

Our study of $Pr_{1-x}Eu_xPt_4Ge_{12}$ shows a complex phase diagram with SC to AFM and FL to NFL crossovers, suggesting that changes in the underlying electronic structure "tune" competing interactions in this system; this interpretation could be supported by the scenario of multiband type of SC with different energy gap structures in $PrPt_4Ge_{12}$ [9–11, 14]. Since there is no report of the $GdPt_4Ge_{12}$ compound, it would be interesting to perform a substitution study of $Pr_{1-x}Gd_xPt_4Ge_{12}$ as a comparative study with the current study. Subsequent studies of density functional theory (DFT) calculations on $Pr_{1-x}(Eu,Gd)_xPt_4Ge_{12}$ would give us better understanding of the relationship of the electronic density of states (DOS) and paramagnetic impurities on the nature of unconventional SC in $PrPt_4Ge_{12}$.

## V.E Concluding Remarks

We studied the superconducting and normal-state properties of the unconventional superconductor $PrPt_4Ge_{12}$, in which Eu has been substituted for Pr. Polycrystalline samples of $Pr_{1-x}Eu_xPt_4Ge_{12}$ were investigated via x-ray diffraction, electrical resistivity, magnetic susceptibility, and specific heat measurements. Upon Eu substitution, we observed a crossover from superconducting to antiferromagnetically ordered states with a region where superconductivity and antiferromagnetism may coexist. In the superconducting region, the specific heat data exhibit a crossover of temperature dependence, suggesting a change from a nodal to a nodeless superconducting energy gap or suppression of multiband superconductivity. This crossover is relatively slower than previous reports of different substitution studies, suggesting paramagnetic impurities have weaker pair break-

ing effect on the unconventional superconductivity in $PrPt_4Ge_{12}$. In the normal state, we observed a crossover from Fermi-liquid to non-Fermi-liquid behavior, accompanied by a coexistence of superconductivity and antiferromagnetism, suggesting intrinsic electronic structures may be correlated with the complex physical phenomena in this system.

The text and data presented in this chapter are reprints of material that appears in "Crossover and coexistence of superconductivity and antiferromagnetism in the filled-skutterudite system $Pr_{1-x}Eu_xPt_4Ge_{12}$," I. Jeon, S. Ran, A. J. Breindel, P.-C. Ho, R. B. Adhikari, C. C. Almasan, B. Luong, and M. B. Maple, *Phys. Rev. B* **95**, 134517 (2017). The dissertation author is the primary investigator and author of this article.

## Bibliography

[1] E. Bauer, A. Grytsiv, X.-Q. Chen, N. Melnychenko-Koblyuk, G. Hilscher, H. Kaldarar, H. Michor, E. Royanian, G. Giester, M. Rotter, R. Podloucky, and P. Rogl, Phys. Rev. Lett. **99**, 217001 (2007).

[2] E. Bauer, X.-Q. Chen, P. Rogl, G. Hilscher, H. Michor, E. Royanian, R. Podloucky, G. Giester, O. Sologub, and A. P. Gonçalves, Phys. Rev. B **78**, 064516 (2008).

[3] R. Gumeniuk, W. Schnelle, H. Rosner, M. Nicklas, A. Leithe-Jasper, and Y. Grin, Phys. Rev. Lett. **100**, 017002 (2008).

[4] M. Toda, H. Sugawara, K. ichi Magishi, T. Saito, K. Koyama, Y. Aoki, and H. Sato, J. Phys. Soc. Jpn. **77**, 124702 (2008).

[5] A. Maisuradze, M. Nicklas, R. Gumeniuk, C. Baines, W. Schnelle, H. Rosner, A. Leithe-Jasper, Y. Grin, and R. Khasanov, Phys. Rev. Lett. **103**, 147002 (2009).

[6] F. Kanetake, H. Mukuda, Y. Kitaoka, H. Sugawara, K. Magishi, K. M. Itoh, and E. E. Haller, Physica C **470**, S703 (2010).

[7] R. Gumeniuk, H. Borrmann, A. Ormeci, H. Rosner, W. Schnelle, M. Nicklas, Y. Grin, and A. Leithe-Jasper, Z. Kristallogr. **225**, 531 (2010).

[8] A. Maisuradze, W. Schnelle, R. Khasanov, R. Gumeniuk, M. Nicklas, H. Rosner, A. Leithe-Jasper, Y. Grin, A. Amato, and P. Thalmeier, Phys. Rev. B **82**, 024524 (2010).

[9] L. S. S. Chandra, M. K. Chattopadhyay, and S. B. Roy, Phil. Mag. **92**, 3866 (2012).

[10] Y. Nakamura, H. Okazaki, R. Yoshida, T. Wakita, H. Takeya, K. Hirata, M. Hirai, Y. Muraoka, and T. Yokoya, Phys. Rev. B **86**, 014521 (2012).

[11] J. L. Zhang, Y. Chen, L. Jiao, R. Gumeniuk, M. Nicklas, Y. H. Chen, L. Yang, B. H. Fu, W. Schnelle, H. Rosner, A. Leithe-Jasper, Y. Grin, F. Steglich, and H. Q. Yuan, Phys. Rev. B **87**, 064502 (2013).

[12] K. Huang, L. Shu, I. K. Lum, B. D. White, M. Janoschek, D. Yazici, J. J. Hamlin, D. A. Zocco, P.-C. Ho, R. E. Baumbach, and M. B. Maple, Phys. Rev. B **89**, 035145 (2014).

[13] I. Jeon, K. Huang, D. Yazici, N. Kanchanavatee, B. D. White, P.-C. Ho, S. Jang, N. Pouse, and M. B. Maple, Phys. Rev. B **93**, 104507 (2016).

[14] Y. P. Singh, R. B. Adhikari, S. Zhang, K. Huang, D. Yazici, I. Jeon, M. B. Maple, M. Dzero, and C. C. Almasan, Phys. Rev. B **94**, 144502 (2016).

[15] D. C. Johnston, Advances in Physics **59**, 803 (2010).

[16] G. R. Stewart, Rev. Mod. Phys. **83**, 1589 (2011).

[17] P.-C. Ho, T. Yanagisawa, W. M. Yuhasz, A. A. Dooraghi, C. C. Robinson, N. P. Butch, R. E. Baumbach, and M. B. Maple, Phys. Rev. B **83**, 024511 (2011).

[18] D. E. MacLaughlin, P.-C. Ho, L. Shu, O. O. Bernal, S. Zhao, A. A. Dooraghi, T. Yanagisawa, M. B. Maple, and R. H. Fukuda, Phys. Rev. B **89**, 144419 (2014).

[19] A. Grytsiv, X.-Q. Chen, N. Melnychenko-Koblyuk, P. Rogl, E. Bauer, G. Hilscher, H. Kaldarar, H. Michor, E. Royanian, R. Podloucky, M. Rotter, and G. Giester, J. Phys. Soc. Jap. **77**, 121 (2008).

[20] E. D. Bauer, A. Slebarski, N. A. Frederick, W. M. Yuhasz, M. B. Maple, D. Cao, F. Bridges, G. Giester, and P. Rogl, J. Phys.: Condens. Matter **16**, 5095 (2004).

[21] C. Sekine, K. Akahira, K. Ito, and T. Yagi, J. Phys. Soc. Jpn. **78**, 093707 (2009).

[22] V. V. Krishnamurthy, J. C. Lang, D. Haskel, D. J. Keavney, G. Srajer, J. L. Robertson, B. C. Sales, D. G. Mandrus, D. J. Singh, and D. I. Bilc, Phys. Rev. Lett. **98**, 126403 (2007).

[23] C. Sekine, M. Inoue, T. Inaba, and I. Shirotani, Physica B: Condensed Matter **281/282**, 308 (2000).

[24] M. Nicklas, R. Gumeniuk, W. Schnelle, H. Rosner, A. Leithe-Jasper, F. Steglich, and Y. Grin, J. Phys.: Conf. Ser. **273**, 012118 (2011).

[25] A. C. Larson and R. B. V. Dreele, Los Alamos National Laboratory Report, 1994 (unpublished).

[26] B. Toby, J. Appl. Crystallogr. **34**, 210 (2001).

[27] B. D. White, K. Huang, and M. B. Maple, Phys. Rev. B **90**, 235104 (2014).

[28] R. M. Galéra, C. Opagiste, M. Amara, M. Zbiri, and S. Rols, J. Phys.: Conf. Ser. **592**, 012011 (2015).

[29] N. F. Mott and H. Jones, *The theory of the properties of metals and alloys* (Dover Publications Inc., New York, 1958).

[30] M. Nicklas, S. Kirchner, R. Borth, R. Gumeniuk, W. Schnelle, H. Rosner, H. Borrmann, A. Leithe-Jasper, Y. Grin, and F. Steglich, Phys. Rev. Lett. **109**, 236405 (2012).

[31] E. D. Bauer, N. A. Frederick, P.-C. Ho, V. S. Zapf, and M. B. Maple, Phys. Rev. B **65**, 100506 (2002).

[32] M. B. Maple, P.-C. Ho, V. S. Zapf, N. A. Frederick, E. D. Bauer, W. M. Yuhasz, F. M. Woodward, and J. W. Lynn, J. Phys. Soc. Jpn. **71**, 23 (2002).

[33] M. Sigrist and K. Ueda, Rev. Mod. Phys. **63**, 239 (1991).

[34] N. A. Frederick, T. A. Sayles, S. K. Kim, and M. B. Maple, J. Low Temp. Phys. **147**, 321 (2007).

[35] K. Huang, D. Yazici, B. D. White, I. Jeon, A. J. Breindel, N. Pouse, and M. B. Maple, Phys. Rev. B **94**, 094501 (2016).

[36] G. Gladstone, M. A. Jensen, and J. R. Schrieffer, in *Superconductivity*, edited by R. D. Parks (Marcel Dekker, New York, 1969), vol. 2, p. 699.

[37] E. Bonjour, R. Calemczuk, J. Y. Henry, and A. F. Khoder, Phys. Rev. B **43**, 106 (1991).

[38] S. B. Ota, V. S. Sastry, E. Gmelin, P. Murugaraj, and J. Maier, Phys. Rev. B **43**, 6147 (1991).

[39] A. A. Arikosov and L. P. Gor'kov, Sov. Phys.-JETP **12**, 1243 (1961).

[40] M. B. Maple, E. D. Bauer, V. S. Zapf, and J. Wosnitza, in *Superconductivity, Conventional and Unconventional Superconductors*, edited by K. H. Bennemann and J. B. Ketterson (Springer, Berlin, 2008), vol. 1, p. 693.

[41] R. Gumeniuk, H. Rosner, W. Schnelle, M. Nicklas, A. Leithe-Jasper, and Y. Grin, Phys. Rev. B **78**, 052504 (2008).

[42] R. McCallum, D. Johnston, R. Shelton, and M. Maple, Solid State Commun. **24**, 391 (1977).

[43] M. Ishikawa and . A. Fischer, Solid State Commun. **24**, 747 (1977).

[44] X. F. Lu, N. Z. Wang, H. Wu, Y. P. Wu, D. Zhao, X. Z. Zeng, X. G. Luo, T. Wu, W. Bao, G. H. Zhang, F. Q. Huang, Q. Z. Huang, and X. H. Chen, Nat. Mater. **14**, 325 (2015).

[45] M. B. Maple, R. E. Baumbach, N. P. Butch, J. J. Hamlin, and M. Janoschek, J. Low Temp. Phys. **161** (2010).

[46] L. Zhu, M. Garst, A. Rosch, and Q. Si, Phys. Rev. Lett. **91**, 066404 (2003).

[47] A. Ślebarski, M. Fijałkowski, M. M. Maśka, M. Mierzejewski, B. D. White, and M. B. Maple, Phys. Rev. B **89**, 125111 (2014).